



UNIL | Université de Lausanne

Unicentre

CH-1015 Lausanne

<http://serval.unil.ch>

Year : Tourbier Sébastien

NOVEL IMAGE PROCESSING METHODS FOR IMPROVED FETAL BRAIN MRI

2016

2016, Tourbier Sébastien, NOVEL IMAGE PROCESSING METHODS FOR IMPROVED FETAL
BRAIN MRI

Originally published at : Thesis, University of Lausanne

Posted at the University of Lausanne Open Archive <http://serval.unil.ch>

Document URN : urn:nbn:ch:serval-BIB_92AC4B1CA9EE5

Droits d'auteur

L'Université de Lausanne attire expressément l'attention des utilisateurs sur le fait que tous les documents publiés dans l'Archive SERVAL sont protégés par le droit d'auteur, conformément à la loi fédérale sur le droit d'auteur et les droits voisins (LDA). A ce titre, il est indispensable d'obtenir le consentement préalable de l'auteur et/ou de l'éditeur avant toute utilisation d'une oeuvre ou d'une partie d'une oeuvre ne relevant pas d'une utilisation à des fins personnelles au sens de la LDA (art. 19, al. 1 lettre a). A défaut, tout contrevenant s'expose aux sanctions prévues par cette loi. Nous déclinons toute responsabilité en la matière.

Copyright

The University of Lausanne expressly draws the attention of users to the fact that all documents published in the SERVAL Archive are protected by copyright in accordance with federal law on copyright and similar rights (LDA). Accordingly it is indispensable to obtain prior consent from the author and/or publisher before any use of a work or part of a work for purposes other than personal use within the meaning of LDA (art. 19, para. 1 letter a). Failure to do so will expose offenders to the sanctions laid down by this law. We accept no liability in this respect.



UNIL | Université de Lausanne

Faculté de biologie
et de médecine

Centre d'Imagerie BioMédicale,
Département de radiodiagnostic et radiologie interventionnelle, CHUV

**NOVEL IMAGE PROCESSING METHODS
FOR IMPROVED FETAL BRAIN MRI**

Thèse de doctorat en sciences de la vie (PhD)

présentée à la

Faculté de biologie et de médecine
de l'Université de Lausanne

par

Sébastien TOURBIER

Ingénieur en systèmes de communication diplômé
de l'Ecole Polytechnique Fédérale de Lausanne

Jury:

Prof. Viktor Bartanusz, président
Prof. Reto Meuli, directeur de thèse
Dr. Meritxell Bach Cuadra, co-directrice de thèse
Prof. Simon K. Warfield, expert
Prof. Pierre Vanderghyest, expert

Lausanne, 2016

Imprimatur

Vu le rapport présenté par le jury d'examen, composé de

Président · e	Monsieur Prof. Viktor Bartanusz
Directeur · rice de thèse	Monsieur Prof. Reto Meuli
Co-directeur · rice	Madame Dre Meritxell Bach cuadra
Experts · es	Monsieur Prof. Simon Warfield
	Monsieur Prof. Pierre Vandergheynst

le Conseil de Faculté autorise l'impression de la thèse de

Monsieur Sébastien Tourbier

Master in communication systems EPFL

intitulée

**NOVEL IMAGE PROCESSING METHODS
FOR IMPROVED FETAL BRAIN MRI**

Lausanne, le 30 septembre 2016

pour le Doyen
de la Faculté de biologie et de médecine

Prof. Viktor Bartanusz

To my family, friends and colleagues...

Abstract

Fetal magnetic resonance imaging (MRI) has been increasingly used as a powerful complement imaging modality to ultrasound imaging (US) for the clinical evaluation of prenatal abnormalities. Specifically, clinical application of fetal MRI has been significantly improved in the nineties by hardware and software advances with the development of ultrafast multi-slice T2-weighted (T2w) acquisition sequences able to freeze the unpredictable fetal motion and provide excellent soft-tissue contrast. Fetal motion is indeed the major challenge in fetal MRI and slice acquisition time should be kept as short as possible. As a result, typical fetal MRI examination involves the acquisition of a set of orthogonally planned scans of thick two-dimensional slices, largely free of intra-slice motion artifacts. The poor resolution in the slice-select dimension as well as possible motion occurring between slices limits further quantitative data analysis, which is the key for a better understanding of the developing brain but also the key for the determination of operator-independent biomarkers that might significantly facilitate fetal diagnosis and prognosis.

To this end, several research groups have developed in the past ten years advanced image processing methods, often denoted by motion-robust super-resolution (SR) techniques, to reconstruct from a set of clinical low-resolution (LR) scans, a high-resolution (HR) motion-free volume. SR problem is usually modeled as a linear inverse problem describing the imaging degradation due to acquisition and fetal motion. Typically, such approaches consist in iterating between slice motion estimation that estimates the motion parameters and SR that recovers the HR image given the estimated degradation model. This thesis focuses on the development of novel advanced image processing methods, which have enabled the design of a completely automated reconstruction pipeline for fetal MRI. The proposed techniques help in improving state-of-the-art fetal MRI reconstruction in terms of efficiency, robustness and minimized user-interactions, with the ultimate goal of being translated to the clinical environment.

The first part focuses on the development of a more efficient Total Variation (TV)-regularized optimization algorithm for the SR problem. The algorithm uses recent advances in convex

optimization with a novel adaptive regularization strategy to offer simultaneously fast, accurate and robust solutions to the fetal image recovery problem. Extensive validations on both simulated fetal and real clinical data show the proposed algorithm is highly robust in front of motion artifacts and that it offers the best trade-off between speed and accuracy for fetal MRI recovery as in comparison with state-of-the art methods.

The second part focuses on the development of a novel automatic brain localization and extraction approach based on template-to-slice block matching and deformable slice-to-template registration. As most fetal brain MRI reconstruction algorithms rely only on brain tissue-relevant voxels of low-resolution (LR) images to enhance the quality of inter-slice motion correction and image reconstruction, the fetal brain needs to be localized and extracted as a first step. These tasks generally necessitate user interaction, manually or semi-automatically done. Our methods have enabled the design of completely automated reconstruction pipeline that involves intensity normalization, inter-slice motion estimation, and super-resolution. Quantitative evaluation on clinical MRI scans shows that our approach produces brain masks that are very close to manually drawn brain masks, and ratings performed by two expert observers show that the proposed pipeline achieves similar reconstruction quality to reference reconstruction based on manual slice-by-slice brain extraction without any further effort.

The third part investigates the possibility of automatic cortical folding quantification, one of the best biomarkers of brain maturation, by combining our automatic reconstruction pipeline with a state-of-the-art fetal brain tissue segmentation method and existing automated tools provided for adult brain's cortical folding quantification. Results indicate that our reconstruction pipeline can provide HR MR images with sufficient quality that enable the use of surface tessellation and active surface algorithms similar to those developed for adults to extract meaningful information about fetal brain maturation.

Finally, the last part presents new methodological improvements of the reconstruction pipeline aiming at improving the quality of the image for quantitative data analysis, whose accuracy is highly dependent on the quality and resolution of the reconstructed image. In particular, it presents a more consistent and global magnetic bias field correction method which takes advantage of the super-resolution framework to provide a final reconstructed image quasi free of the smooth bias field. Then, it presents a new TV SR algorithm that uses the Huber norm in the data fidelity term to be more robust to non-Gaussian outliers. It also presents the design of a novel joint reconstruction-segmentation framework and the development of a novel TV SR algorithm driven by segmentation to produce images with enhanced edge information that could ultimately improve their segmentation. Finally, it preliminary investigates the capability of increasing the resolution in the in-plane dimensions using SR to ultimately reduce the partial volume effect.

Keywords: Brain, Fetal, MRI, Slice-to-Volume Reconstruction, Super-Resolution, Total Variation Regularization, Convex Optimization, Atlas-based Segmentation, Slice-by-Slice De-

formable Registration, Brain Localization, Brain Extraction, Bias Field Correction.

Résumé

L'imagerie par résonance magnétique (IRM) cérébrale fœtale est une modalité devenue de plus en plus utilisée comme un puissant complément à l'imagerie par ultrasons (US) pour l'évaluation des anomalies prénatales en milieu clinique. Plus précisément, l'application clinique de l'IRM fœtale a été considérablement améliorée dans les années nonante grâce au développement de nouvelles séquences d'acquisition multi-coupes en pondération T2 (T2w), capables de figer le mouvement du fœtus et de fournir un excellent contraste des tissus mous constituant le cerveau.

Le mouvement fœtal est au fond le défi majeur de l'IRM fœtale et le temps d'acquisition d'une coupe doit être aussi court que possible. En conséquence, les examens actuels d'IRM fœtales consistent en l'acquisition d'un ensemble de coupes en deux dimensions épaisses, en grande partie libres d'artefacts inhérents au mouvement intervenant durant l'acquisition d'une coupe. Cependant, la mauvaise résolution obtenue dans la direction d'acquisition ainsi que le mouvement pouvant survenir entre l'acquisition des coupes limitent une analyse quantitative des images, qui est la clé d'une meilleure compréhension du développement du cerveau, mais aussi la clé de la détermination de biomarqueurs indépendants de l'opérateur qui pourrait faciliter considérablement le diagnostic prénatal et le pronostic.

Durant ces dernières années, plusieurs groupes de recherche ont mis au point à cette fin des méthodes avancées de traitement d'images, souvent désignées par techniques de super-résolution (SR). Ces méthodes sont capables de reconstruire une image à haute résolution (HR) libre de tout mouvement, à partir d'un ensemble de scans cliniques à basse résolution. Dans ces travaux, le problème de super-résolution est généralement modélisé comme un problème inverse linéaire, décrivant la dégradation de l'image qui est induite par l'acquisition et le mouvement fœtal. Cette thèse porte sur le développement de nouvelles méthodes de traitement d'images qui ont permis la conception d'un pipeline de reconstruction entièrement automatisé pour l'IRM fœtale. Les techniques proposées aident à améliorer la reconstruction de pointe de l'IRM fœtale en termes d'efficacité, de robustesse, et en réduisant les interactions

de l'utilisateur, dans le but ultime d'être employées dans un environnement clinique.

La première partie porte sur le développement d'un algorithme plus efficace pour le problème de SR, régularisé avec la variation totale de l'image (TV). L'algorithme proposé utilise les récentes avancées en optimisation convexe avec une nouvelle stratégie de régularisation adaptative pour offrir des solutions à la fois rapides, précises et robustes au problème de récupération de l'image HR du cerveau. Une validation approfondie montre que notre algorithme est, en comparaison avec les méthodes de pointe, plus robuste aux artefacts causés par le mouvement fœtal et qu'il offre le meilleur compromis entre vitesse et précision pour la restauration de l'IRM fœtal à haute-résolution.

La deuxième partie porte sur le développement d'une nouvelle technique automatique de localisation et d'extraction du cerveau, basée sur l'utilisation d'un atlas spatio-temporel et l'appariement d'un algorithme de correspondance de blocs avec un algorithme de recallage déformable d'images. Comme la plupart des algorithmes de reconstruction IRM du cerveau fœtal reposent uniquement sur les voxels de tissus pertinents au cerveau pour améliorer la qualité de la correction de mouvement inter-coupe et la reconstruction de l'image, le cerveau du fœtus doit être localisé et extrait dans un premier temps. Ces tâches nécessitent généralement l'interaction de l'utilisateur, étant effectuées manuellement ou semi-automatiquement. Nos méthodes ont permis la conception d'un pipeline de reconstruction entièrement automatisé qui inclut des processus de normalisation d'intensité, d'estimation du mouvement, et de super-résolution. Une évaluation quantitative montre que l'approche proposée produit des masques du cerveau très proches de ceux dessinés manuellement, et une évaluation visuelle, réalisée par deux experts, montre que le pipeline proposé permet d'obtenir une qualité de reconstruction similaire à une reconstruction de référence utilisant des masques manuellement dessinés, sans effort supplémentaire.

La troisième partie étudie la possibilité de quantification automatique du plissement cortical, qui est l'un des meilleurs indicateurs de la maturation du cerveau, en combinant notre pipeline de reconstruction automatique avec une méthode de segmentation de pointe et des outils automatisés, développés pour la quantification du plissement cortical chez adulte. Les résultats indiquent que notre pipeline de reconstruction peut fournir des IRM à haute résolution, dont la qualité est suffisante pour extraire des informations utiles sur la maturation du cerveau fœtal, tout en utilisant des algorithmes de tessellation de surfaces et de surfaces actives similaires à ceux développés pour les cerveaux adultes.

Finalement, la dernière partie présente de très récentes améliorations méthodologiques du pipeline de reconstruction, visant à améliorer la qualité de l'image pour l'analyse quantitative ultérieure, dont la précision est très dépendante de la qualité et résolution de l'image reconstruite. En particulier, elle présente une méthode plus consistante de correction du champ de biais d'intensité, qui profite du cadre de super-résolution pour fournir une image reconstruite finale quasiment libre du champ de biais. Cette partie présente ensuite un nouvel algorithme

TV SR qui utilise la norme de Huber dans son terme de fidélité aux données pour être plus robuste aux valeurs aberrantes non-Gaussiennes. Elle présente également la conception d'un cadre novateur de reconstruction-segmentation conjointe, et le développement d'un algorithme TV SR conduit par la segmentation, pour produire des images avec des interfaces aux tissus plus accentuées qui pourrait ultimement améliorer leur segmentation. Finalement, elle donne une enquête préliminaire sur la capacité d'augmenter la résolution dans le plan d'acquisition à l'aide de SR pour réduire l'effet de volume partiel.

Mots-clefs : Cerveau, Fetal, IRM, Reconstruction Coupe-à-Volume, Super-Resolution, Régularisation basée sur la Variation Totale (TV), Optimisation Convexe, Segmentation basée sur Atlas, Recallage Déformable Coupe-par-Coupe, Localisation du Cerveau, Extraction du Cerveau, Correction du Champ de Biais d'Intensité.

Contents

Abstract (English/Français)	i
List of figures	xiii
List of tables	xv
Introduction	1
Fetal magnetic resonance imaging: clinical context	1
Single-shot T2-weighted imaging	2
Towards a motion-free high-resolution image	5
Segmentation and quantification of fetal brain	9
Thesis outline and contributions	11
Bibliography	13
1 An Efficient TV Algorithm for Super-Resolution in Fetal Brain MRI with Adaptive Regularization	19
1.1 Introduction	19
1.2 Contributions	21
1.3 Overview of fetal MRI reconstruction algorithms	22
1.3.1 Notations and definitions	22
1.3.2 A generic observation model	22
1.3.3 Two-step reconstruction algorithm	24
1.3.4 Motion estimation algorithms	25
1.3.5 Fetal MRI restoration algorithms	26
1.4 Our Total Variation algorithm	30
1.4.1 Algorithm description	30
1.4.2 Adaptive regularization parameter λ	32
1.4.3 Practical implementation	33
1.5 Results and validation	35

Contents

1.5.1	Material	35
1.5.2	Numerical comparison of optimization schemes: ε -TV v.s. exact TV . . .	36
1.5.3	Quantitative analysis of simulated fetal images	38
1.5.4	Quantitative analysis of real fetal images	39
1.5.5	Perceptual evaluation of the adaptive regularization	41
1.5.6	Discussion	43
1.6	Conclusion	45
	Bibliography	47
2	Automated Template-based Brain Localization and Extraction for Fetal Brain MRI Reconstruction	53
2.1	Introduction	53
2.2	Contributions	54
2.3	Overview of fetal brain localization and extraction	55
2.4	Novel template-based brain localization and extraction for fetal MRI	56
2.4.1	Template-to-slice block matching brain localization	57
2.4.2	Deformable slice-to-template brain extraction	60
2.4.3	Intensity standardization	61
2.4.4	Joint brain mask refinement and reconstruction	61
2.5	Results	63
2.5.1	Material	63
2.5.2	Performance of brain extraction	65
2.5.3	Influence of brain extraction on reconstruction quality	66
2.5.4	Perceptual evaluation of final reconstruction by expert observers	69
2.5.5	Application to intra-cranial fetal brain volumetry	70
2.6	Discussion	71
2.7	Conclusion	72
	Bibliography	75
3	Quantification of Fetal Cortical Folding using Super-Resolution MRI Reconstruction and FreeSurfer	79
3.1	Introduction	79
3.2	Contributions	81
3.3	Methods	81
3.4	Results	83
3.5	Discussion	83
3.6	Conclusion	85
	Bibliography	87
4	Further Improvements	89
4.1	Introduction	89
4.2	Contributions	90

4.3	Slice-by-slice intensity inhomogeneity correction from a globally-estimated bias field	91
4.3.1	Motivation	91
4.3.2	Method	92
4.3.3	Results	93
4.4	A robust Total Variation algorithm based on the Huber norm	94
4.4.1	Motivation	94
4.4.2	Method	95
4.4.3	Results	96
4.5	A segmentation-driven Total Variation super-resolution algorithm	97
4.5.1	Motivation	97
4.5.2	Methods	99
4.5.3	Results	101
4.6	Super-resolution to increasing in-plane fetal MRI resolution	104
4.6.1	Motivation	104
4.6.2	Method	105
4.6.3	Results	106
4.7	Conclusion	108
	Bibliography	111
5	Conclusion and perspectives	113
	Bibliography	117
A	MIALSRTK: C++ Medical Image Analysis Laboratory Super-Resolution Toolkit	119
A.1	Image denoising	119
A.2	Brain localization and extraction	120
A.3	Intensity standardization	121
A.4	Motion estimation	122
A.5	Super-resolution	122
A.6	Evaluation tools	122
A.7	Other tools	123
	Bibliography	125
	Curriculum Vitae	127

List of Figures

1	Single-shot T2-weighted magnetic resonance imaging principles.	4
2	Clinical orthogonally-planned fetal MRI scans.	5
3	Principle of super-resolution from anisotropic low-resolution images.	6
4	General paradigm for direct and iterative fetal brain MR image reconstruction.	7
1.1	MRI scans and HR reconstruction of a fetal brain of 25 weeks gestational age.	20
1.2	General paradigm for direct and iterative fetal brain MR image reconstruction.	21
1.3	The observation model of a real MR imaging system relating the low-resolution (LR) image \mathbf{X}_k^{LR} (observed images) to an high-resolution (HR) image \mathbf{X}	24
1.4	Summary of the overall fetal brain HR reconstruction pipeline.	34
1.5	Numerical comparison of optimization schemes: ϵ -TV vs exact TV.	38
1.6	Impact of the choice of ϵ in ϵ -TV algorithms.	38
1.7	Robustness of SR algorithms to motion error residuals when 1/5, 2/5, and 3/5 of the slices are affected.	39
1.8	Optimization of the regularization parameter λ	40
1.9	Illustration of the leave-one-out analysis results.	41
1.10	Illustration of the qualitative analysis for fetus P1, P8 and P10.	43
1.11	Regularization versus number of input LR images.	44
2.1	Automated pipeline for fetal MRI reconstruction.	57
2.2	Template-based brain localization and extraction from clinical MR scans.	59
2.3	Pipeline for refining LR brain masks.	62
2.4	Brain mask evolution.	66
2.5	Influence of brain extraction on image reconstruction quality in terms of Peak-Signal-to-Noise Ratios (PSNR) as reconstruction progresses.	67
2.6	Comparison of reconstruction results of case F10 using (i) only brain localization, (ii) rigid-only <i>slice-to-template</i> registration and (ii) the full method.	68

List of Figures

2.7	Brain extraction and reconstruction results of one pathological brain diagnosed with unilateral ventriculomegaly and one healthy brain.	70
2.8	Bland-Altman plot of intra-cranial fetal brain volumetry results.	71
3.1	Image processing pipeline for in-vivo fetal cortical folding quantification taking advantage of the set of tools provided by FreeSurfer.	82
3.2	Generic bash script that uses FreeSurfer to extract cortical surfaces and quantify cortical folding.	84
3.3	Reconstructed cortical surfaces from fetal MRI and resulting quantitative maps of cortical folding in normal brains.	85
4.1	Reconstruction pipeline for fetal MRI using the proposed bias field correction method	92
4.2	Reconstruction results using the improved bias field correction method.	94
4.3	Plots of the Huber error norm function and its associated weight function.	95
4.4	Comparison of Total Variation Super-Resolution algorithms based on the ℓ_2 -norm and the robust Huber norm.	98
4.5	Image processing pipeline for joint reconstruction-segmentation.	99
4.6	Reconstruction and segmentation results in a joint reconstruction-segmentation framework.	102
4.7	Impact of segmentation-driven reconstruction on further automatic volumetric analysis.	103
4.8	Comparison between mapping used currently and the new mapping for increased resolution in the in-plane dimensions.	105
4.9	Mapping between anisotropic voxels of the scans and voxels of the reconstructed image.	106
4.10	Impact of segmentation-driven reconstruction on further volumetric analysis using image reconstructed with increased isotropic resolution.	107
4.11	Impact of segmentation-driven reconstruction on reconstructed image contrast using image reconstructed with increased isotropic resolution.	108
4.12	Reconstruction and segmentation results in a joint reconstruction-segmentation framework using image reconstructed with increased isotropic resolution.	109
A.1	Our ultimate reconstruction pipeline for fetal MRI using MIALSRTK.	120

List of Tables

1.1	Clinical datasets.	37
1.2	Leave-one-out analysis: similarity w.r.t the original LR images.	40
1.3	Leave-one-out analysis: sharpness of the reconstructed HR images.	42
2.1	Clinical datasets.	64
2.2	Evolution of brain extraction performance as reconstruction progresses.	65
2.3	Qualitative rating of final reconstruction by two expert observers.	69

Introduction

Fetal magnetic resonance imaging: clinical context

Advances in hardware and software during the nineties have allowed magnetic resonance imaging (MRI) as a powerful complementary imaging modality for the evaluation of in utero fetal abnormalities in clinical settings. Since its first use in pregnancy, reported in 1983 [1], fetal MRI is now available in many prenatal diagnostic centers. Despite the cost and complexity, MRI has advantages over ultrasound. It provides a large field-of-view, facilitating examination of fetuses with complex anomalies, superior soft-tissue contrast resolution, and the ability to distinguish well individual structures such as gray and white matter in the fetal brain. It is still a noninvasive and non-ionizing technique where no evidence of adverse outcomes regarding fetal exposure to electromagnetic and sound energy has been reported in the literature [2]. As a precaution, fetal MRI is however only performed during the second and third trimesters of pregnancy and is sought and performed only after an optimal ultrasound examination. MRI is mainly indicated in pregnancy when (1) there is a history of brain abnormality in a previous pregnancy and MRI can detect more subtle signs of recurrence than ultrasound; (2) an abnormality is overlooked (such as corpus callosum agnesis) or identified by ultrasound (such as lissencephaly or ventriculomegaly) and MR-specific information is sought in order to make a diagnostic or to boost diagnostic confidence; (3) a fetus is significantly at risk for abnormality, especially in the case of infection; and (4) ultrasound cannot be completed due to technical problems such as maternal adiposity and fetal position. The field has now reached a maturity with a number of clinical findings reviewed in a number of excellent articles and the creation of atlas books [3, 4] that gives to physicians a better understanding and interpretation of the three dimensional fetal brain anatomy. Fetal MRI has shown to be particularly helpful in the detection of central nervous system abnormalities, including ventriculomegaly, abnormalities of the corpus callosum, abnormalities of posterior fossa, and severe intracranial hemorrhage [5, 6]. However, fetal MRI acquisition is very challenging due

Single-shot T2-weighted imaging

to unpredictable motion and current state-of-the-art fast multi-slice acquisition results in very anisotropic and potentially motion-corrupted images (stack of thick slices) in order to be able to freeze motion while having a sufficient signal level (Figure 1.1). The poor resolution of the image in the through-plane dimension creates a significant partial volume effect as well as the possible presence of motion artifacts complicate the diagnostic task of radiologists and limit the use of computer-assisted methods for large-scale studies. There is therefore a great interest in reconstructing a motion-free high-resolution image of the fetal brain.

In the rest of the introduction, I will familiarize the reader to the current *state-of-the-art* acquisition solution for fetal MRI, its limitations and the emergence of advanced retrospective image processing methods that have enabled the reconstruction of motion-free high-resolution images [7–16] and stimulated new research in the creation of spatio-temporal digital atlas of the developing brain [17, 18] and in the analysis of in utero fetal brain development and maturation [19–24].

Single-shot T2-weighted imaging

Fetal MRI is very challenging due to intermittent maternal and fetal motions that disrupt the spatial encoding needed for 3D image acquisition. The development of single-shot sequences in the nineties has made possible some sort of “snapshot” MR imaging that avoids image degradation from fetal motion [25, 26]. One of the very first single-shot imaging methods based upon multiple gradient echo trains, known as echo planar imaging (EPI) was first applied to study the fetus [27]. An other family of single-shot imaging methods based on RF spin echoes has been made available by the mid-nineties, known as Single-Shot T2-Weighted (SST2W) imaging. The last approach has quickly shown its supremacy for the evaluation of fetal brain in utero by providing the best contrast while being able to largely freeze motion [25, 28]. SST2W imaging has since then been the imaging modality of choice in the field.

I will now introduce the basic MRI principles to understand how a SST2W sequence works, how sequence parameters are fixed in practice. This will help the reader understanding current acquisition and spatial resolution limitations and the needs of developing advanced retrospective image processing techniques to enable the reconstruction of high-resolution images of the fetal brain.

MRI principles MR imaging relies on the energetic interaction between spins and electromagnetic radiofrequency (RF) [29]. Only protons that spin with the same frequency as the electromagnetic RF pulse (known as the Larmor or precession frequency) will respond to that RF pulse by absorbing electromagnetic energy and modifying its spin equilibrium. During this period of time, known as excitation, longitudinal magnetization decreases and a transverse magnetization appears, created by spins getting into phase coherence. When the system returns from this state of imbalance to equilibrium, there is an emission of electromagnetic energy that creates the MR signal. The transverse magnetization decay is described by an

exponential curve and is characterized by the time constant T2 after which it has lost 63% of its original value. MRI signal acquisition consists in sampling k-space, often referred as “filling” k-space, a matrix of pixel values representing spatial frequencies in the MR image. A 2D/3D MR image is thus a complex-valued map of the spatial distribution of the transverse magnetization in the sample at a specific time point after an excitation. The image is formed by applying a 2D/3D Fourier transform to its acquired 2D/3D k-space representation (Figure 1).

SST2W principles Fetal SST2W imaging consists of acquiring one k-space representation for each slice which is usually a 256×256 matrix, resulting in a stack of k-space (Figure 1); each of the line (frequency encoding direction in Figure 1) is occupied by one echo and each of the 256 values per line is occupied by an individual sample of transverse magnetization (phase encoding direction in Figure 1), measured after one slice selective excitation 90° RF pulse [28, 30]. This 90° RF pulse tips the equilibrium longitudinal magnetization from a slice of spins into the plane perpendicular to the main magnetic field, known as the “transverse plane”. It is followed by a series of slice selective refocusing 180° (theoretically), each of which leads to the generation of a “spin-echo” that undergoes T2 decay, the decay of transverse magnetization due to spins getting out of phase. Then, each spin-echo is acquired using RF coils during the frequency encoding which is preceded and followed by appropriate “wind” and “rewind” phase encode gradients such that it forms a line in k-space. Individual spin-echo duration (TE) is on the order of 2 to 3ms. After acquisition of all echoes, which happens after TE * number of frequency encodings to acquire ($256 \times [2 - 3]ms \approx [500 - 800]ms$), k-space is completely filled and the anatomic image is generated using 2D inverse Fourier transform. The sequence is further accelerated by half k-space acquisition using k-space symmetry to estimate the missing lines. It avoids the need to capture the latest echoes (whose signal is much reduced by T2 relaxation) and it allows acquisition time to be reduced by a factor close to 2. The degree of T2 contrast weighting is governed such that the specific echo times used for the low order phase encode lines determine the effective echo time (ETE) associated with the T2 contrast [28].

Implementation Common supplied SST2W sequences can be found under different names depending on the manufacturer: Single-Shot Fast Spin Echo (SSFSE) for General Electric Medical systems; Half-fourier Single-shot Turbo spin Echo (HASTE) for Siemens; Single-Shot half-Fourier Turbo Spin Echo (SShTSE) for Philips; Rapid Acquisition with Relaxation Enhancement (RARE) for Bruker Instruments. They use RF refocusing flip angles in the 120° to 150° range; wider the angle, stronger the signal. A well-designed fetal MR imaging protocol should consider the following “golden-rule”: each scan should take 25s or less in order to capture quiescent periods of fetal motion during one maternal breathholding cycle [28]. This 25s “golden rule” will thus constraint the parameters associated with the SST2W sequence (in-plane resolution and slice thickness) and the volume coverage, or number of slices, acquired per scan. As a result, current implementations of SST2W sequences are able to generate, in approximately 500 ms or less, a T2-weighted image with in-plane spatial resolutions from

Single-shot T2-weighted imaging

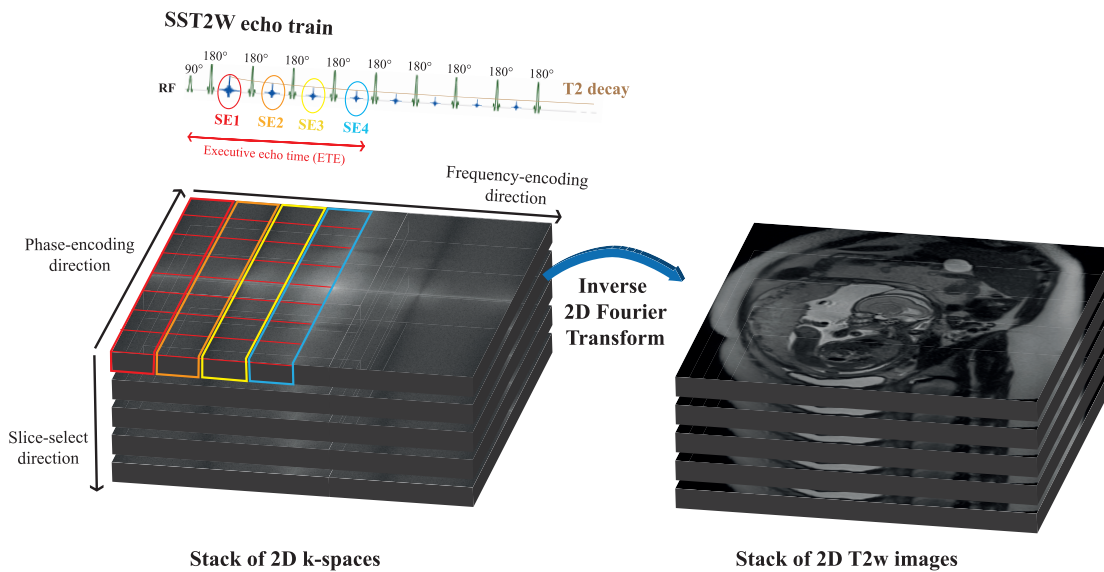


Figure 1 – Single-shot T2-weighted MR imaging principles. It consists of acquiring one k-space representation for each slice which is usually a 256×256 matrix, resulting in a stack of k-space (left); each of the line is occupied by one echo and each of the 256 values per line is occupied by an individual sample of transverse magnetization, measured after one slice selective excitation 90° RF pulse [28, 30]. This 90° RF pulse tips the equilibrium longitudinal magnetization from a slice of spins into the plane perpendicular to the main magnetic field, known as the “transverse plane”. It is followed by a series of slice selective refocusing 180° (theoretically), each of which leads to the generation of a “spin-echo” that undergoes T2 decay, the decay of transverse magnetization due to spins getting out of phase. Then, each spin-echo is acquired using RF coils during the frequency encoding which is preceded and followed by appropriate “wind” and “rewind” phase encode gradients such that it forms a line in k-space. Individual spin-echo duration (TE) is on the order of 2 to 3ms. After acquisition of all echoes, which happens after $TE \times \text{number of frequency encodings to acquire}$ ($256 \times [2 - 3]ms \approx [500 - 800]ms$), k-space is completely filled and the anatomic image is generated using 2D inverse Fourier transform (right).

0.7×0.7 to $2 \times 2mm^2$ and slice thicknesses from 2 to 4mm, largely free of intra-scan motion artifacts. In practice, several multi-slice scans are acquired, often in different orthogonal views (Figure 1.1) in order to provide the in utero three dimensional fetal anatomy in a short acquisition time.

Limitations Despite fast acquisition, motion remains and mostly generates inter-slice artifacts (see views orthogonal to the in-plane dimensions in Figure 1.1) as well as in-plane degradation. In addition, acquired images suffer from significant intensity inhomogeneity artifacts mainly due to both spin history and the proximity from the receiver coils of the fetal brain imaged, whose location varies when the fetus is moving. Finally, the partial volume effect, which arises when the interface between two different tissues occur within a single

voxel, is highly pronounced due to thick-slice acquisition. This complicates the diagnostic tasks of radiologists and this limits the use of computer-assisted methods for large-scale studies. As previously stated, a motion-free MR image of the fetal brain with isotropic high resolution would be highly desired and this introduces the next section.

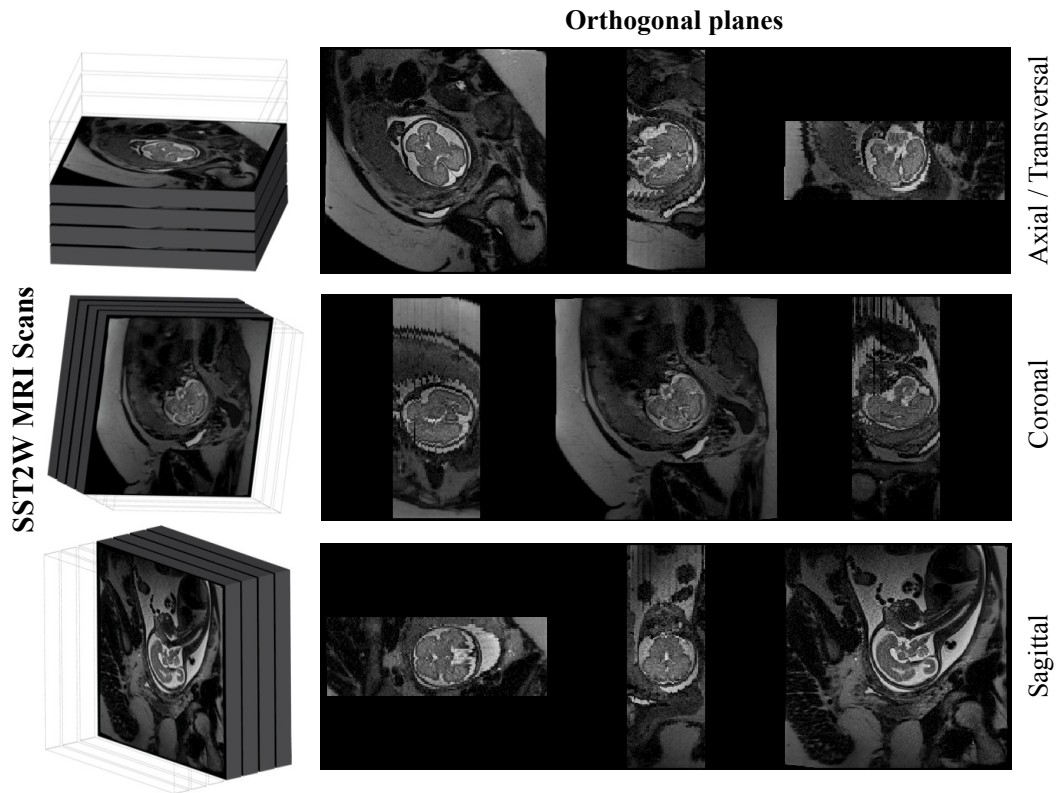


Figure 2 – Clinical orthogonally-planned MRI scans of fetus of 27 weeks of gestational age. Acquisitions were done with a Siemens Skyra 3*Tesla*, HASTE (SST2W) sequence (TR: 1600ms, TE: 116ms, slice thickness: 2.0mm, in-plane resolutions: $1.0 \times 1.0mm^2$).

Towards a motion-free high-resolution image

Higher resolution is the key to reduce partial volume effect, allowing a more accurate visualization of the anatomy and a more accurate assessment of size and morphology of organs and pathologies. In recent years, major advances in the image and video processing domains indicating the possibility of improving resolution using “Super-Resolution” (SR) algorithms [31] have motivated several research groups to start addressing resolution improvement in MRI as a post-acquisition image-processing challenge. SR deals with the task of taking benefits from aliasing occurring in several low-resolution (LR) images acquired by a specific imaging system (acquisition or forward model), which typically represents different “looks” of the object from a slightly shifted field-of-view (FOV), to estimate the high-resolution (HR) image (Figure 3). Resolution in multi-slice MRI scans is anisotropic and aliasing artifacts caused by

poor spatial resolution usually appear such as staircase effects along sharp edges. According to the sampling theorem, aliasing occurs when an image is sampled at a frequency lower than twice the Nyquist frequency (maximum frequency observed in the image) which converts high frequencies from the original HR image into low frequencies in the sampled image. Such aliased frequencies can no longer be distinguished from accurate low frequency signals. But indeed they still contain precious information about the high frequency content of the scene. Extracting aliased content is a major advantage for SR over standard interpolation techniques.

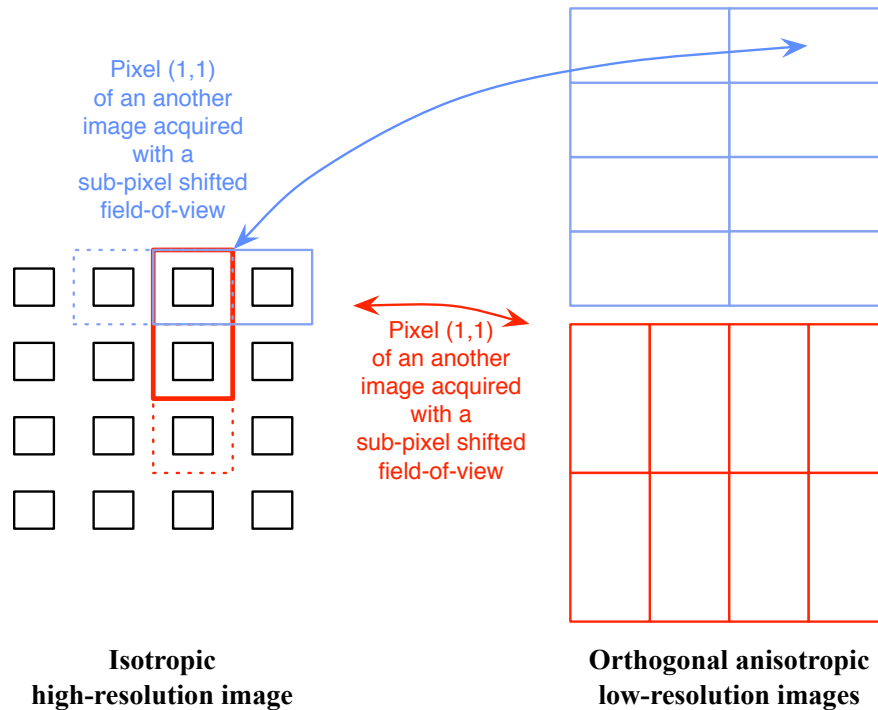


Figure 3 – Principle of super-resolution from anisotropic low-resolution images.

SR in magnetic resonance imaging A variety of SR algorithms have been proposed and successfully applied to MR imaging data [32], where the common objective is to accurately estimate the HR image while minimizing noise and preserving important image constraints. Their advantage over single HR acquisition has been proven in terms of higher SNR for a given acquisition time [33]. SR techniques were initially dedicated to *static* subjects where several low-resolution volumes were acquired with motion between them is controlled by employing spatial subpixel shifted FOVs. While most the works have proposed SR to enhance the resolution in the slice-select dimension and the success is clear and theoretically explained [32], a debate still exists in the SR community about the feasibility of enhancing the resolution in the in-plane dimensions [34–36]. Due to the theoretical nature of MR data, MR images are bandlimited since it can be expressed in Fourier basis with a finite number of coefficients, corresponding to each acquired sample in its k-space representation. Consequently, spatial

subpixel FOV shift in the in-plane dimension would only correspond to linear phase modulation in the k-space, if the FOV and the MR signal digitalization are unchanged. Indeed this infers that no new frequency content is acquired. Despite this controversy, it is clear from existing results that combining in-plane FOV shifted images does improve the signal-to-ratio (SNR), which enhances image quality especially in the case of noisy data [35]. Moreover, few works suggested that new information (although very small) may still be present in the frequency encoding (“readout”) direction in each new scans if the imaged object is *shifted prior* to imaging [37–39].

Application to in-utero fetal imaging Focus has been recently applied to SR of *moving* subjects, with major application to in-utero fetal MRI where current SST2W scans are highly anisotropic and fetal motion is unpredictable and likely to occur between scans and even between slices. Under these conditions, the need of advanced retrospective image processing techniques to enhance spatial resolution while correcting for motion is of great importance. Most of the works assumed the fetal head to be a rigid moving object and were dedicated to the through-plane resolution improvement. They consist of two common image processing steps: *image registration* (motion estimation for the super-resolution acquisition model) and *super-resolution (SR)*¹ (for image recovery), that solves the so-called *inverse problem* (see Figures 3 and 4 and Chapter 1).

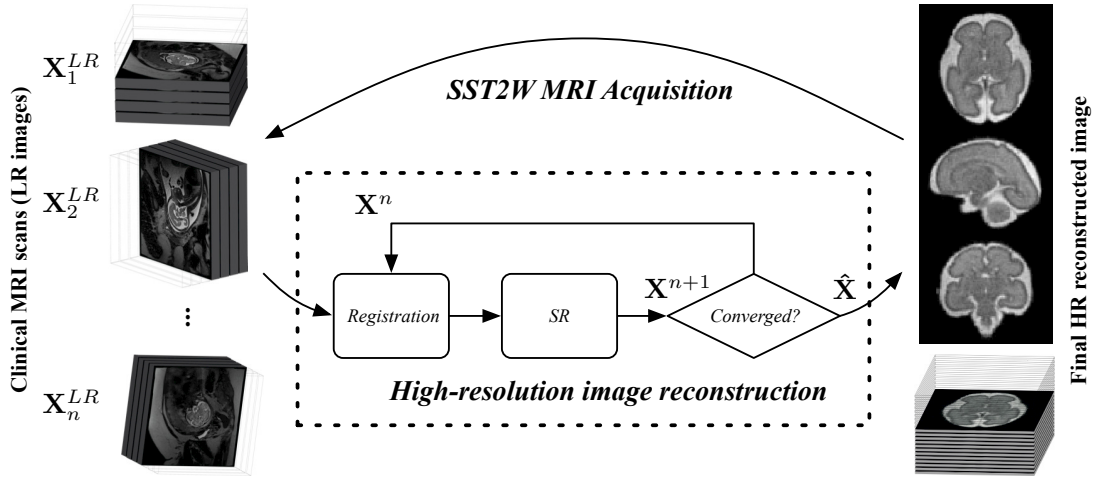


Figure 4 – General paradigm for direct and iterative fetal brain MR image reconstruction which relates anisotropic acquired scan X_k^{LR} and the HR image \hat{X} through the forward (image degradation) model. Two iterative steps are considered until convergence: 1) an image registration process for motion parameters estimation; 2) a super-resolution (SR) process for HR image recovery.

Two main registration methods have been proposed to estimate inter-stack and inter-slice

¹All through the thesis we will denote this step indistinctly by SR, image recovery and restoration. Let us note that this step has to be differentiated from *reconstruction* or *slice-to-volume reconstruction* that, in this work, refers to both motion estimation and image recovery steps.

fetal motions. The most common technique is slice-to-volume registration, where slices are iteratively registered to an estimation of the reconstructed 3D volume, allowing the refinement of the slice alignment [7, 10, 13]. A second approach proposed by [40] formulates the motion correction problem as the optimization of the intersections of all slice pairs from all orthogonal scans, which consequently does not require the estimation of the 3D image as motion estimation progresses.

Several SR methods have been proposed to restore the HR image. The pioneer approaches addressed this problem through iterative slice-to-volume registration and scattered data interpolation using a local neighborhood Gaussian [7] or a cubic B-Spline [8] kernel. However, those approaches employ different fitting criterion for image reconstruction and slice alignment, which results in a lack of any guarantee of overall convergence and may induce blurring in the interpolation-based SR step. It has thus encouraged the authors in [9] to introduce a Tikhonov-regularized inverse problem for SR, which gave to SR in fetal MRI a general deterministic framework with mathematical proof of overall convergence, and which allowed the introduction of spatial priors through regularization and the reconstruction of HR images with finer details. However, Tikhonov regularization poses smoothness constraints on the reconstruction that may result in excessive smoothing.

This has motivated several groups to refine the formulation based on the approximated Total Variation (ϵ -TV) regularization [12, 13] and Non-Local Means (NLM) [15]. In addition, intensity level of the same anatomy imaged can be inconsistent between different slice views due to spin-history (sudden fetal motion during the slice acquisition) and the B0 bias field effect. It has encouraged the community to develop more robust formulations that can minimize or totally exclude the contribution of highly corrupted and misregistered slices [10, 11, 13] and correct for intensity inhomogeneities [7, 13]. A last and rather different approach was introduced in [11] based on slice intersection motion correction combined with a gradient-weighted averaging technique for image estimation. It was further improved in [14] within a unified motion estimation / SR formulation by optimizing a single energy minimization process.

All these methods rely on localizing and extracting the fetal brain (rigid component) from surrounding maternal tissues (non-rigid components) as a preprocessing step to ensure the success of the subsequent image processing algorithms. Consequently, they can successfully reconstruct only a partial FOV containing the brain. Recently, a GPU implementation has enabled the exact computation of the acquisition model for every voxel in the scans [16] and the possibility to reconstruct the whole FOV by splitting slices into overlapping patches (which contain rigid components) and performing patch-to-volume registration and SR reconstruction [41], in an acceptable amount of time. In the case of fetal brain studies, reconstructing a partial FOV containing the brain benefits nonetheless from computational advantages over reconstructing the full FOV.

Formulation based on ϵ -TV regularization has attracted most of the active research groups

as it allows to use a simple gradient descent technique for optimization but it is very slow to converge towards the solution if one wishes to recover well edges. However, fast TV-based algorithms based on convex optimization theory have been developed in the last years. I will present in Chapter 1 a new efficient primal-dual SR algorithm for fetal MRI reconstruction based on exact TV regularization and fast convex optimization. An other concern in fetal MRI reconstruction is the brain localization and extraction step which is essential to guarantee the quality of the reconstruction. This step corresponds to the most important effort spent by the user since it is typically done manually or semi-automatically. Only few methods have addressed this automatization problem by adopting either template-based segmentation [42–46] or machine learning techniques [47–50]. I will present in Chapter 2 a novel brain localization and extraction approach based on template-to-slice block matching and deformable slice-to-template registration which has been integrated in the reconstruction pipeline. I will finally present in Chapter 4 new recent improvements that could allow a more accurate image analysis tasks. They consist of the development of a more consistent bias field inhomogeneity correction, the extension of the TV SR algorithm to resolution improvement in the in-plane dimensions, the development of a new robust TV SR algorithm which uses the robust Huber norm in the data fidelity term to deal with outliers as well as a new segmentation-driven TV SR algorithm which incorporates of discriminative Gaussian mixture models.

Such reconstructions have already proven to open new perspectives for the neuroimaging research [51] and to improve the efficacy of clinical evaluation [52]. They has recently stimulated new research aiming at, amongst others, to have a better understanding of early brain development and maturation.

Automatic segmentation and quantification of fetal brain

The development of motion robust SR fetal MRI offers new opportunities to quantitatively analyze fetal brain MR images. The first and essential step in fetal brain quantitative analysis is tissue segmentation. It consists of automatically segmenting tissues, such as grey matter (GM), white matter (WM), cerebrospinal fluid (CSF) surrounding the brain, whose appearance changes rapidly, or structures, such as ventricles, whose size and shape highly vary, in images adversely affected by motion artifacts, and severe intensity inhomogeneity artifacts. Many automated segmentation methods have been suggested for MR images of the adult, mainly based on the intensity with strong anatomical priors. However they cannot be directly adapted to fetal MR images, since many assumptions in adults do not hold in images of the fetal brain. Firstly, T2w contrast used to visualize the fetal brain anatomy differs from T1w contrast used to visualize the adult brain anatomy. Secondly, the fetal brain at early to mid gestational ages grows and develops at rapid pace leading to transient tissue regions (ventricular and subventricular germinal matrices, subplate, intermediate zone, and cortical plate) that do not exactly correspond to the traditional white and gray matter of the late gestation fetal brain [53].

Once the segmentation of the tissue or structure of interest has been performed, further brain

analysis consists in extracting biomarkers, e.g. quantitatively analyzing the fetal brain MR images. Quantitative analysis of the early brain development is specific to the application. It is the key to facilitate the diagnosis and prognosis of brain anomalies. For instance, segmentation of the ventricles have been used to compute ventricular volumetry, which have shown to be an excellent quantitative indicator of severe forms of ventriculomegaly [54]. Quantification of normal cortical folding patterns over a wide GA range from 22 to 39 enabled the modeling of the increase in folding measures with GA, which has shown in turn to be an accurate predictor of GA from folding measures [42].

To date, several works have addressed automated segmentation and quantification of fetal brain MR images, mainly using a spatio-temporal atlas-based approach. The first work extended the popular atlas-based expectation-maximization segmentation with a standard Markov random field regularization (EM-MRF) approach for adult brain images [55] to the segmentation of the fetal brain [17, 56]. The proposed framework consisted of building a spatio-temporal atlas of tissue distribution and MR template of the fetal brain, registering the target brain to the age-specific MR template and using the corresponding propagated tissue probability map as spatial priors for automatic EM-MRF-based tissue segmentation of the target brain.

This segmentation framework has been successfully employed in young fetuses ranging from 20 to 30 weeks gestational age (GA) in a number of quantitative studies in the case of normal growth [19, 20, 57] and in the case of abnormal growth seen in isolated mild ventriculomegaly [58]. Although the previous EM-MRF techniques that incorporated a standard MRF penalization term had shown to be sufficient to segment the young fetal brain, the standard MRF, which penalized a specific tissue class based on its adjacency with one other specific classe, did not explicitly address the problem of mislabelled partial volume voxels which could result in poor performance at the cortical boundary. However, this would be essential for accurately segmentating older fetal brains, which consists of more complex cortical structures. The EM-MRF technique was recently improved by adding an additional second order MRF penalization term, which could penalize a specific tissue class based on its adjacency with two other specific classes, and was successfully applied to extract cortical surfaces and quantify normal cortical folding patterns over a wide GA range from 22 to 39 weeks [42]. It was subsequently extended to the construction of a spatio-temporal cortical surface atlas [59]. Finally, an accurate volumetric study of severe forms of fetal ventriculomegaly in a wide GA range was performed based on a novel probabilistic framework combining a robust multi-atlas strategy with shape-constrained optimization [54].

Despite EM-MRF approaches have demonstrated to perform well on normal brains, they are based on strong anatomical priors coming from the atlas which may introduce a *risk of circularity* as each brain is deformed to the atlas template with potentially biased results, especially for pathological data. Only few works have investigated topological priors to avoid this risk. The first attempt proposed to perform an initial Bayesian segmentation followed by a three-step MRF model that introduced both local spatial priors and anatomical priors given by

a cortical distance map [60]. A supervised approach, based on intensity-based classification, connected components labeling, morphological filtering, and geodesic active contours level set segmentation, was developed for the segmentation of the pericerebral fluid spaces [61]. An other method was developed for cortex segmentation, which included structural constraints based on a topological model to define a region of interest including the cortex, and which used a morphological filter to identify the regions where the cortex appears the most likely [62]. Chapter 3 will investigate the possibility of automatic quantification of cortical folding by (1) employing the robust multi-atlas multi-shape segmentation method [54] to extract the WM volume from our reconstructed images and (2) taking advantages of existing tools for the study of cortical folding in adult brains to extract cortical surfaces and compute cortical folding features.

Thesis outline and contributions

In this thesis, I present a *complete* reconstruction pipeline with novel advanced image processing methods that improves *state-of-the-art* fetal MRI reconstruction in terms of efficiency, robustness and minimized user-interactions.

Chapter 1 will present and validate **an efficient SR algorithm that combines exact Total Variation (TV) regularization with fast convex optimization**. Results will show the algorithm is more efficient, as it is optimal in the sense of convex optimization theory, and more robust to motion estimation errors than Tikhonov- and approximated TV-regularized based algorithms. Chapter 1 will also give a more formal description of the SR problem in fetal MRI and an overview of the existing SR algorithms within an unified formulation.

Chapter 2 will present and validate **a novel age-matched template-based method based on template-to-slice block matching and deformable slice-to-template registration for brain localization and extraction automatization**, two inherent steps in most existing SR methods that are commonly performed either manually or semi-automatically. The method has been integrated in **a novel automatic reconstruction framework which combines the masking process with intensity standardization, motion correction, and SR reconstruction**. In the proposed framework the brain masks are refined in the spatial space of the template using a consensus fusion voting process and are re-applied to the scans as the reconstruction proceeds. Results will show the proposed approach allow brain extraction to take into account for inter-slice motion and thus is more robust than a global rigid 3D template-registration-based approach. It will be also demonstrated that the proposed automatic pipeline allows us to achieve similar reconstruction quality to reference reconstruction based on manually drawn masks without any effort.

Chapter 3 will investigate the possibility of **automatic cortical folding quantification by combining our automatic reconstruction pipeline**, as described in Chapter 2, **with the state-of-the-art multi-atlas multi-segmentation method [54] and existing automated tools provided for adult brain's cortical folding quantification**. Results will indicate that our recon-

Thesis outline and contributions

struction pipeline can provide HR MR images with sufficient quality that enables the use of surface tessellation and active surface algorithms similar to those developed for adult brains to extract meaningful information about fetal brain maturation.

Chapter 4 will present new improvements that can potentially improve reconstruction quality, segmentation accuracy and quantification accuracy, whose success is highly inter-dependent. Specifically, it will present **a more consistent and global magnetic bias field correction method which takes advantage of the super-resolution framework** to provide a final reconstructed image quasi free of the smooth bias field. Chapter 4 will present **a new TV SR algorithm based on the Huber norm** that should be more robust to misaligned outlier slices. Chapter 4 will also present **a novel joint reconstruction-segmentation framework which uses a new segmentation-driven TV SR algorithm** that incorporates a discriminative Gaussian mixture modeling estimated from segmentation. Such an approach could produce images with enhanced edge information that could ultimately improve their segmentation. Finally, Chapter 4 will **preliminary investigate the capability of increasing the resolution in the in-plane dimensions using SR** to ultimately reduce the partial volume effect by refining the mapping between voxels in the scans and voxels in the reconstructed HR image.

Chapter 5 will draw the conclusion and will discuss about different future perspectives.

Annex ?? will present the **C++ software Medical Image Analysis Laboratory Toolbox (MI-ALTK)** based on the open-source Insight ToolKit (ITK) library [63]. It consists of the implementation of all algorithms and methods developed in this thesis. The toolbox provides therefore **tools for the entire reconstruction pipeline** in order to automatically, efficiently and robustly reconstruct HR MR image of the fetal brain.

Bibliography

- [1] F. W. Smith, A. H. Adam, W. D. P. Phillips, NMR imaging in pregnancy, *The Lancet* 321 (8314) (1983) 61–62.
- [2] F. V. Coakley, O. A. Glenn, A. Qayyum, A. J. Barkovich, R. Goldstein, R. A. Filly, Fetal MRI: a developing technique for the developing patient, *American Journal of Roentgenology* 182 (1) (2004) 243–252.
- [3] C. Garel, The role of MRI in the evaluation of the fetal brain with an emphasis on biometry, gyration and parenchyma, *Pediatric Radiology* 34 (9) (2004) 694–699.
- [4] D. Levine, *Atlas of Fetal MRI*, Taylor & Francis, 2005.
- [5] E. M. Simon, R. B. Goldstein, F. V. Coakley, R. A. Filly, K. C. Broderick, T. J. Musci, A. J. Barkovich, Fast MR imaging of fetal CNS anomalies in utero, *American Journal of Neuro-radiology* 21 (9) (2000) 1688–1698.
- [6] O. A. Glenn, MR imaging of the fetal brain, *Pediatric Radiology* 40 (1) (2010) 68–81.
- [7] F. Rousseau, O. A. Glenn, B. Iordanova, C. Rodriguez-Carranza, D. B. Vigneron, J. A. Barkovich, C. Studholme, Registration-based approach for reconstruction of high-resolution in utero fetal MR brain images, *Academic Radiology* 13 (9) (2006) 1072–1081.
- [8] S. Jiang, H. Xue, A. Glover, M. Rutherford, D. Rueckert, J. Hajnal, MRI of moving subjects using multislice snapshot images with volume reconstruction (SVR): Application to fetal, neonatal, and adult brain studies, *Medical Imaging, IEEE Transactions on* 26 (7) (2007) 967–980.
- [9] A. Gholipour, S. K. Warfield, Super-resolution reconstruction of fetal brain MRI, in: *MICCAI Workshop on Image Analysis for the Developing Brain (IADB'2009)*, 2009, pp. 45–52.
- [10] A. Gholipour, J. Estroff, S. Warfield, Robust super-resolution volume reconstruction from slice acquisitions: Application to fetal brain MRI, *Medical Imaging, IEEE Transactions on* 29 (10) (2010) 1739–1758.
- [11] K. Kim, P. Habas, F. Rousseau, O. Glenn, A. Barkovich, C. Studholme, Intersection based motion correction of multislice MRI for 3-D in utero fetal brain image formation, *Medical Imaging, IEEE Transactions on* 29 (1) (2010) 146–158.
- [12] F. Rousseau, K. Kim, C. Studholme, M. Koob, J. Dietemann, On super-resolution for fetal brain MRI, in: T. Jiang, N. Navab, J. Pluim, M. Viergever (Eds.), *Medical Image Computing and Computer Assisted Intervention (MICCAI), International Conference on*, Vol. 6362 of *Lecture Notes in Computer Science*, Springer, 2010, pp. 355–362.

Bibliography

- [13] M. Kuklisova-Murgasova, G. Quaghebeur, M. A. Rutherford, J. V. Hajnal, J. A. Schnabel, Reconstruction of fetal brain MRI with intensity matching and complete outlier removal, *Medical Image Analysis* 16 (8) (2012) 1550–1564.
- [14] M. Fogtman, S. Seshamani, K. Kim, T. Chapman, C. Studholme, A unified approach for motion estimation and super resolution reconstruction from structural magnetic resonance imaging on moving objects, in: *MICCAI workshop on Perinatal and Paediatric Imaging: PaPI*, 2012, pp. 9–16.
- [15] F. Rousseau, E. Oubel, J. Pontabry, M. Schweitzer, C. Studholme, M. Koob, J.-L. Dietemann, BTK: An open-source toolkit for fetal brain MR image processing, *Computer Methods and Programs in Biomedicine* 109 (1) (2013) 65–73.
- [16] B. Kainz, M. Steinberger, W. Wein, M. Kuklisova-Murgasova, C. Malamateniou, K. Ker-audren, T. Torsney-Weir, M. Rutherford, P. Aljabar, J. V. Hajnal, et al., Fast volume reconstruction from motion corrupted stacks of 2D slices, *Medical Imaging, IEEE Transactions on* 34 (9) (2015) 1901–1913.
- [17] P. A. Habas, K. Kim, F. Rousseau, O. A. Glenn, A. J. Barkovich, C. Studholme, A spatio-temporal atlas of the human fetal brain with application to tissue segmentation, in: *Medical Image Computing and Computer Assisted Intervention (MICCAI), International Conference on*, Vol. 12, 2009, pp. 289–296.
- [18] A. Gholipour, C. Limperopoulos, S. Clancy, C. Clouchoux, A. Akhondi-Asl, J. A. Estroff, S. K. Warfield, Construction of a deformable spatiotemporal MRI atlas of the fetal brain: Evaluation of similarity metrics and deformation models, in: P. Golland, N. Hata, C. Barillot, J. Hornegger, R. Howe (Eds.), *Medical Image Computing and Computer Assisted Intervention (MICCAI), International Conference on*, Vol. 8674 of *Lecture Notes in Computer Science*, Springer, 2014, pp. 292–299.
- [19] P. A. Habas, J. A. Scott, A. Roosta, V. Rajagopalan, K. Kim, F. Rousseau, A. J. Barkovich, O. A. Glenn, C. Studholme, Early folding patterns and asymmetries of the normal human brain detected from in utero MRI, *Cerebral Cortex* 22 (1) (2012) 13–25.
- [20] J. A. Scott, P. A. Habas, K. Kim, V. Rajagopalan, K. S. Hamzelou, J. M. Corbett-Detig, A. J. Barkovich, O. A. Glenn, C. Studholme, Growth trajectories of the human fetal brain tissues estimated from 3D reconstructed in utero MRI, *International Journal of Developmental Neuroscience* 29 (5) (2011) 529–536.
- [21] J. Corbett-Detig, P. Habas, J. Scott, K. Kim, V. Rajagopalan, P. McQuillen, A. Barkovich, O. Glenn, C. Studholme, 3D global and regional patterns of human fetal subplate growth determined in utero, *Brain Structure and Function* 215 (2011) 255–263.
- [22] C. Studholme, Mapping fetal brain development in utero using MRI: The big bang of brain mapping, *Annual review of biomedical engineering* 13 (2011) 345–368.

- [23] C. Clouchoux, D. Kudelski, A. Gholipour, S. K. Warfield, S. Viseur, M. Bouyssi-Kobar, J.-L. Mari, A. C. Evans, A. J. Du Plessis, C. Limperopoulos, Quantitative in vivo MRI measurement of cortical development in the fetus, *Brain Structure and Function* 217 (1) (2012) 127–139.
- [24] C. Clouchoux, A. Du Plessis, M. Bouyssi-Kobar, W. Tworetzky, D. McElhinney, D. Brown, A. Gholipour, D. Kudelski, S. Warfield, R. McCarter, et al., Delayed cortical development in fetuses with complex congenital heart disease, *Cerebral Cortex* 23 (12) (2013) 2932–2943.
- [25] D. Prayer, *Fetal MRI*, Springer, 2011.
- [26] Y. Yamashita, T. Namimoto, Y. Abe, M. Takahashi, J. Iwamasa, K. Miyazaki, H. Okamura, MR imaging of the fetus by a haste sequence., *American Journal of Roentgenology* 168 (2) (1997) 513–519.
- [27] P. N. Baker, I. R. Johnson, P. A. Gowland, J. Hykin, P. R. Harvey, A. Freeman, V. Adams, P. Mansfield, B. S. Worthington, Fetal weight estimation by echo-planar magnetic resonance imaging, *The Lancet* 343 (8898) (1994) 644–645.
- [28] A. Gholipour, J. A. Estroff, C. E. Barnewolt, R. L. Robertson, P. E. Grant, B. Gagoski, S. K. Warfield, O. Afacan, S. A. Connolly, J. J. Neil, et al., Fetal MRI: A technical update with educational aspirations, *Concepts in Magnetic Resonance Part A* 43 (6) (2014) 237–266.
- [29] E. M. Haacke, R. W. Brown, M. R. Thompson, R. Venkatesan, *Magnetic resonance imaging : physical principles and sequence design*, Wiley, 1999.
- [30] R. F.J., M. R.V., Principles and clinical applications of single-shot magnetic resonance imaging (editorial), *Applied Radiology* 30 (Supp 1) (2001) 30–34.
- [31] J. Yang, T. Huang, *Image super-resolution: historical overview and future challenges, from the book: Super-Resolution Imaging* (edited by Peyman Milanfar), CRC Press (Taylor & amp and Francis Group), 2011.
- [32] E. Van Reeth, I. W. K. Tham, C. H. Tan, C. L. Poh, Super-resolution in magnetic resonance imaging: A review, *Concepts in Magnetic Resonance Part A* 40A (6) (2012) 306–325.
- [33] E. Plenge, D. H. J. Poot, M. Bernsen, G. Kotek, G. Houston, P. Wielopolski, L. van der Weerd, W. J. Niessen, E. Meijering, Super-resolution methods in MRI: Can they improve the trade-off between resolution, signal-to-noise ratio, and acquisition time?, *Magnetic Resonance in Medicine* 68 (6) (2012) 1983–1993.
- [34] K. Scheffler, Superresolution in MRI?, *Magnetic Resonance in Medicine* 48 (2) (2002) 408–408.
- [35] Q. M. Tieng, G. J. Cowin, D. C. Reutens, G. J. Galloway, V. Vegh, Mri resolution enhancement: How useful are shifted images obtained by changing the demodulation frequency?, *Magnetic Resonance in Medicine* 65 (3) (2011) 664–672.

Bibliography

- [36] M. Uecker, T. J. Sumpf, J. Frahm, Reply to: MRI resolution enhancement: How useful are shifted images obtained by changing the demodulation frequency?, *Magnetic Resonance in Medicine* 66 (6) (2011) 1511–1512.
- [37] E. Carmi, S. Liu, N. Alon, A. Fiat, D. Fiat, Resolution enhancement in MRI, *Magnetic Resonance Imaging* 24 (2) (2006) 133–154.
- [38] G. S. Mayer, E. R. Vrscaj, *Mathematical Analysis of “Phase Ramping” for Super-Resolution Magnetic Resonance Imaging*, Springer, 2006, pp. 82–93.
- [39] J. Mitchell, G. Mayer, M. Lauzon, H. Zhu, Synthetic aperture MRI, uS Patent 7,005,854 (Feb. 28 2006).
URL <https://www.google.com/patents/US7005854>
- [40] K. Kim, M. Hansen, P. Habas, F. Rousseau, O. Glenn, A. Barkovich, C. Studholme, Intersection based registration of slice stacks to form 3d images of the human fetal brain, in: *Biomedical Imaging: From Nano to Macro, 2008. ISBI 2008. 5th IEEE International Symposium on*, 2008, pp. 1167–1170.
- [41] B. Kainz, A. Alansary, C. Malamateniou, K. Keraudren, M. Rutherford, J. Hajnal, D. Rueckert, Flexible reconstruction and correction of unpredictable motion from stacks of 2d images, in: *Medical Image Computing and Computer Assisted Intervention (MICCAI), International Conference on, Lecture Notes in Computer Science*, Springer, 2015, pp. 555–562.
- [42] R. Wright, V. Kyriakopoulou, C. Ledig, M. Rutherford, J. Hajnal, D. Rueckert, P. Aljabar, Automatic quantification of normal cortical folding patterns from fetal brain MRI, *NeuroImage* 91 (0) (2014) 21–32.
- [43] J. Anquez, E. D. Angelini, I. Bloch, Automatic segmentation of head structures on fetal MRI., in: *Biomedical Imaging (ISBI), International Symposium on, IEEE*, 2009, pp. 109–112.
- [44] Y. Taleb, M. Schweitzer, C. Studholme, M. Koob, J.-L. Dietemann, F. Rousseau, Automatic template-based brain extraction in fetal MR images, in: *Organization for Human Brain Mapping (OHBM) conference.*, 2013.
- [45] S. Tourbier, P. Hagmann, M. Cagneaux, L. Guibaud, S. Gorthi, M. Schaer, J.-P. Thiran, R. Meuli, M. B. Cuadra, Automatic brain extraction in fetal MRI using multi-atlas-based segmentation, in: *Proc. SPIE Medical Imaging*, Vol. 9413, 2015, pp. 94130Y–94130Y–7.
- [46] V. Taimouri, A. Gholipour, C. Velasco-Annis, J. Estroff, S. K. Warfield, A template-to-slice block matching approach for automatic localization of brain in fetal MRI, in: *Biomedical Imaging (ISBI), International Symposium on, IEEE*, 2015, pp. 144–147.
- [47] M. Ison, E. Dittrich, R. e. Donner, G. Kasprian, D. Prayer, G. Langs, Fully automated brain extraction and orientation in raw fetal MRI, *MICCAI workshop on Perinatal and Paediatric Imaging: PaPI* (2012) 17–24.

- [48] K. Keraudren, V. Kyriakopoulou, M. A. Rutherford, J. V. Hajnal, D. Rueckert, Localisation of the brain in fetal MRI using bundled SIFT features., in: K. Mori, I. Sakuma, Y. Sato, C. Barillot, N. Navab (Eds.), *Medical Image Computing and Computer Assisted Intervention (MICCAI)*, International Conference on, Vol. 8149 of *Lecture Notes in Computer Science*, Springer, 2013, pp. 582–589.
- [49] B. Kainz, K. Keraudren, V. Kyriakopoulou, M. Rutherford, J. V. Hajnal, D. Rueckert, Fast fully automatic brain detection in fetal MRI using dense rotation invariant image descriptors, in: *Biomedical Imaging (ISBI)*, International Symposium on, IEEE, 2014, pp. 1230–1233.
- [50] K. Keraudren, M. Kuklisova-Murgasova, V. Kyriakopoulou, C. Malamateniou, M. Rutherford, B. Kainz, J. Hajnal, D. Rueckert, Automated fetal brain segmentation from 2D MRI slices for motion correction, *NeuroImage* 101 (2014) 633–643.
- [51] C. Studholme, F. Rousseau, Quantifying and modelling tissue maturation in the living human fetal brain, *International Journal of Developmental Neuroscience* 32 (2014) 3 – 10, special Issue: *Imaging Developing Brain*.
- [52] M. Rutherford, S. Jiang, J. Allsop, L. Perkins, L. Srinivasan, T. Hayat, S. Kumar, J. Hajnal, MR imaging methods for assessing fetal brain development, *Developmental Neurobiology* 68 (6) (2008) 700–711.
- [53] I. Kostovic, M. Judaš, M. Rados, P. Hrabac, Laminar organization of the human fetal cerebrum revealed by histochemical markers and magnetic resonance imaging, *Cerebral Cortex* 12 (5) (2002) 536–544.
- [54] A. Gholipour, A. Akhondi-Asl, J. A. Estroff, S. K. Warfield, Multi-atlas multi-shape segmentation of fetal brain MRI for volumetric and morphometric analysis of ventriculomegaly, *NeuroImage* 60 (3) (2012) 1819–1831.
- [55] K. Van Leemput, F. Maes, D. Vandermeulen, P. Suetens, Automated model-based tissue classification of MR images of the brain, *Medical Imaging, IEEE Transactions on* 18 (10) (1999) 897–908.
- [56] P. A. Habas, K. Kim, F. Rousseau, O. A. Glenn, A. J. Barkovich, C. Studholme, Atlas-based segmentation of developing tissues in the human brain with quantitative validation in young fetuses, *Human Brain Mapping* 31 (9) (2010) 1348–1358.
- [57] V. Rajagopalan, J. Scott, P. A. Habas, K. Kim, J. Corbett-Detig, F. Rousseau, A. J. Barkovich, O. A. Glenn, C. Studholme, Local tissue growth patterns underlying normal fetal human brain gyrification quantified in utero, *The Journal of neuroscience : the official journal of the Society for Neuroscience* 31 (8) (2011) 2878–2887.
- [58] J. A. Scott, K. S. Hamzelou, V. Rajagopalan, P. A. Habas, K. Kim, A. J. Barkovich, O. A. Glenn, C. Studholme, 3d morphometric analysis of human fetal cerebellar development, *Cerebellum (London, England)* 11 (3) (2012) 761–770.

Bibliography

- [59] R. Wright, A. Makropoulos, V. Kyriakopoulou, P. Patkee, L. Koch, M. Rutherford, J. Hajnal, D. Rueckert, P. Aljabar, Construction of a fetal spatio-temporal cortical surface atlas from in utero MRI: Application of spectral surface matching, *NeuroImage* 120 (2015) 467 – 480.
- [60] M. B. Cuadra, M. Schaer, A. Andre, L. Guibaud, S. Eliez, J. Thiran, Brain tissue segmentation of fetal MR images, in: *MICCAI Workshop on Image Analysis for the Developing Brain (IADB)*, 2009.
- [61] A. Gholipour, J. A. Estroff, C. E. Barnewolt, S. A. Connolly, S. K. Warfield, Fetal brain volumetry through MRI volumetric reconstruction and segmentation, *International Journal of Computer Assisted Radiology and Surgery* 6 (3) (2011) 329–339.
- [62] B. Caldairou, N. Passat, P. A. Habas, C. Studholme, M. Koob, J.-L. Dietemann, F. Rousseau, Segmentation of the cortex in fetal MRI using a topological model, in: *Biomedical Imaging (ISBI), International Symposium on, IEEE*, 2011, pp. 2045–2048.
- [63] T. S. Yoo, M. J. Ackerman, W. E. Lorensen, W. Schroeder, V. Chalana, S. Aylward, D. Metaxas, R. Whitaker, Engineering and algorithm design for an image processing API: A technical report on ITK - the Insight Toolkit, in: J. Westwood (Ed.), *Proc. of Medicine Meets Virtual Reality*, Vol. 85, IOS Press Amsterdam, 2002, pp. 586–592.

1

An Efficient TV Algorithm for Super-Resolution in Fetal Brain MRI with Adaptive Regularization

The work in this chapter was originally published as [S. Tourbier, X. Bresson, P. Hagmann, J.-P. Thiran, R. Meuli, M. Bach Cuadra, “An Efficient Total Variation Algorithm for Super-Resolution in Fetal Brain MRI with Adaptive Regularization”, *NeuroImage* 2015 \(118\) , pp. 584-597, 2015.](#) A 8-page conference paper was previously peer-reviewed and presented as poster presentation at the International Conference on Medical Image Computing and Computer-Assisted Intervention (MICCAI) 2014 and published as [S. Tourbier, X. Bresson, P. Hagmann, J.-P. Thiran, R. Meuli, M. Bach Cuadra, “Efficient Total Variation Algorithm for Fetal Brain MRI Reconstruction”, *MICCAI 2014, Part II, LNCS 8674, pp. 252–259, 2014.*](#)

1.1 Introduction

Recent advances in clinical magnetic resonance imaging (MRI) provide an unprecedented opportunity to study the human brain growth *in-utero*. Concretely, T2-weighted (T2w) MR images have proven to provide the best ability to delineate structures and layers in fetal brain MRI [1–4]. Clinical MRI examination involves the use of ultra-fast multi-slices MR sequences, such as Half Fourier Acquisition Single-Shot Turbo Spin Echo (HASTE) or Single-Shot Fast Spin Echo (ssFSE) [5] to avoid as much as possible motion. In practice, these sequences are acquired as several stacks of thick slices, often in different orthogonal views (Figure 1.1 b)) in order to provide the *in-vivo* 3D fetal anatomy in a short acquisition time. This procedure has allowed a more regular use of fetal MR imaging in clinics, with an excellent in-plane spatial resolution (around 1 mm in-plane resolution with a slice thickness between 3 and 5 mm), very good tissue contrast and anatomical detail within the images while reducing motion artifacts (Figure 1.1 a)).

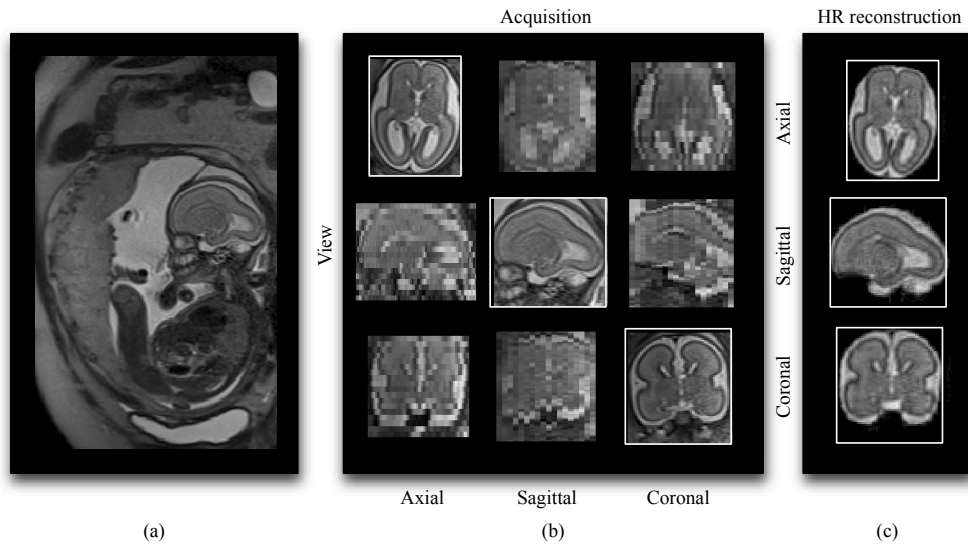


Figure 1.1 – Fetus of 25 weeks of gestational age: (a) Sagittal view of whole volume scan, (b) Orthogonal stacks in brain region. Acquisitions were done with a Siemens Aera 1.5Tesla, T2w HASTE sequence (TR 1200ms, TE 90ms, slice thickness 3.6mm, in-plane resolution 1.13mm), and (c) HR image of the fetal brain reconstructed by SR technique.

Although fetal anatomy can be adequately viewed in new multi-slice MR images, many critical limitations remain for quantitative data analysis. Despite these fast acquisition techniques, motion remains and mostly generates inter-slice artifacts (see top row, coronal view, in Figure 1.1 b) but also in-plane degradation. This limits the use of computer-assisted methods for large-scale studies. To this end, several research groups have recently developed advanced image processing methods, often denoted by super-resolution (SR) techniques, to reconstruct from several clinical stacks, low-resolution (LR) images, a high-resolution (HR) motion-free volume [6–14]. Such HR volume facilitates early and precise diagnosis (see Figure 1.1 c) and offers, to the neuroscientist, the possibility of an automated quantitative study of the first stages of brain development [15–18].

In the last years, SR algorithms have been successfully applied to MR imaging data [19] and their advantage over single HR acquisition has been proven in terms of higher SNR for a given acquisition time [20]. SR techniques were initially dedicated to *static* subjects where scanning protocol can be adapted to add new information of the scene under controlled motion conditions. More recently, focus has been applied to SR of *moving* subjects, where motion is not controlled. In these cases, the need of advanced post-processing techniques to enhance spatial resolution is of great importance. Most of these works assumed a rigid motion and they are dedicated to the through-plane resolution improvement of fetal MRI images, providing us a fully isotropic 3D image only limited by the in-plane resolution of the acquisition [6–14]. Thus, these methods consist of two common image processing steps: image registration (for motion compensation) and super-resolution¹ (for image recovery),

¹All through the paper we will denote this step indistinctly by super-resolution, image recovery and restoration.

that solves the so-called inverse problem (see Figure 1.2 and Section 1.3.3).

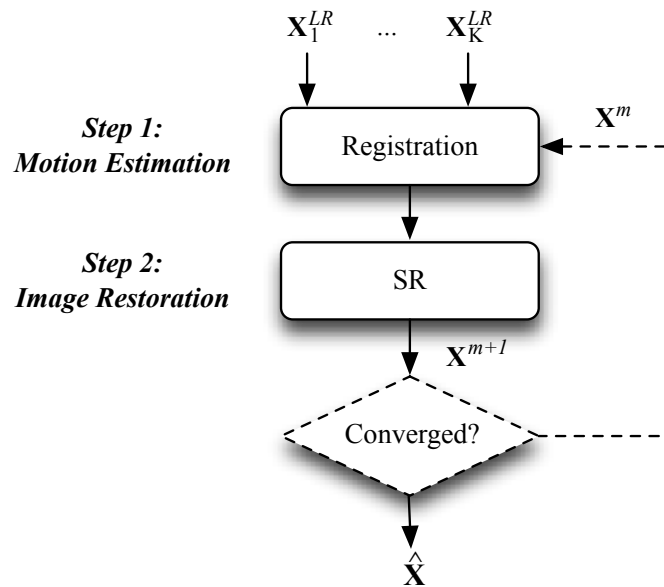


Figure 1.2 – General paradigm for direct and iterative fetal brain MR image reconstruction. Two iterative steps are considered until convergence: 1) a registration process for motion parameters estimation; 2) a restoration process for HR image recovery.

An objective of this chapter is to provide an overview of SR techniques in the case of fetal MRI. Along this line, our contribution differs from the recent review of Reeth-et.al. [19] that aimed at discussing SR MRI techniques in various contexts. Here we focus on the literature of SR fetal MRI algorithms in order to emphasize the similarities and differences between the successful Bayesian and variational formulations for this specific problem. We built on this overview of SR techniques and recent advances in convex optimization to present the optimization algorithm introduced in [21] that offers simultaneously fast, accurate and robust solutions to the fetal image recovery problem.

1.2 Contributions

- I have reviewed existing SR reconstruction algorithms for fetal MRI within a unified mathematical formulation.
- I have designed and implemented a fast, accurate and guaranteed-to-converge regularized-based SR algorithm for the fetal reconstruction problem that is based on the Total Variation (TV) energy.
- I have proposed an automatic process that estimates a near-visually optimal value for

Let us note that this step has to be differentiated from *reconstruction* that, in this work, refers to both motion estimation and image recovery steps.

the contribution weight of the TV regularization.

- I have extensively validated the SR algorithm on simulated fetal data and on a set of ten clinical fetal datasets of normal and pathological brains under various acquisition conditions, including:
 - a developed comparison between our model, the baseline Tikhonov model and the open-source state-of-the-art method [12],
 - a study of robustness of regularization terms w.r.t motion error residuals,

The chapter is organized as follows. Section 1.3 provides a short review of fetal MRI reconstruction, starting with the description of the most generic observation model used in this context. Section 1.4 recalls our TV algorithm presented in [21] and it describes the design and implementation of our reconstruction pipeline. Section 2.5 develops an extensive validation of our algorithm, using simulated fetal data and clinically acquired fetal data. Finally, a conclusion is presented in Section 2.7.

1.3 Overview of fetal MRI reconstruction algorithms

1.3.1 Notations and definitions

We consider the following discrete setting throughout the paper. Let \mathbf{X} denotes the high-resolution (HR) image desired, \mathbf{X}_{kl}^{LR} be the l -th observed slice of the k -th LR image, \mathbf{n}_k is the observed noise in the k -th LR image. Let $S_{\mathbf{x}}, S_{\mathbf{y}}$ be two finite-dimensional real vector spaces with inner product $\langle \cdot, \cdot \rangle$, norm $\|\cdot\| := \langle \cdot, \cdot \rangle^{1/2}$, $\dim S_{\mathbf{x}} = N$ where N is the total number of pixels/voxels and $\dim S_{\mathbf{y}} = m = N \cdot d$ where $d = \{2, 3\}$ for 2D/3D images. Let HR images $\mathbf{X} \in S_{\mathbf{x}}$ and $\mathbf{DX} \in S_{\mathbf{y}}$ their gradients. The gradient operator $\mathbf{D} : S_{\mathbf{x}} \rightarrow S_{\mathbf{y}}$ is a continuous linear operator with norm $\|\mathbf{D}\| := \max\{\|\mathbf{DX}\| \mid \mathbf{X} \in S_{\mathbf{x}}, \|\mathbf{X}\| \leq 1\}$. Let $\frac{\partial}{\partial \mathbf{x}_i}$ denotes the derivative operator w.r.t. dimension \mathbf{x}_i .

1.3.2 A generic observation model

Given the literature, the most accepted image acquisition model in the context of fetal MRI is the linear model:

$$\mathbf{X}_{kl}^{LR} = \mathbf{H}_{kl}\mathbf{X} + \mathbf{n}_k, \tag{1.1}$$

where \mathbf{H}_{kl} are linear operators that supposedly model the acquisition distortions (such as noise, blurring, aliasing, intensity bias and motion). In this process, the MR scanner acquires several LR stacks of 2D slices, referred as LR images, which are downsampled, degraded, and aliased from the HR original scene (Figure 1.3). A typical acquisition model accounting for motion, blurring and downsampling processes has been considered in [6, 7, 10, 11, 14, 22, 23].

1.3. Overview of fetal MRI reconstruction algorithms

In those formulations, the matrix \mathbf{H}_{kl} is decomposed into three matrices accounting for motion \mathbf{M}_{kl} , blurring effects \mathbf{B}_{kl} , and a basic downsampling/aliasing operator \mathbf{A}_{kl} , i.e.:

$$\mathbf{H}_{kl} = \mathbf{A}_{kl}\mathbf{B}_{kl}\mathbf{M}_{kl}, \quad (1.2)$$

where \mathbf{B}_{kl} is the 3D Point-Spread-Function (PSF) of the system and \mathbf{M}_{kl} is assumed to be 6-DOF 3D rigid motion. Typically, a good approximation of the PSF is a 3D Gaussian function with the full width at half maximum (FWHM) equal to the slice-thickness in the slice-select direction and $1.2 \times$ voxel size in-plane [7, 13]. In [8, 9], the slice acquisition process is fully modeled by decomposing \mathbf{B}_{kl} into two matrices, that simulate (1) the in-plane 2D PSF (\mathbf{P}_{kl}) and (2) the slice profile (\mathbf{S}_{kl}):

$$\mathbf{H}_{kl} = \mathbf{A}_{kl}\mathbf{P}_{kl}\mathbf{S}_{kl}\mathbf{M}_{kl}, \quad (1.3)$$

where \mathbf{P}_{kl} is a 2D Gaussian function with FWHM equal to $1.2 \times$ voxel size in-plane, \mathbf{S}_{kl} corresponds to a 3D rotation operator that defines the orientation of the slice plane. In [13], the authors proposed to unify SR, regularization, robust statistics and intensity matching within a common expectation maximization framework. The model (1.1) is modified to consider intensity inhomogeneities (bias field and slice-dependent scaling factors) as follows:

$$\mathbf{X}_{kl}^{LR*} = \mathbf{H}_{kl}\mathbf{X} + \mathbf{n}_k, \quad \mathbf{X}_{kli}^{LR*} = s_{kl} \exp(-\mathbf{I}_{kli})\mathbf{X}_{kli}^{LR}, \quad (1.4)$$

where \mathbf{X}_{kl}^{LR*} represents the l -th scaled, denoised and bias-corrected slice of the k -th LR image, \mathbf{X}_{kli}^{LR*} is the intensity of the i -th voxel of \mathbf{X}_{kl}^{LR*} , \mathbf{X}_{kli}^{LR} is the intensity of the i -th voxel of the l -th slice of the k -th original LR image, s_{kl} is the corresponding intensity scaling factor, and \mathbf{I}_{kli} the corresponding bias field factor.

Finding the original HR image in (1.1) and (1.4) that generated the LR images \mathbf{X}^{LR} under the MRI acquisition is carried out with an inverse problem strategy, where (1.1) and (1.4) are known to be the forward models (Figure 1.3). This means that the given measures \mathbf{X}^{LR} are used to generate the original unknown HR image \mathbf{X} . The most natural way to combine the LR images is through a standard least-square problem:

$$\min_{\mathbf{X}} \sum_{kl} \|\mathbf{H}_{kl}\mathbf{X} - \mathbf{X}_{kl}^{LR}\|^2. \quad (1.5)$$

However, due to the presence of noise and insufficient number of acquired LR images, the above inverse problem is said to be ill-posed, meaning that it has generally no meaningful solutions. A natural solution of this issue is to add **priors** about \mathbf{X} , i.e. make use of known properties that \mathbf{X} holds such as intensity smoothness.

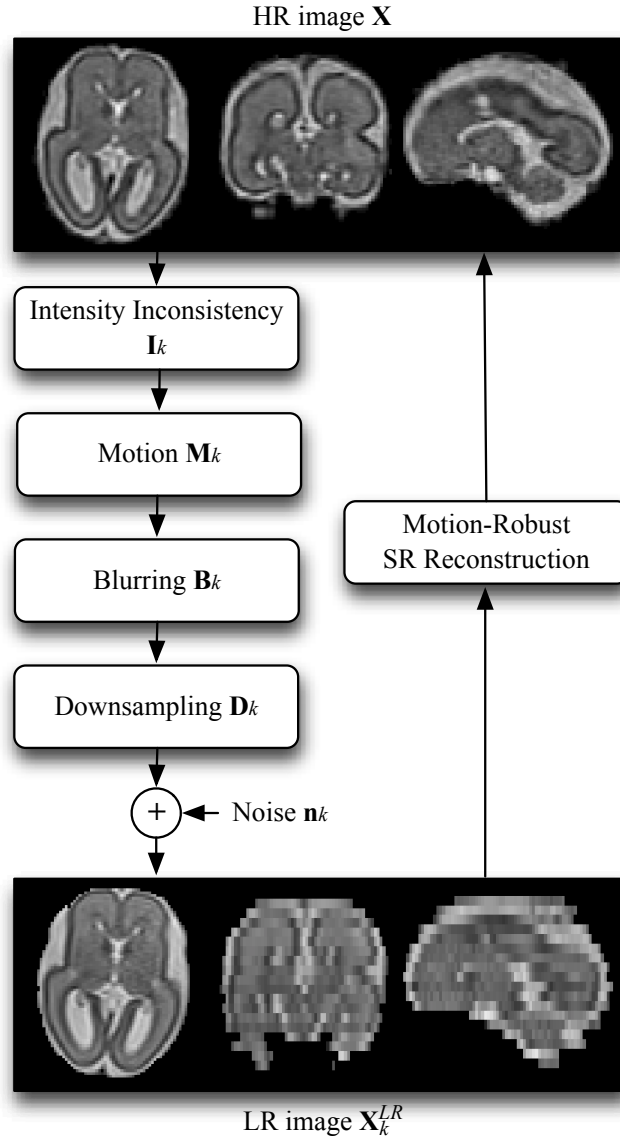


Figure 1.3 – The observation model of a real MR imaging system relating the low-resolution (LR) image \mathbf{X}_k^{LR} (observed images) to an high-resolution (HR) image \mathbf{X} . The SR reconstruction step corresponds to the inverse problem, i.e., finding \mathbf{X} given the observations \mathbf{X}_k^{LR} .

1.3.3 Two-step reconstruction algorithm

Let us now introduce the most generic algorithm for fetal brain MRI reconstruction [6–14]. The algorithm consists in iterating the following two steps until convergence:

Step 1: Motion estimation

$$\mathbf{M}_{kl}^{m+1} = \underset{\mathbf{M}_{kl}}{\operatorname{argmin}} \sum_{kl} \|\mathbf{A}_{kl} \mathbf{B}_{kl} \mathbf{M}_{kl} \mathbf{X}^m - \mathbf{X}_{kl}^{LR}\|_M, \quad (1.6)$$

where $\|\cdot\|_M$ is a distance function that can be based on l_2 -distance [8–10], cross-correlation [7], and NMI [6, 11–13].

Step 2: Image restoration

$$\mathbf{X}^{m+1} = \arg \min_{\mathbf{X}} \frac{\lambda}{2} \sum_{kl} \|\mathbf{A}_{kl} \mathbf{B}_{kl} \mathbf{M}_{kl}^{m+1} \mathbf{X} - \mathbf{X}_{kl}^{LR}\|^2 + R(\mathbf{X}),$$

where $R(\mathbf{X})$ is a prior introduced to regularize the solution, the first term relates to data fidelity. The parameter λ balances the trade-off between $R(\mathbf{X})$ and data fidelity. The general reconstruction scheme is illustrated in Figure 1.2. Our present work focuses on the image restoration step. It is beyond the scope of this paper to also tackle the motion compensation problem but we briefly summarize in the next section what the fetal MRI literature offered to solve this problem. We refer to [24] for a detailed discussion about motion correction strategies in fetal applications.

1.3.4 Motion estimation algorithms

The motion estimation problem is addressed through an image registration task that aims at compensating mainly for motion occurring between slices of the LR images, typically generated by short and fast movements of the fetal head. All existing methodologies [6–14] have addressed the problem using voxel-based registration methods where fetal motion is modeled as a full 6 degree-of-freedom rigid 3D transformation (3 translations and 3 rotations). Typically, they consist in (1) globally co-registering the LR images (volume-to-volume registration) and (2) hierarchically aligning every slice of the LR image to the reconstructed HR image (slice-to-volume registration), that is built using the current estimate of slice positions.

In practice, most registration methods differ only as regards their choice of similarity metric, the distance $\|\cdot\|_M$ in (1.6), and the corresponding optimization algorithm used to estimate the spatial transformation. When the assumptions of similar levels of blur and identical contrasts between LR volumes are made, the mean square intensity difference (MSD) is adopted [8, 9]. In order to force similar intensity values in the images being registered, a weighted MSD [10] and cross-correlation (CC) [7] measures have also been proposed. To not be based on strong assumptions between the two images and to be less sensitive to changes in overlap, the Normalized Mutual Information (NMI) as cost function has also been used [6, 11–13]. In all methods, a classical hierarchical strategy is applied in order to incorporate the interleaved aspect of acquisition and to reduce the risk to fall into local minima. Such hierarchical implementation involves decreasing step sizes of the optimization algorithm at the different stages of registration.

Rather than single slice-to-volume registration, the Slice Intersection Motion Correction (SIMC) [10] aims at solving a slice motion correction registration by seeking the collective alignment of all slices simultaneously, and considering the matching structure along all intersecting slice pairs.

Chapter 1. An Efficient TV Algorithm for Super-Resolution in Fetal Brain MRI with Adaptive Regularization

While all approaches deal with the motion compensation as an independent step, a unified formulation for motion estimation and SR reconstruction was recently presented in [14]. Their major contribution is a regularization term for the motion estimation that encodes the high correlation between temporal neighboring slices, increasing the robustness when large motion occur.

Despite these motion compensation efforts, the HR image may still be corrupted by remaining registration errors and other types of motion artifacts not well-modeled by a 6 DOF transformation². To treat these cases, outlier detection and rejection schemes are used, either implemented as a separate module preceding the SR [6, 10], or incorporated in the energy formulation of the restoration algorithm [9, 13].

1.3.5 Fetal MRI restoration algorithms

Original restoration algorithms were designed in the frequency domain, using the shifting and aliasing properties of the Fourier Transform in order to increase the image resolution. But these frequency approaches have shown to have an observation model limited to translation only. Nowadays, researchers in fetal MRI address this problem in the spatial domain, which allow models taking into rotation [25]. Besides, desired edge-preserving properties are easier to deal with in the spatial domain.

Interpolation models

Pioneer works on fetal HR restoration are based on the interpolation SR model [6, 7, 10, 22]. They consist in performing an iterative reconstruction procedure, interleaving rigid co-registration of the LR images and Scattered Data Interpolation (SDI) (interpolation onto an HR grid) steps.

Based on the acquisition model (1.2), the development of such approaches have been motivated by assuming that \mathbf{B}_{kl} is linearly spatial invariant and is the same for all slices and \mathbf{M}_{kl} considers only rigid 6 DOF motions (translations + rotations). Thus, \mathbf{B}_{kl} and \mathbf{M}_{kl} can commute in (1.2), and after injection in (1.1), the acquisition model becomes:

$$\mathbf{X}_{kl}^{LR} = \mathbf{A}_{kl} \mathbf{M}_{kl} \underbrace{\mathbf{B}_{kl} \mathbf{X} + \mathbf{n}_k}_{\mathbf{Z}} = \mathbf{A}_{kl} \mathbf{M}_{kl} \mathbf{Z}. \quad (1.7)$$

A composite image on non-uniformly spaced sampling points is first obtained with the registration of LR images. Then, nonuniform interpolation is performed to get \mathbf{Z} , an image with uniformly spaced sampling points.

The first interpolation method that tackles the SR problem in fetal MRI was presented in [6]. The method used an interpolation SR approach that comprises slice-to-volume registration

²For instance, when fetus is displaced from the region being imaged and, due to the loss of signal, LR images have dark slices.

1.3. Overview of fetal MRI reconstruction algorithms

interleaved with Scattered Data Interpolation (SDI). Once motion parameters are estimated, a bias field correction step is performed to correct the local relative intensity distortion between LR images. Finally, a computationally efficient local neighborhood Gaussian kernel SDI is employed for reconstruction but this reduces spatial frequency content and thus results in excessive blurring. In [7], SDI is improved with the use of cubic B-spline kernel SDI.

Introduction of spatial priors has been later adopted. They are reviewed in the next section.

Bayesian and Variational models

Two main categories of algorithms that introduce spatial regularizations in the restoration task can be distinguished: (1) Deterministic / variational models and (2) stochastic / Bayesian models. Typically, stochastic approaches rely on the formulation of the problem in a Bayesian framework such as *Maximum a Posteriori* (MAP), while deterministic approaches are based on the formulation of Constrained Least Squares (CLS) energy with functional space-based regularization. In both approaches, the HR image and motion among LR images can be considered as either stochastic or deterministic variables, relating the SR reconstruction steps stochastically or deterministically toward an optimal reconstruction.

Let us express the SR reconstruction problem into a full Bayesian formulation. Let $\mathbf{H}_{kl} = \mathbf{A}_{kl}\mathbf{B}_{kl}\mathbf{M}_{kl}$ be the matrix modeling the MRI acquisition. Let suppose \mathbf{n}_k to be Gaussian. Then, SR reconstruction can be formulated as:

$$\hat{\mathbf{X}} = \operatorname{argmax}_{\mathbf{X}} \prod_{kl} \Pr(\mathbf{X} | \mathbf{X}_{kl}^{LR}), \quad (1.8)$$

where $\Pr(\mathbf{X} | \mathbf{X}_{kl}^{LR})$ refers to the posterior probability. In fetal MRI, \mathbf{X} and \mathbf{H}_{kl} are assumed to be statistically independent and, if we suppose that \mathbf{H}_{kl} is estimated beforehand, denoted as $\hat{\mathbf{H}}_{kl}$, Eq. (1.8) can be reformulated (using the Bayes rule) as:

$$\hat{\mathbf{X}} = \operatorname{argmax}_{\mathbf{X}} \prod_{kl} \Pr(\mathbf{X}_{kl}^{LR} | \mathbf{X}, \hat{\mathbf{H}}_{kl}) \Pr(\mathbf{X}). \quad (1.9)$$

where probability $\Pr(\mathbf{X}_{kl}^{LR} | \mathbf{X}, \hat{\mathbf{H}}_{kl})$ corresponds to the data likelihood, $\Pr(\mathbf{X})$ is the prior probability on the HR image desired. Eq. (1.9) describes the popular stochastic MAP formulation of SR. When no prior distribution over the image is incorporated, the *Maximum Likelihood* (ML) formulation could be obtained from Eq. (1.9). Such ML formulation has been adopted in the pioneer work presented in [8, 9], which aims at providing an optimum solution through maximizing the conditional probability density function $\Pr(\mathbf{X}_{kl}^{LR} | \mathbf{X})$ of the acquired slice \mathbf{X}_{kl}^{LR} given the reconstructed volume \mathbf{X} . Standard stochastic optimization techniques, such as Monte Carlo [26, 27], Simulated annealing [28], Iterated Conditional Modes [29] or stochastic Partial Differential Equations [30] can be used to find a solution to (1.9). However, using the assumption of independent slice acquisition, the stochastic formulation (1.9) can be cast into a deterministic optimization framework. If we suppose that $\Pr(\mathbf{X}_{kl}^{LR} | \mathbf{X}, \hat{\mathbf{H}}_{kl}) = e^{-\lambda \|\hat{\mathbf{H}}_{kl}\mathbf{X} - \mathbf{X}_{kl}^{LR}\|^2}$, $\Pr(\mathbf{X}) = e^{-R(\mathbf{X})}$, when the noise residuals are presumed to be drawn from a Gaussian distribu-

Chapter 1. An Efficient TV Algorithm for Super-Resolution in Fetal Brain MRI with Adaptive Regularization

tion, and using the logarithmic function, then (1.9) becomes

$$\begin{aligned}
\hat{\mathbf{X}} &= -\log[\operatorname{argmax}_{\mathbf{X}} \prod_{kl} \Pr(\mathbf{X}_{kl}^{LR} | \mathbf{X}, \hat{\mathbf{H}}_{kl}) \Pr(\mathbf{X})] \\
&= \operatorname{argmin}_{\mathbf{X}} \sum_{kl} -\log[\Pr(\mathbf{X}_{kl}^{LR} | \mathbf{X}, \hat{\mathbf{H}}_{kl})] - \log[\Pr(\mathbf{X})] \\
&= \operatorname{argmin}_{\mathbf{X}} \lambda \sum_{kl} \|\mathbf{H}_{kl} \mathbf{X} - \mathbf{x}_{kl}^{LR}\|^2 + R(\mathbf{X}),
\end{aligned} \tag{1.10}$$

where $R(\mathbf{X})$ corresponds to the regularization term and λ controls the trade-off between regularization strength and data fidelity. As a result, it is equivalent to solve (1.9) and (1.10) under the slice independence hypothesis. Several proposed methods [8, 9, 11–14] used this equivalence to formulate the problem in a Bayesian framework and compute a solution with variational optimization techniques. However, non-Gaussian noise and outliers might be present in the data due to possible intensity inhomogeneities and inaccurate slice motion estimation. In this case, the ℓ_2 -norm is not robust and it has led to the development of modified versions of (1.10). They will be reviewed in the next section.

Variational terms

A more general formulation of (1.10) is:

$$\hat{\mathbf{X}} = \operatorname{argmin}_{\mathbf{X}} \lambda F(\mathbf{X}) + R(\mathbf{X}), \tag{1.11}$$

where $F(\mathbf{X})$ is a function that represents the data fidelity term. The choice of appropriate terms as well as an adequate optimization scheme is crucial for high reconstruction quality.

Data fidelity terms In fetal MRI acquisition, motion estimation errors and intensity inhomogeneities usually occur. This is critical as these errors influence the quality of the restored image. Consequently, several error norms for the data fidelity term have been considered for dealing with outliers.

As noise might not be Gaussian, they have considered in [8, 9] a modified error weight function Ω^k (based on the Huber error function) to take into consideration more generic outliers such that:

$$F(\mathbf{X}) = \|\Omega^k [\mathbf{H}_{kl} \mathbf{X} - \mathbf{x}_{kl}^{LR}]\|^2. \tag{1.12}$$

Such a formulation has shown to be a good balance between the most precise estimation in a Gaussian environment (ℓ_2 -norm) and the most robust estimation in a non-Gaussian environment.

Alternatively in [13], the authors proposed to simultaneously maximize the fit between the estimated reconstruction, the estimated intensity inhomogeneities and the data acquisition s.t. $\hat{\mathbf{X}} = \min_{\mathbf{X}} \min_{I_{kl}} F(\mathbf{X}, I_{kl})$, where I_{kl} is the underlying intensity inhomogeneity. They in-

1.3. Overview of fetal MRI reconstruction algorithms

roduced probability density function in order to model outliers, where they consider the inlier class posterior probability \mathbf{p}_{kl}^{slice} of the l -th slice of k -th LR image and the posterior probability \mathbf{p}_{klj}^{voxel} of a voxel j being classified as an inlier. This corresponds to an hybrid approach, where probabilities are integrated in a deterministic energy minimization problem as weight functions:

$$F(\mathbf{X}) = \sum_{klj} \mathbf{p}_{kl}^{slice} \mathbf{p}_{klj}^{voxel} \mathbf{e}_{klj}^2, \quad (1.13)$$

where $\mathbf{e}_{klj} = \mathbf{H}_{klj} \hat{\mathbf{X}}_j - \mathbf{X}_{klj}^{LR*}$ is the estimation error of the j -th voxel of the l -th slice of the k -th intensity-corrected LR image. It has been demonstrated that this method performs better than the method with Huber statistics and exclusion of either intensity matching or robust statistics results in drop of performance compared to their full method.

Finally, the authors in [14] suggested to reduce outliers by optimizing F with respect to both the underlying image \mathbf{X} and the underlying slice motions \mathbf{M}_{kl} . They also propose a unified formulation that simultaneously maximizes the fit between the estimated reconstruction, the estimated motion and the data acquisition data such that:

$$\hat{\mathbf{X}} = \underset{\mathbf{X}}{\operatorname{argmin}} \min_{\mathbf{M}_{kl}} F(\mathbf{X}, \mathbf{M}_{kl}). \quad (1.14)$$

This method has been compared against different formulations using different estimators and penalty terms for registration as well as different approaches such as the SIMC. On simulated data, the method designed with a ℓ_2 estimator and a Huber penalty has proved to provide the best overall performance.

Regularization terms Due to the ill-posedness of the restoration problem it is essential to introduce regularization terms to constraint the solution to hold prior knowledge of the desired image. If the regularization term is not appropriate, SR could result in too blurry images or artifacts can be produced. Several local regularization terms have been considered in the literature s.a. Tikhonov regularization [9, 14], Total-Variation based regularization [11, 13], and non-local regularization terms such as non-local means [12]. In general, TV energies can be seen as a measure of signal variability that penalizes only the total amount of gradient in the image, preserving edges during reconstruction, as opposed to Tikhonov which penalizes its distribution. For these reasons, they have been more widely adopted by the community.

Optimization via gradient descent

Let $F(\mathbf{X})$ be the simple l_2 error norm. The fetal brain reconstruction problem can be formulated as a first order convex optimization problem such that:

$$\min_{\mathbf{X} \in \mathcal{S}_x} \frac{\lambda}{2} \sum_{kl} \|\mathbf{H}_{kl} \mathbf{X} - \mathbf{X}_{kl}^{LR}\|^2 + \|\mathbf{X}\|_{TV} \text{ s.t. } \mathbf{X} \geq 0 \quad (1.15)$$

Chapter 1. An Efficient TV Algorithm for Super-Resolution in Fetal Brain MRI with Adaptive Regularization

where $\|\mathbf{X}\|_{TV} := \|\mathbf{DX}\|_1$ is the TV semi-norm [31]. Problem (1.15) is a convex but also non-smooth optimization problem. Non-smooth minimization has been challenging since the introduction of TV in imaging problems in the 90's. The most common methodology that optimizes TV consists in using a smooth ε -regularization of TV such that:

$$\|\mathbf{X}\|_{TV_\varepsilon} := \sum_{i,j} \sqrt{|\mathbf{DX}_{i,j}|^2 + \varepsilon} \rightarrow \|\mathbf{X}\|_{TV} \text{ for } \varepsilon \rightarrow 0. \quad (1.16)$$

The natural main motivation to introduce a quadratic approximation of TV is to apply smooth optimization tools like gradient descent or conjugate gradient schemes. In the context of fetal reconstruction, this approach was considered with $\varepsilon = 1$ in [11, 13] based on the edge-preserving technique introduced in [32]. In [9], the authors considered large ε that links to the Dirichlet/Laplacian energy, i.e. $\|\mathbf{X}\|_{TV_\varepsilon} \rightarrow \|\mathbf{X}\|_{Dir} = \|\mathbf{DX}\|^2$ for $\varepsilon \rightarrow \infty$. Standard optimization techniques for ε -TV have been carried out with the calculus of variation followed by a forward explicit steepest gradient descent scheme, such as in [11, 13], or followed by a quasi-Newton optimization scheme, such as in [14]. The non-local reconstruction approach suggested in [12], is solved by iteratively performing a basic image restoration algorithm, based on the Dirichlet energy, and a NLM denoising algorithm, as in [33]. The energy is optimized using the Fletcher-Reeves form of conjugate gradient descent algorithm.

TV energies have been largely adopted in the literature because of their powerful ability in edge preservation. However, only standard steepest gradient techniques have been applied to optimize fetal-based TV energies. But, such standard PDE-based optimization schemes may be slow because they are restricted by the Courant-Friedrichs-Lewy's condition [34], that basically sets an upper bound on the time step of the iterative flow s.t. $\Delta t \leq \varepsilon \Delta x / \max_{i,j} EL_{i,j}$, where EL corresponds to the Euler-Lagrange equations (speed of the flow) and Δx is the spatial step. It is known that the asymptotic rate of convergence of forward steepest descent techniques for smooth energy is $O(1/n)$ where n is the number of iteration steps and the iterative rate is $O(1/\varepsilon)$, see e.g. [35]. Besides the speed, there are two other limitations with ε -TV: (1) the TV term is not exactly solved because we compute an ε -solution, which does not preserve as well image contrasts and small-scale structures as the exact TV, and (2) there is an extra parameter, ε , to select (unlike exact TV).

1.4 Our Total Variation algorithm

1.4.1 Algorithm description

In the last years, fast TV-based algorithms based on convex optimization theory have been developed to solve sparse reconstruction problems such as Compressed Sensing. Major classes of TV optimization methods are (1) Alternating Direction Method of Multipliers (ADMM) [36, 37], (2) Forward-Backward algorithms [35, 38–40], and (3) Uzawa-based Primal-Dual

methods [41–43]. For the sake of clarity, we recall in this section our contribution [21] where we reformulated (1.15) by using an accelerated primal-dual hybrid gradient (PDHG) method based on [44] to design a fast, robust algorithm that offers accurate solutions and is guaranteed to converge to a global solution for Eq. (1.15) (i.e. solution is independent of the initialization). Specifically, PDHG consists in introducing the dual variable \mathbf{P} in Eq. (1.15) that splits our initial complex problem on the primal variable \mathbf{X} into two simpler problems easy to solve. It corresponds to rewrite Eq. (1.15) as the saddle point problem or equivalently as a primal-dual optimization problem:

$$\min_{\mathbf{X} \in S_X} \max_{\mathbf{P} \in S_Y} \underbrace{\langle \mathbf{D}\mathbf{X}, \mathbf{P} \rangle - F^*(\mathbf{P}) + G(\mathbf{X})}_{\|\mathbf{X}\|_{TV}} + \underbrace{\delta_C(\mathbf{X})}_{\mathbf{X} \geq 0} \quad (1.17)$$

where \mathbf{X} corresponds to the original primal variable and \mathbf{P} corresponds to the dual variable introduced, $G(\mathbf{X}) = \frac{\lambda}{2} \sum_{k=1}^K \|\mathbf{H}_k \mathbf{X} - \mathbf{X}_k^{LR}\|^2$, the convex function F^* denotes the barrier function of the ℓ_∞ unit ball, that is $F^*(\mathbf{P}) = 0$ if $|\mathbf{P}_i| \leq 1$ for $1 \leq i \leq n$, otherwise $F^*(\mathbf{P}) = +\infty$ and $\delta_C(\mathbf{X})$ is a barrier function of the convex set $C := \{\mathbf{X} \geq 0\}$. As G is uniformly convex, we may therefore apply [44] to solve Eq. (1.17). The proposed algorithm consists in iterating

$$\mathbf{P}^{n+1} = \text{prox}_{\sigma^n F^*}(\mathbf{P}^n + \sigma^n \mathbf{D}\bar{\mathbf{X}}^n) \quad (1.18)$$

$$\mathbf{X}^{n+1} = \text{prox}_{\tau^n G + \delta_C}(\mathbf{X}^n - \tau^n \mathbf{D}^t \mathbf{P}^{n+1}) \quad (1.19)$$

$$\begin{aligned} \theta^{n+1} &= 1/\sqrt{1+2\rho\tau^n}, \quad \tau^{n+1} = \theta^{n+1}\tau^n, \\ \sigma^{n+1} &= \sigma^n/\theta^{n+1} \end{aligned} \quad (1.20)$$

$$\bar{\mathbf{X}}^{n+1} = \mathbf{X}^{n+1} + \theta^{n+1}(\mathbf{X}^{n+1} - \mathbf{X}^n) \quad (1.21)$$

where prox_E the proximal operator of E defined as $\text{prox}_E(\mathbf{X}) := \text{argmin}_Y E(\mathbf{Y}) + \frac{1}{2}\|\mathbf{Y} - \mathbf{X}\|^2$. Solution of the inner problem Eq. (1.18) is given by $(\text{prox}_{\sigma^n F^*}(\mathbf{Z}))_i = \mathbf{Z}_i / \max\{1, |\mathbf{Z}_i|\}$ where $\mathbf{Z} = \mathbf{P}^n + \sigma^n \mathbf{D}\bar{\mathbf{X}}^n$. The solution of the least-square problem Eq. (1.19), $\min_{\mathbf{X} \geq 0} \frac{\lambda}{2} \sum_{k=1}^K \|\mathbf{H}_k \mathbf{X} - \mathbf{X}_k^{LR}\|^2 + \frac{1}{2\tau^n} \|\mathbf{X} - \mathbf{W}\|^2$ with $\mathbf{W} = \mathbf{X}^n - \tau^n \mathbf{D}^t \mathbf{P}^{n+1}$ can be computed with several approaches. We use a semi-implicit gradient descent scheme that provides fast good approximate minimizing solutions. More specifically, the Euler-Lagrange solution of Eq. (1.19) is $\lambda \tau^n (\mathbf{H}\mathbf{X} - \mathbf{X}^{LR}) + \mathbf{X} - \mathbf{W} = 0$ where $\mathbf{H} := \sum_{k=1}^K \mathbf{H}_k^t \mathbf{H}_k$ and $\mathbf{X}^{LR} := \sum_{k=1}^K \mathbf{H}_k^t \mathbf{X}_k^{LR}$ (note that \mathbf{H} and \mathbf{X}^{LR} are computed only once) and the iterative semi-implicit scheme is defined as $\mathbf{X}^{l+1} = \mathcal{P}_C(\mathbf{X}^l - \Delta t \lambda \tau^n (\mathbf{H}\mathbf{X}^l - \mathbf{X}^{LR}) + \Delta t \mathbf{W}) / (1 + \Delta t)$ where \mathcal{P}_C is the projection operator onto the set $\mathbf{X} \geq 0$ and $\Delta t = 0.1$ in all experiments.

Algorithm defined by Eq. (1.18)-(1.21) is guaranteed to converge to a saddle point $(\mathbf{X}^*, \mathbf{P}^*)$ to Eq. (1.17) (where \mathbf{P}^* is the maximizer of the dual problem and \mathbf{X}^* is the minimizer of the

Chapter 1. An Efficient TV Algorithm for Super-Resolution in Fetal Brain MRI with Adaptive Regularization

primal problem) and therefore a solution \mathbf{X}^* of the fetal reconstruction problem Eq. (1.15) as long as the initial time steps are chosen to be $\sigma^0 \tau^0 \leq 1/\|\mathbf{D}\|^2$, see [44] for more details.

We observe that TV-based models have been proposed in the literature for the fetal MRI reconstruction problems such as [11, 13, 32]. However, these works have considered a smooth approximation of the TV semi-norm, that is Eq. (1.16). Although our technique and the ones in [11, 13, 32] target at optimizing the TV energy, there is a subtle but essential difference between our approach and the other published TV-based techniques. If one wants the exact TV for best image edge recovery in ε -TV approaches, then taking ε as small as possible is required, but the smaller ε , the slower the convergence to the steady state solution (and $\varepsilon = 0$ can never be chosen). More importantly, our approach solves the *exact* TV with a new optimization scheme that is optimal for this class of problems as proved by Nesterov in [45], as the asymptotic speed of convergence of the algorithm is quadratic, i.e. $O(\frac{1}{n^2})$, while optimization techniques based on ε -TV are restricted to $O(\frac{1}{n})$. We will carry out a numerical experiment in Section 1.5.2 to validate these asymptotic speeds of convergence.

1.4.2 Adaptive regularization parameter λ

Determination of an appropriate weight λ that controls the strength of the regularization terms is the key for successful regularized image reconstruction. Intuitively, the amount of regularization would depend on the image resolution and the number of LR images. In this sense, the more the number of available LR images is increased, the less ill-posed the problem will be, and thus, a lower level of regularization will be required. To our knowledge, existing SR techniques in fetal MRI set the amount of regularization *arbitrarily* based on visual perception [8, 9, 11–14]. However, many regularization parameter choice methods have been proposed in image restoration and reconstruction problems [46, 47]. In general, they can be classified into two major categories. Methods in the first category s.a. those based the discrepancy principle [46, 47] seek to estimate the optimal value based on *a priori* knowledge of the image and/or statistics of the noise while methods in the second category s.a. those based on *L*-curve [48], generalized cross-validation (GCV) [49] and estimation of mean squared error (MSE) [50, 51] search to estimate the optimal value directly from the data available. We refer to [46, 47] for more details about regularization parameter choice.

In this section, we propose a first attempt for adaptive regularization parameter setting in fetal MRI SR reconstruction. Two data-driven strategies are presented here to perform a fair comparison between different regularization terms carried out in Section 2.5.

In fetal MRI, quantitative evaluation of the quality of the reconstruction is challenging as *a priori* knowledge about the ground-truth HR image is not known. To overcome this limitation, previous works on fetal brain SR reconstruction adopted two different approaches. On one side, the authors in [9, 11, 13] simulated fetal data from a known HR image to evaluate their algorithms under controlled conditions. On the other side, the authors in [13] suggested to evaluate their algorithms on clinical fetal data by performing a leave-one-out analysis.

For all experiments, a standard evaluation of the quality of the reconstructed images in fetal MRI was to use either the normalized root mean squared error (*NRMSE*) [8, 13, 21] or the peak signal-to-noise ratio (*PSNR*) [9, 11, 13], related through $PSNR = 10 * \log(1/NRMSE^2)$. Therefore, we have developed two strategies, as regards as the kind of experiments, where the PSNR is considered as the criterion for determining the optimal regularization weight, namely λ_{PSNR} , for comparison between different regularization terms.

For simulated experiments in Section 1.5.3, we propose a strategy which automatically sets the optimal value of the regularization parameter using *the ground-truth HR image* \mathbf{X}^{GT} . Specifically, for each regularization term, we select λ that provides the best reconstruction quality in terms of the highest PSNR with respect to \mathbf{X}^{GT} :

$$\lambda_{PSNR} = \arg \max_{\lambda} PSNR(\hat{\mathbf{X}}, \mathbf{X}^{GT}) \quad (1.22)$$

For in-vivo fetal experiments in Section 1.5.4, as we do *not* know the ground truth HR image, we propose a strategy which automatically sets the optimal regularization weight using *the set of available ground-truth LR images*. Specifically, for each patient and for each regularization term, we will select λ that provides the best reconstruction quality in terms of the highest mean PSNR over the set of acquired LR images:

$$\lambda_{PSNR} = \arg \max_{\lambda} \frac{1}{N} \sum_k PSNR(\hat{\mathbf{X}}_k^{LR}, \mathbf{X}_k^{LR}) \quad (1.23)$$

where $\hat{\mathbf{X}}_k^{LR} = \mathbf{H}\hat{\mathbf{X}}_k$ and $\hat{\mathbf{X}}_k$ corresponds to the HR image reconstructed in a leave-one-out fashion by excluding \mathbf{X}_k^{LR} from the reconstruction. For both strategies, an exhaustive search is performed. To validate the quality of the estimate, we present in Section 1.5.5 a perceptual evaluation of our adaptive regularization parameter in clinical practice using a multiple-alternative forced-choice approach, as in where a radiologist expert was required to choose one image as his preference from a set a reconstructed images with different levels of regularization in a range around λ_{PSNR} .

1.4.3 Practical implementation

Data preprocessing

A first manual reorientation step is performed with Slicer [52] (Step 1 in Figure 1.4). Then, we perform semi-manual brain masking (aided by region growing segmentation algorithm) to ensure good results of the subsequent image processing steps, as maternal tissue surrounding the brain may changes and could consequently corrupt them (Step 2 in Figure 1.4). Note that few works have addressed this problem automatically in the last past years, either

Chapter 1. An Efficient TV Algorithm for Super-Resolution in Fetal Brain MRI with Adaptive Regularization

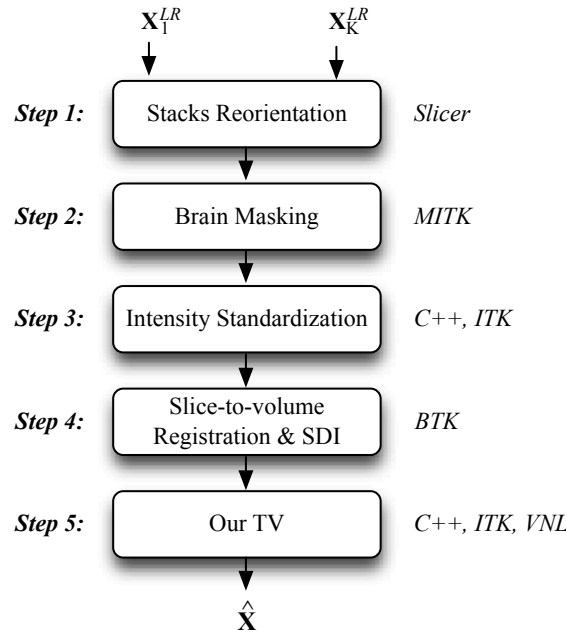


Figure 1.4 – Summary of the overall fetal brain HR reconstruction pipeline. Softwares, libraries and programming languages used are listed on the right-hand side in *italic*.

through template-based segmentation [53–55] or through machine learning [56, 57]. Finally, we standardize intensities of the LR stacks through $N4$ bias field correction, intensity scale standardization [58], and rescaling intensities into $[0, 255]$ (Step 3 in Figure 1.4).

Motion estimation

The estimation of motion parameters is done with BTK. Firstly, global stack registration is used for initialization of the transforms. Then, rigid 6 *degrees-of-freedom* slice-to-volume registration is performed where normalized correlation is used as metric for optimization. Prior to motion estimation, LR images are filtered by NLM denoising. This reduces the chance of the registration process to fall into local minimas. Finally, an initial HR image is estimated using SDI, as in [6]. It corresponds to Step 4 in Figure 1.4.

Super-resolution

Our Total Variation algorithm is implemented in C++ with Insight Toolkit [59]. A first step is the computation of matrices H_k in Eq. 1.15. It consists of positioning and orienting Gaussian kernels according to the transformation between each slice and the HR image followed by sampling to the grid of the HR image. Calculations and operations inherited from our TV formulation are implemented using the numerical library VNL for algebra purposes. Note that input LR images to the SR algorithm are not filtered by NLM denoising. In addition, we prefer to not update motion estimation during super-resolution. We know that motion estimation

updated during SR can further improve the quality of registration and consequently, the quality of image restoration. However, we noticed that the running time was dramatically increased. We decided to focus only on the optimization of the image restoration problem, which is the scope of this work. It corresponds to Step 5 in Figure 1.4.

1.5 Results and validation

As described in Section 1.3.5, most published works in the literature of fetal brain MRI have focused and stayed to these three most important regularizers, i.e. Tikhonov, TV and NLM. In our knowledge, evaluations between different ϵ -TV formulations have been performed by the authors in [11] showing that they led to similar results in terms of PSNR. However, there is no existing comparison either with a classical Tikhonov as used in the pioneer work [9], which is very fast to converge, or with NLM as provided by the open-source toolbox BTK [12] (considered as one of the *state-of-the-art* method freely available).

In this section, we present an extensive validation of our algorithm. First, the convergence speed of our optimization scheme is validated as regards ϵ -TV optimization scheme on a 2D brain image of a mature newborn (Section 1.5.2). Then, we carry out quantitative evaluations on 1) *simulated* fetal acquisitions from a newborn data and 2) normal and pathological fetal brain MRIs, where we compare our TV with Tikhonov and NLM. We study the robustness of the proposed TV reconstruction algorithm to different amounts of residual motion error (Section 1.5.3). We also evaluate the ability of our algorithm to be conformed with the MRI stacks acquired (Section 1.5.4). Eventually, we qualitatively evaluate the proposed algorithm on fetal MRIs (Section 1.5.5).

As BTK, the Tikhonov method is implemented in C++ with Insight Toolkit [59], where the Fletcher-Reeves version of the conjugate gradient is used for optimization. Projection onto the set $\{\mathbf{X} \geq 0\}$ is also applied to guarantee positive intensities. Global rigid stack registration is used for the newborn dataset (Section 1.5.3). Global rigid stack registration followed by slice-to-volume registration is employed in the case of the clinical datasets (Section 1.5.4). Tests are run on a 3.4 GHz Quad-core i7-3770 CPU. Reported running times correspond to the computational time of the SR problem optimization without motion estimation.

1.5.1 Material

Simulated fetal dataset We use a T2-weighted TurboFLASH image of a mature newborn to simulate fetal brain MRIs, as in [9, 13]. The image was acquired on a 3T Siemens Tim Trio with $TR = 4000ms$, $TE = 3.7ms$, slice thickness of $1.2mm$ and in-plane resolution of $0.78mm$. We consider the ground-truth image as the original image that was bias field corrected [60] and isotropically interpolated to a resolution of $1mm$ using B-splines. Six LR images, two per acquisition direction, with in-plane resolution of $1mm$, slice thickness of $3mm$, were simulated from the ground-truth image by applying downsampling and blurring operations.

Chapter 1. An Efficient TV Algorithm for Super-Resolution in Fetal Brain MRI with Adaptive Regularization

Shifts of 1mm were also introduced for images with the same acquisition direction. Note that a number of six LR images was adopted in compliance with previous works [11, 13] showing that the reconstruction quality marginally improves when more than 4-5 stacks LR images are used, in similar acquisition conditions.

Clinical fetal dataset Our clinical fetal dataset is formed by 53 LR images coming from the acquisition of 10 fetus, aged between 22 and 36 weeks GA (see Table 1.1). The acquisition of each fetus consists of a set of 4 to 8 stacks, where at least one stack is available in each anatomical direction. Stacks were acquired using two different MRI scanners, including 1) a 1.5T Siemens Aera using a T2-weighted HASTE sequence with a resolution of $1.13 \times 1.13 \times 3.6\text{mm}^3$ (TE/TR = 90/1200 ms), $1.13 \times 1.13 \times 4.8\text{mm}^3$ (TE/TR = 89/1000 ms) and 2) a 1.5T Philips with a resolution of $1.09 \times 1.09 \times 5.5\text{mm}^3$ (TE/TR = 180/7000 ms). Our dataset is thus heterogeneous as acquisitions come from fetus with different age, performed on different MRI scanner, and with different slice-thickness-to-in-plane-resolution ratio, also known as magnification factor (Mfactor). It was shown by the authors in [61] on 2D images that when Mfactor is an integer, the sufficient number of LR images is Mfactor². A similar number of required LR images was found in [11, 21] in the case of fetal 3D MRI.

This study has been approved by the Cantonal Research Ethics Committee of Vaud, Switzerland. The patient information from all data used in our study was anonymized and de-identified prior to our analysis.

1.5.2 Numerical comparison of optimization schemes: ε -TV v.s. exact TV

The goal of this section is to show that (i) for *small* ε (here we take $\varepsilon = 1e-4$), ε -TV produces the same quality for reconstructed SR images than exact TV but it requires more time to converge, and (ii) for *large* ε (here we take $\varepsilon = 1$), ε -TV does not produce good image quality as the TV approximation is too smooth to recover sharp image discontinuities, i.e. edges.

For (i), we carry out a standard numerical experiment on Figure 1.5 to validate the theoretical asymptotic rates of convergence for ε -TV with $\varepsilon = 1e-4$ (using an explicit forward gradient flow algorithm as in [11, 13]) and exact TV (using the proposed algorithm Eqs. (1.18)-(1.21) in Section 1.4). In order to speed up the computational time, we test both algorithms on a 2D HR image corresponding to an axial slice of the T2-weighted TurboFLASH image of the mature newborn (simulated fetal dataset). Four LR images were generated by applying subsampling operations and introducing noise but without adding any motion, see Figure 1.5a. The numerical asymptotic convergence rates are given in Figure 1.5b.

The computed slope of our optimization algorithm, -1.99 , is close to the theoretical one, i.e. -2 , and the slope of ε -TV, -0.82 , is also close to the theory, i.e. -1 . To illustrate the impact of the difference of convergence rates, we present Figures 1.5c and 1.5d. At the 20th iteration, we can see that the solution given by our algorithm, Figure 1.5d, is very close to the final steady state solution with a PSNR value of 25.21dB . However, the solution provided by the ε -TV

Table 1.1 – Clinical datasets.

Patient	GA	Diagnostic	Brain Volume	Sequence	Stacks	Resolution	Mfactor
P1	22w	Normal	112643mm ³	HASTE	6	1.13 × 1.13 × 3.6	3.2
P5	22w	Important malformation	118169mm ³	HASTE	4	1.13 × 1.13 × 3.6	3.2
P2	25w	Agenesis of the Corpus Colossum	204882mm ³	HASTE	6	1.13 × 1.13 × 3.6	3.2
P4	26w	Limited Gyration	290421mm ³	HASTE	4	1.13 × 1.13 × 3.6	3.2
P10	30w	Bilateral ventriculomegaly + kyste + hemorrhage	275914mm ³	SSFSE	4	1.09 × 1.09 × 5.5	5.1
P3	32w	Normal	470108mm ³	HASTE	5	1.13 × 1.13 × 4.8	4.3
P7	32w	Normal but small	324868mm ³	SSFSE	8	1.09 × 1.09 × 5.5	5.1
P8	33w	Asymmetrical ventriculomegaly	503682mm ³	SSFSE	7	1.09 × 1.09 × 5.5	5.1
P6	34w	Normal	344547mm ³	SSFSE	5	1.09 × 1.09 × 5.5	5.1
P9	36w	Bilateral ventriculomegaly + Cornes frontales	612998mm ³	SSFSE	4	1.09 × 1.09 × 5.5	5.1
Total					53		

algorithm, Figure 1.5c, is far away at the 20th iteration of its final solution as the PSNR value is 6.60dB. It illustrates the fact that more iterations are required for the ϵ -TV algorithm to converge. Eventually, at convergence, both solutions have the same reconstruction quality, around 25.21 – 25.23dB. This confirms that ϵ -TV for *small* ϵ offers same solution as exact TV, but at a higher computational cost.

For (ii), we present Figure 1.6 that compares ϵ -TV for *large* ϵ (Figure 1.6a), ϵ -TV for *small* ϵ (Figure 1.6b), and exact TV (Figure 1.6c). The solution provided by small ϵ and exact TV have almost the same PSNR value of 25.23dB, while the PSNR of large ϵ is lower at 20.34dB. A lower PSNR for large ϵ is expected as a smoother version of TV is less able to recover image edges.

Chapter 1. An Efficient TV Algorithm for Super-Resolution in Fetal Brain MRI with Adaptive Regularization

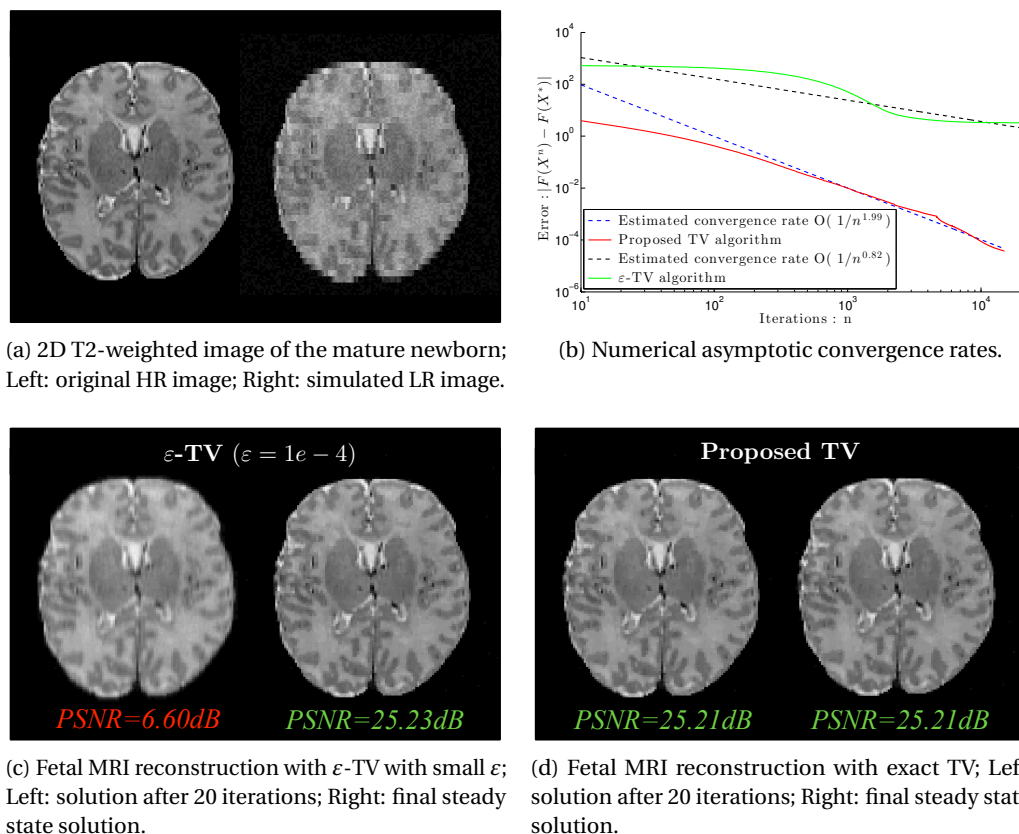


Figure 1.5 – Numerical comparison of optimization schemes: ε -TV vs exact TV.

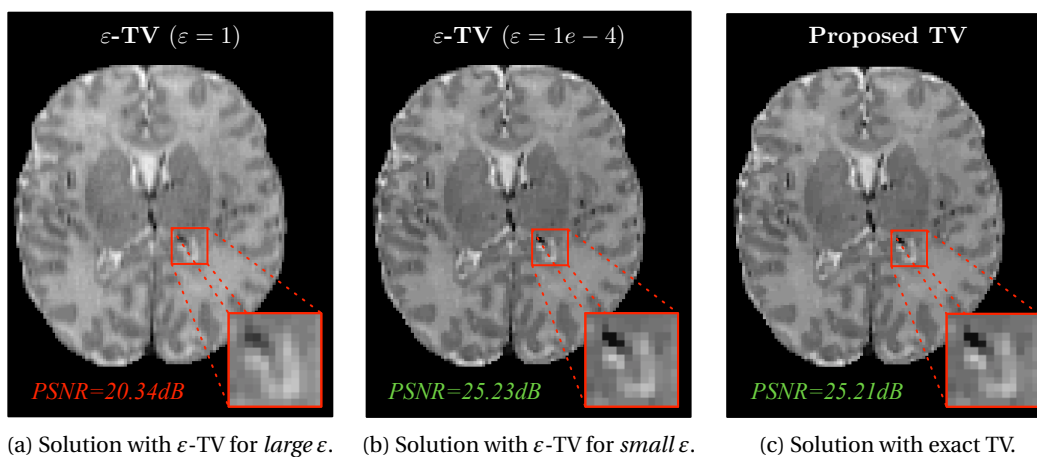


Figure 1.6 – Impact of the choice of ε in ε -TV algorithms.

1.5.3 Quantitative analysis of simulated fetal images

We assess the performance of our algorithm w.r.t. the residual motion error by randomly affecting 1/5, 2/5, 3/5 of the slices in each LR images. Different amounts of residual motion

errors are randomly added to one of the transform parameters (translation only and rotation only), following [6, 7, 9]. Translation errors are selected in $[-t, t]$ for $t = [0.1, 0.2, \dots, 1.5 \text{ mm}]$ and rotation errors are selected in $[-r, r]$ for $r = [0.1, 0.2, \dots, 2.0^\circ]$. The amount of the overall residual motion error is measured by computing the mean square error of the transform parameters. The reconstruction quality is evaluated with the Peak-Signal-To-Noise Ratio (PSNR). Parameters for Tikhonov, BTK and our algorithm are selected to have the best reconstructed HR image in the sense of the highest PSNR with respect to the original isotropic image of the newborn. Results are presented in Figure 1.7.

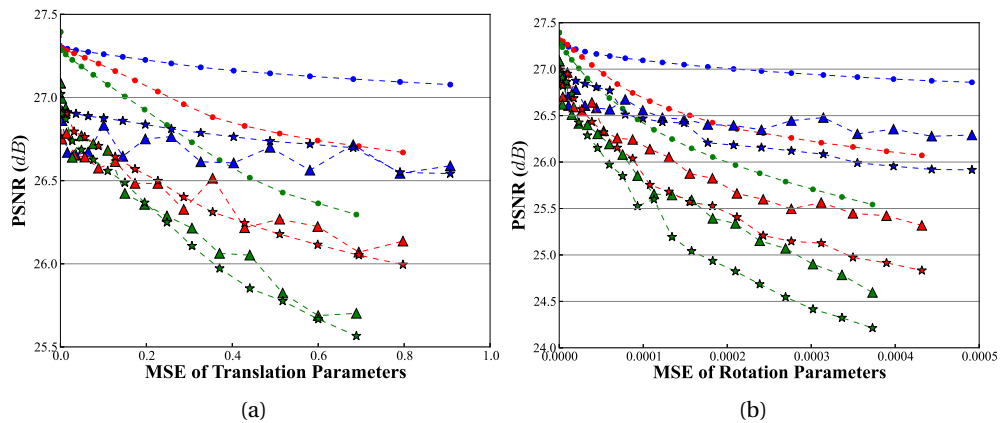


Figure 1.7 – Robustness of SR algorithms to motion error residuals when $1/5$, $2/5$, and $3/5$ of the slices are affected. \star denotes results obtained using the classical Tikhonov algorithm. \blacktriangle denotes results obtained using the BTK algorithm based on NLM. \bullet denotes results obtained using our TV algorithm.

We observe that the reconstruction quality always degrades independently of the regularization term as error motion residual is important. In addition, the TV regularization of our algorithm is less sensitive to residual errors of the motion estimation than the Tikhonov regularization and the NLM regularization employed in BTK. Finally, we observe that for similar MSE, the restoration quality of all methods decreases as the number of affected slices increases.

1.5.4 Quantitative analysis of real fetal images

We also assess the performance of our algorithm on clinical fetal brain MRI in terms of both fidelity with the original LR images and contrast in the reconstructed HR image. To do so, we perform a leave-one-out analysis, as in [13], that evaluates the ability of estimating the LR volume left out from the SR reconstruction based on all the other available LR volumes. We use the strategy described in Section 1.4.2 to automatically set, for each patient, an optimal regularization weight in terms of PSNR. Figure 1.8 illustrates the PSNR curves obtained for three different patients and for Tikhonov, BTK and TV. Obviously, λ is selected for each patient

Chapter 1. An Efficient TV Algorithm for Super-Resolution in Fetal Brain MRI with Adaptive Regularization

as the one providing the best reconstruction quality in terms of the highest mean PSNR (over the set of LR images). For adaptive regularization setting, exhaustive searches on the λ parameter are performed between the range of $[0.001, 0.002, \dots, 0.01, 0.02, \dots, 0.1, 0.2, \dots, 0.5]$ for TV and between the range of $[2/0.01, 2/0.02, \dots, 2/0.1, 2/0.2, \dots, 2/1.0, 2/2.0, \dots, 2/5.0]$ for BTK and Tikhonov.

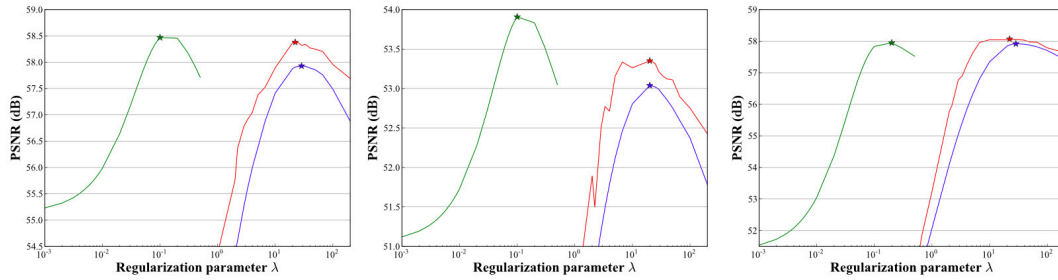


Figure 1.8 – Optimization of the regularization parameter λ for: a) patient P3 (5/18.5), b) patient P6 (5/26), and c) patient P7 (8/26). Numbers in parenthesis (X/Y) correspond respectively to the number X of stacks of slices and to the slice-thickness-to-in-plane-resolution ratio $Y=Mfactor^2$ (defined in Section 1.5.1). Both numbers indicates the “degree” of ill-posedness of the SR problem. \star denotes the optimal regularization weight for Tikhonov. \star denotes the optimal regularization weight for BTK. \star denotes the optimal regularization weight for our TV. The estimated optimal values are further used for the leave-one-out analysis presented in Table 1.2.

Once λ_{PSNR} is set, for each patient and each regularization term, we assess both quality and speed of reconstruction with a leave-one-out analysis. Qualitative results on one left-out ground-truth LR volume and its estimation by BTK and TV regularization are shown in Figure 1.9. Reconstruction results in terms of PSNR and running time are reported in Table 1.2.

Table 1.2 – Leave-one-out analysis: similarity w.r.t the original LR images.

Patient	PSNR (dB)			Run Time (s)		
	Tikhonov	BTK	Our TV	Tikhonov	BTK	Our TV
P1	53.64 ± 1.12	53.71 ± 1.29	53.85 ± 1.19	3.21 ± 3.89	10.76 ± 0.36	4.85 ± 0.06
P5	42.32 ± 2.45	43.44 ± 2.44	44.64 ± 2.52	4.17 ± 0.60	14.54 ± 0.60	4.66 ± 0.08
P2	48.31 ± 2.31	48.56 ± 2.44	48.90 ± 2.37	6.66 ± 2.82	21.52 ± 1.71	8.68 ± 0.11
P4	45.91 ± 3.21	46.38 ± 3.44	47.14 ± 3.50	12.14 ± 5.45	43.04 ± 5.04	15.08 ± 0.30
P10	53.35 ± 4.47	54.22 ± 4.46	54.84 ± 4.40	2.79 ± 0.48	36.53 ± 2.41	12.76 ± 0.16
P3	57.93 ± 1.11	58.39 ± 1.16	58.47 ± 1.18	4.31 ± 0.67	82.61 ± 6.80	30.21 ± 0.91
P7	57.91 ± 8.23	58.07 ± 8.30	57.94 ± 8.13	4.23 ± 0.62	52.56 ± 4.51	23.79 ± 0.39
P8	57.40 ± 3.06	57.72 ± 3.19	57.74 ± 3.06	4.92 ± 0.60	104.74 ± 5.45	39.05 ± 0.46
P6	53.04 ± 4.24	53.39 ± 4.15	53.91 ± 4.09	2.83 ± 0.40	44.99 ± 1.91	15.88 ± 0.17
P9	52.90 ± 1.49	54.52 ± 1.11	54.94 ± 1.00	4.09 ± 0.21	76.33 ± 9.40	7.91 ± 0.18

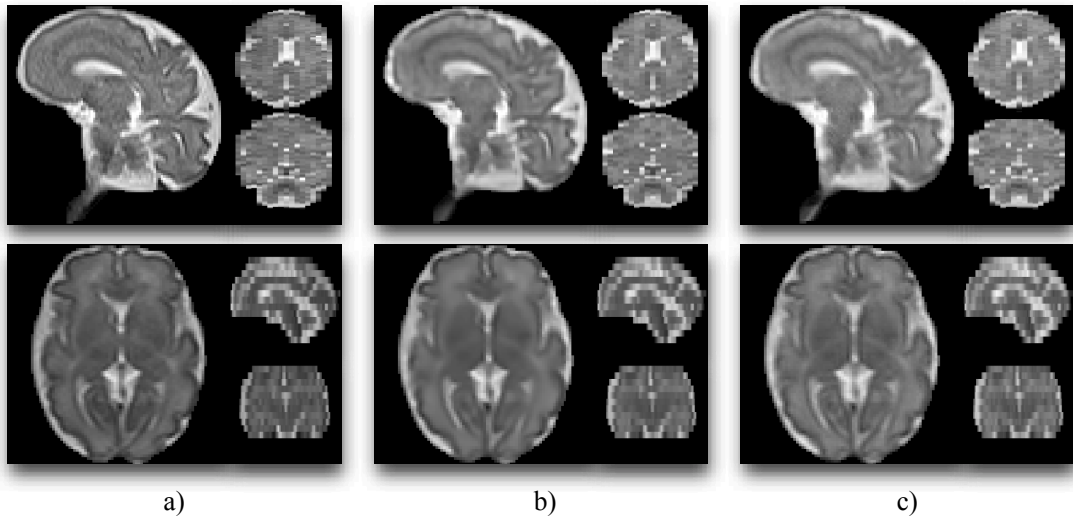


Figure 1.9 – Illustration of the leave-one-out analysis results for fetus P3 (row 1) and fetus P7 (row 2); a) Original LR Image \mathbf{X}_k^{LR} left for evaluation; b) $\hat{\mathbf{X}}_k^{LR}$ using BTK; c) $\hat{\mathbf{X}}_k^{LR}$ using our TV.

In terms of fidelity to the original LR stacks, both BTK and TV outperform Tikhonov and our TV algorithm performs better than BTK (0.34 dB in average for all subjects). In terms of speed, Tikhonov regularization is the fastest. TV regularization is about 4 times slower in average than Tikhonov (due to an extra inner problem optimisation), and TV is about 2-3 times faster than BTK. We also notice that BTK uses a parallel implementation of the non-local means algorithm, while the proposed TV algorithm has no such speed-up here. A parallel implementation of TV optimization may reduce the presented computational time.

It was observed that some reconstructed HR images suffer from reduced within-tissue contrast despite a high PSNR. Consequently, we decide to also measure the sharpness in the reconstructed HR image in complement to the PSNR. Sharpness validation was carried out using the energy of the gradient magnitude image (**M2**), as proposed in [8]. We computed **M2** by integrating the magnitude of the gradient of the HR reconstructed image at all voxels. The rationale behind this study is that sharper structures would be observed if the motion-corrected images are more accurately fused in the restoration process. Sharpness results are summarized in Table 1.3. In most of all the patients, the HR images reconstructed by our TV-based restoration algorithm obtained higher **M2** values. Supported by better PSNR, this suggests that our algorithm with TV regularization provides the best performance in terms of stronger contrasts between and within tissues.

1.5.5 Perceptual evaluation of the adaptive regularization

We show in this section the capability of our TV algorithm to restore HR images for diagnosis purposes in fetal MRI. In order to evaluate the optimality of the regularization weight λ_{PSNR} automatically set in terms of PSNR, see Section 1.4.2, we adopted a multiple-alternative

Chapter 1. An Efficient TV Algorithm for Super-Resolution in Fetal Brain MRI with Adaptive Regularization

Table 1.3 – Leave-one-out analysis: sharpness of the reconstructed HR images. $M2_{method}$ corresponds to the energy of the gradient magnitude image of the HR image reconstructed by the respective *method*.

Patient	$M2_{Tikhonov}$	$M2_{BTK}$	$M2_{TV}$
P1	1437602	1428423	1501358
P5	959734	963221	1327880
P2	1869633	1696500	2154680
P4	2234225	2277655	3040140
P10	4272910	4291232	4522360
P3	5918378	5791398	5840018
P7	3988919	4053390	4792452
P8	5785973	5441901.43	6407542
P6	4732112	5072980	4757786
P9	4233893	3988113	4247992

forced-choice approach, inspired from [62]. For each patient, a total of 6 HR images were reconstructed using a regularization weight of $\lambda_{PSNR}/8$, $\lambda_{PSNR}/4$, $\lambda_{PSNR}/2$, λ_{PSNR} , $2\lambda_{PSNR}$ and $4\lambda_{PSNR}$. Then, a radiologist expert proceeded to a visual evaluation where he indicated the best HR image in terms of image quality. Here, we consider only the reconstructed HR images of patients P1, P2, and P6 (diagnosed as normal brain), and the reconstructed HR images of patients P8 and P10 (diagnosed as abnormal brain) to minimize the number of images evaluated by the expert. Reconstruction results, running time for image restoration and the amount of regularization preferred by the expert are summarized in Figure 1.10. Results for only 3 patients are visually shown due to space limitation.

In general, HR reconstructed images with regularization weight of $\lambda_{PSNR}/4$ were selected for a majority of the patients (P1, P2, P8 and P10), except for patient P6, where an HR image with regularization of $\lambda_{PSNR}/2$ was chosen. This shows that the expert does prefer to visualize a little more regularized HR image than the one provided by the optimal PSNR (Section 1.5.4). Let us notice that our PSNR image quality measure may be not fully correlated with the visual image quality. Especially, outliers in the LR images are still used in the reconstruction process which might emphasize the noise in the reconstructed HR image. Let us now recall that our PSNR-based parameter choice method works (on a leave-one-out fashion) on LR images simulated from the reconstructed HR image to compute the PSNR w.r.t. the excluded LR image. This simulation process reduces the noise in the LR image simulated as regards the real noise observed in the original HR reconstructed image. Therefore when we say “a little more regularized image” we here talk regularization w.r.t. PSNR and not w.r.t. visual quality measure. So even if it is more regularized w.r.t. PSNR, the image may not be regularized w.r.t. visual quality.

This suggests that our method, originally proposed to automatically set the regularization level for a fair comparison between our TV, Tikhonov and BTK, could indeed give an upper bound for regularization setting in clinical practice. This also suggests that the integration of a

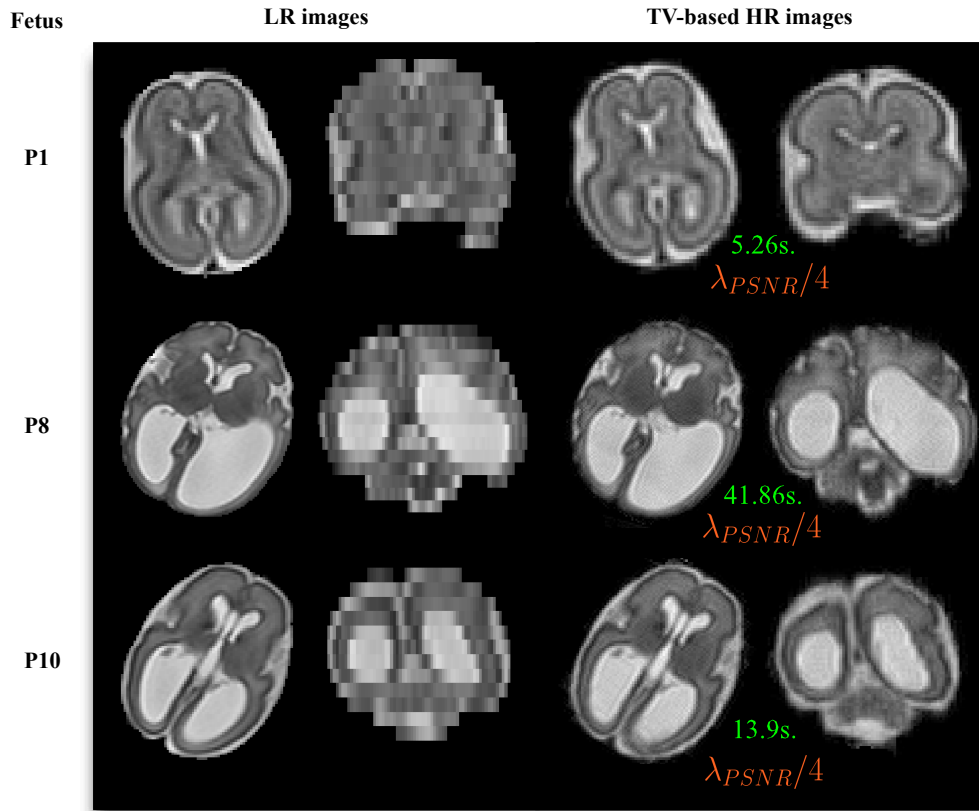


Figure 1.10 – Illustration of the qualitative analysis for fetus P1, P8 and P10.

robust outlier removal scheme could give even a more optimal estimate of the regularization visually perceived by the radiologist expert.

1.5.6 Discussion

In this chapter, we have revisited the existing SR techniques that address the fetal MRI brain reconstruction problem. Concretely, we have focused on the Bayesian and variational dual formulations with the goal of reviewing and unifying current state-of-the-art methods. Built on this formulation, we have recalled our TV-based optimization algorithm [21] and we have presented the design and the implementation of our reconstruction pipeline. We have also numerically recovered the theoretical speed of convergence of the proposed algorithm. Precisely, we have shown that the proposed algorithm solves the exact TV problem and outperforms the ε -TV optimization scheme in terms of convergence speed.

A second contribution is the extensive study of the convex TV regularization in comparison with classical Tikhonov and BTK. Concretely, we have presented for the first time a quantitative analysis of robustness of regularization w.r.t residual registration errors (see Section 1.5.3). Our experiments have clearly shown that TV is more robust to motion artifacts than Tikhonov

Chapter 1. An Efficient TV Algorithm for Super-Resolution in Fetal Brain MRI with Adaptive Regularization

and BTK. Moreover, this experiment confirms that registration accuracy is very crucial for the success of super-resolution algorithms. It also supports the development of outliers rejection schemes, as suggested in [9, 10, 13]. Obviously, our approach would perform even better with the inclusion of these schemes. Using the automated setting of λ for each patient independently and inspired by [13], we have performed a leave-one-out analysis to compare our TV regularization strategy to classical Tikhonov regularization and to NLM regularization on real fetal data (see Section 1.5.4). We have shown that TV outperforms Tikhonov and BTK. We have observed that such improvement is higher in the cases where less LR volumes are available and where the Mfactor is higher i.e. in the cases where the problem is more ill-posed. To validate this hypothesis we have conducted an experiment that analyzes, for a given subject, the behavior of the regularization in function of the number of LR volumes (3, 6 and 9) used in the reconstruction (see Fig. 1.11). This confirms that TV is more robust when only few LR volumes are available. Such results go in favor of our TV, since in a clinical acquisition setting we will often have few LR available (between 3 and 6).

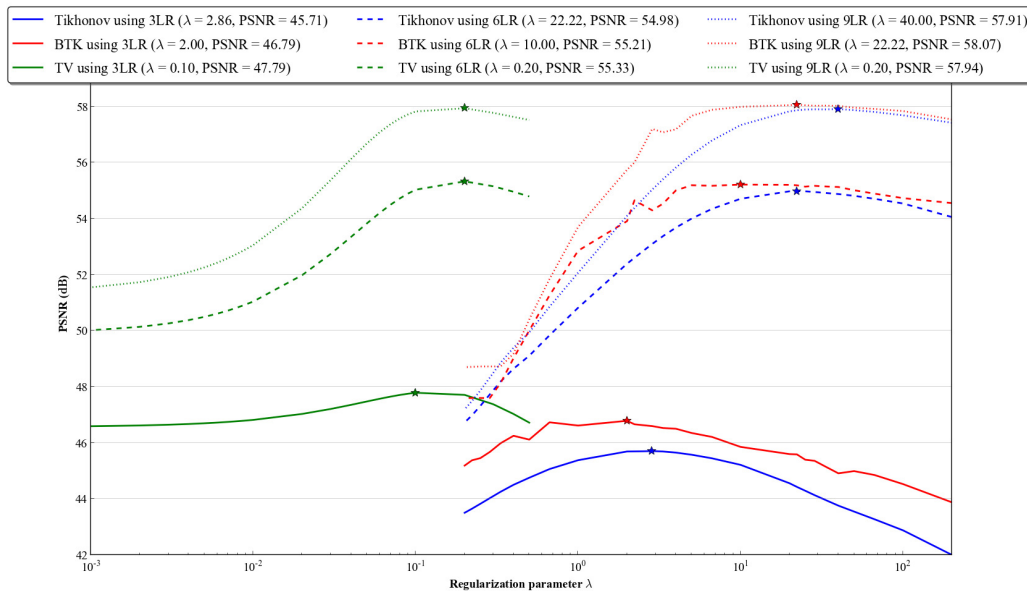


Figure 1.11 – Regularization versus number of input LR images.

A third contribution is the adaptive setting of the amount of regularization w.r.t. each subject to be reconstructed and thus adapted to the ill-posedness nature of the reconstruction problem. We propose a first attempt to automatically select the optimal λ w.r.t each subject and each algorithm in terms of PSNR (see Section 1.5.4). Note that only an exhaustive search on λ was performed here. This could be improved by the formulation of the problem in terms of quadratic energy minimization. This will allow a faster convergence towards to optimal value of λ and it will guarantee that the solution is optimal and unique. We could also suggest to integrate information about sharpness of the reconstructed HR image into the energy to be minimized. This should even better estimate the appropriate regularization for

diagnosis purposes. Moreover, we have adopted a simple heuristic approach as our goal was to fairly compare different regularization terms but the estimation of the optimal regularization weight could also be performed in a Bayesian framework, at the price of solving a non-convex optimization problem and computationally more expensive.

A last contribution is to show the capability of TV to reconstruct 3D volumes for diagnosis. We propose to proceed to a blind qualitative evaluation of the 3D reconstructed HR images conducted by an expert radiologist, including subjects diagnosed with both normal and abnormal brains (see Section 1.5.5). It has been shown that in general, his choice was 4 times smaller than the estimated λ , optimal w.r.t the PSNR. It demonstrates that the method, originally developed to determine the optimal regularization weight used by each algorithm with the leave-one-out analysis, is able to provide an upper bound to the regularization level in clinical application. In practice, we can imagine that this value could still be manually adjusted to fit end user expectations.

1.6 Conclusion

In summary, the proposed approach is a simple framework with an optimal and efficient TV optimization algorithm that has shown to be well adapted to solve the HR reconstruction problem in fetal MRI. It has been noticed that TV regularization generally outperforms Tikhonov and BTK in terms of reconstruction error w.r.t the original LR images and in terms of sharpness of the reconstructed HR images. However, more sophisticated schemes could be integrated into the framework, such as complete outlier rejection scheme and bias field correction scheme in order to enhance its robustness to several kinds of clinical scenarios.

Next chapter will present a novel slice-by-slice template-based method for automatic fetal brain localization and extraction, a crucial step of the reconstruction process, which is also the most-consuming step if performed manually or semi-automatically.

Acknowledgment

This work was supported by the Swiss National Science Foundation under Grant SNSF-141283 and by the CIBM of Geneva-Lausanne Universities and EPFL, as well as the Fondation Leenaards and Fondation Louis-Jeantet. The authors would like to thank Prof. Laurent Guibaud for providing access to the SSFSE data.

Bibliography

- [1] D. Prayer, *Fetal MRI*, Springer, 2011.
- [2] F. V. Coakley, O. A. Glenn, A. Qayyum, A. J. Barkovich, R. Goldstein, R. A. Filly, Fetal MRI: a developing technique for the developing patient, *American Journal of Roentgenology* 182 (1) (2004) 243–252.
- [3] P. Brugger, F. Stuhr, C. Lindner, D. Prayer, Methods of fetal MR: beyond T2-weighted imaging, *Eur Radiol* (57) (2006) 172–181.
- [4] C. Garel, New advances in fetal mr neuroimaging, *Pediatr Radiol* (36) (2006) 621–625.
- [5] D. Levine, H. Hatabu, J. Gaa, M. Atkinson, R. Edelman, Fetal anatomy revealed with fast mr sequences, *AJR* (167) (1996) 905–908.
- [6] F. Rousseau, O. A. Glenn, B. Iordanova, C. Rodriguez-Carranza, D. B. Vigneron, J. A. Barkovich, C. Studholme, Registration-based approach for reconstruction of high-resolution in utero fetal MR brain images, *Academic Radiology* 13 (9) (2006) 1072–1081.
- [7] S. Jiang, H. Xue, A. Glover, M. Rutherford, D. Rueckert, J. Hajnal, MRI of moving subjects using multislice snapshot images with volume reconstruction (SVR): Application to fetal, neonatal, and adult brain studies, *Medical Imaging, IEEE Transactions on* 26 (7) (2007) 967–980.
- [8] A. Gholipour, S. K. Warfield, Super-resolution reconstruction of fetal brain MRI, in: *MIC-CAI Workshop on Image Analysis for the Developing Brain (IADB'2009)*, 2009, pp. 45–52.
- [9] A. Gholipour, J. Estroff, S. Warfield, Robust super-resolution volume reconstruction from slice acquisitions: Application to fetal brain MRI, *Medical Imaging, IEEE Transactions on* 29 (10) (2010) 1739–1758.
- [10] K. Kim, P. Habas, F. Rousseau, O. Glenn, A. Barkovich, C. Studholme, Intersection based motion correction of multislice MRI for 3-D in utero fetal brain image formation, *Medical Imaging, IEEE Transactions on* 29 (1) (2010) 146–158.
- [11] F. Rousseau, K. Kim, C. Studholme, M. Koob, J. Dietemann, On super-resolution for fetal brain MRI, in: T. Jiang, N. Navab, J. Pluim, M. Viergever (Eds.), *Medical Image Computing and Computer Assisted Intervention (MICCAI)*, International Conference on, Vol. 6362 of *Lecture Notes in Computer Science*, Springer, 2010, pp. 355–362.
- [12] F. Rousseau, E. Oubel, J. Pontabry, M. Schweitzer, C. Studholme, M. Koob, J.-L. Dietemann, BTK: An open-source toolkit for fetal brain MR image processing, *Computer Methods and Programs in Biomedicine* 109 (1) (2013) 65–73.
- [13] M. Kuklisova-Murgasova, G. Quaghebeur, M. A. Rutherford, J. V. Hajnal, J. A. Schnabel, Reconstruction of fetal brain MRI with intensity matching and complete outlier removal, *Medical Image Analysis* 16 (8) (2012) 1550–1564.

Chapter 1. An Efficient TV Algorithm for Super-Resolution in Fetal Brain MRI with Adaptive Regularization

- [14] M. Fogtman, S. Seshamani, K. Kim, T. Chapman, C. Studholme, A unified approach for motion estimation and super resolution reconstruction from structural magnetic resonance imaging on moving objects, in: MICCAI workshop on Perinatal and Paediatric Imaging: PaPI, 2012, pp. 9–16.
- [15] A. Gholipour, J. A. Estroff, C. E. Barnewolt, S. A. Connolly, S. K. Warfield, Fetal brain volumetry through MRI volumetric reconstruction and segmentation, *International Journal of Computer Assisted Radiology and Surgery* 6 (3) (2011) 329–339.
- [16] J. Corbett-Detig, P. Habas, J. Scott, K. Kim, V. Rajagopalan, P. McQuillen, A. Barkovich, O. Glenn, C. Studholme, 3D global and regional patterns of human fetal subplate growth determined in utero, *Brain Structure and Function* 215 (2011) 255–263.
- [17] J. A. Scott, P. A. Habas, K. Kim, V. Rajagopalan, K. S. Hamzelou, J. M. Corbett-Detig, A. J. Barkovich, O. A. Glenn, C. Studholme, Growth trajectories of the human fetal brain tissues estimated from 3D reconstructed in utero MRI, *International Journal of Developmental Neuroscience* 29 (5) (2011) 529–536.
- [18] P. A. Habas, J. A. Scott, A. Roosta, V. Rajagopalan, K. Kim, F. Rousseau, A. J. Barkovich, O. A. Glenn, C. Studholme, Early folding patterns and asymmetries of the normal human brain detected from in utero MRI, *Cerebral Cortex* 22 (1) (2012) 13–25.
- [19] E. Van Reeth, I. W. K. Tham, C. H. Tan, C. L. Poh, Super-resolution in magnetic resonance imaging: A review, *Concepts in Magnetic Resonance Part A* 40A (6) (2012) 306–325.
- [20] E. Plenge, D. H. J. Poot, M. Bernsen, G. Kotek, G. Houston, P. Wielopolski, L. van der Weerd, W. J. Niessen, E. Meijering, Super-resolution methods in MRI: Can they improve the trade-off between resolution, signal-to-noise ratio, and acquisition time?, *Magnetic Resonance in Medicine* 68 (6) (2012) 1983–1993.
- [21] S. Tourbier, X. Bresson, P. Haggmann, J.-P. Thiran, R. Meuli, M. Bach Cuadra, Efficient total variation algorithm for fetal brain MRI reconstruction, in: P. Golland, N. Hata, C. Barillot, J. Hornegger, R. Howe (Eds.), *Medical Image Computing and Computer Assisted Intervention (MICCAI), International Conference on*, no. 8674 in *Lecture Notes in Computer Science*, Springer, 2014, pp. 252–259.
- [22] K. Kim, M. Hansen, P. Habas, F. Rousseau, O. Glenn, A. Barkovich, C. Studholme, Intersection based registration of slice stacks to form 3d images of the human fetal brain, in: *Biomedical Imaging: From Nano to Macro, 2008. ISBI 2008. 5th IEEE International Symposium on*, 2008, pp. 1167–1170.
- [23] F. Rousseau, A non-local approach for image super-resolution using intermodality priors, *Medical Image Analysis* 14 (4) (2010) 594–605.
- [24] C. Malamateniou, S. J. Malik, S. J. Counsell, J. M. Allsop, A. K. McGuinness, T. Hayat, K. Broadhouse, R. G. Nunes, A. M. Ederies, J. V. Hajnal, M. A. Rutherford, Motion-

- Compensation Techniques in Neonatal and Fetal MR Imaging., *AJNR American journal of neuroradiology*.
- [25] J. Yang, T. Huang, Image super-resolution: historical overview and future challenges, from the book: *Super-Resolution Imaging* (edited by Peyman Milanfar), CRC Press (Taylor & Francis Group), 2011.
- [26] N. Metropolis, A. W. Rosenbluth, M. N. Rosenbluth, A. H. Teller, E. Teller, Equation of state calculations by fast computing machines, *Journal of Chemical Physics* 21 (1953) 1087–1092.
- [27] W. Hastings, Monte carlo sampling methods using markov chains and their applications, *Biometrika* 57 (1970) 97–109. doi:10.1093/biomet/57.1.97.
- [28] S. Kirkpatrick, C. D. Gelatt, M. P. Vecchi, Optimization by simulated annealing, *Science* 220 (1983) 671–680.
- [29] J. Besag, On the statistical analysis of dirty pictures, *Journal of the Royal Statistical Society. Series B (Methodological)* 48 (3) (1986) 259–302.
- [30] N. Zabaras, *Solving Stochastic Inverse Problems: A Sparse Grid Collocation Approach*, John Wiley & Sons, Ltd, 2010, pp. 291–319.
- [31] L. I. Rudin, S. Osher, E. Fatemi, Nonlinear total variation based noise removal algorithms, *Physica D: Nonlinear Phenomena* 60 (14) (1992) 259 – 268.
- [32] P. Charbonnier, L. Blanc-féraud, G. Aubert, M. Barlaud, Deterministic edge-preserving regularization in computed imaging, *IEEE Trans. Image Processing* 6 (1997) 298–311.
- [33] J. Manjón, P. Coupé, A. Buades, V. Fonov, D. L. Collins, M. Robles, Non-local MRI upsampling, *Medical Image Analysis* 14 (6) (2010) 784 – 792.
- [34] R. Courant, K. Friedrichs, H. Lewy, On the partial difference equations of mathematical physics, *IBM J. Res. Dev.* 11 (2) (1967) 215–234.
- [35] A. Beck, M. Teboulle, A Fast Iterative Shrinkage-Thresholding Algorithm for Linear Inverse Problems, *SIAM J. Imaging Sci.* 2(1) (2009) 183–202.
- [36] R. Glowinski, P. L. Tallec, *Augmented Lagrangian and Operator-Splitting Methods in Nonlinear Mechanics*, SIAM, 1989.
- [37] T. Goldstein, S. Osher, The Split Bregman Method for L1-Regularized Problems, *SIAM Journal on Imaging Sciences* 2(2) (2009) 323–343.
- [38] Y. Nesterov, Smooth Minimization of Non-Smooth Functions, *Mathematic Programming* 103 (2005) 127–152.
- [39] P. Combettes, V. Wajs, Signal Recovery by Proximal Forward-Backward Splitting, *Multi-scale Modeling and Simulation* 4(4) (2006) 1168–1200.

Chapter 1. An Efficient TV Algorithm for Super-Resolution in Fetal Brain MRI with Adaptive Regularization

- [40] P. Combettes, J. Pesquet, Proximal Splitting Methods in Signal Processing, Fixed-Point Algorithms for Inverse Problems in Science and Engineering.
- [41] K. Arrow, L. Hurwicz, H. Uzawa, Studies in Linear and Non-Linear Programming, Stanford University Press.
- [42] M. Zhu, T. Chan, An Efficient Primal-Dual Hybrid Gradient Algorithm for Total Variation Image Restoration, UCLA CAM Report 08-34.
- [43] A. Chambolle, T. Pock, A First-Order Primal-Dual Algorithm for Convex Problems with Applications to Imaging, *Journal of Mathematical Imaging and Vision* 40(1) (2011) 120–145.
- [44] A. Chambolle, T. Pock, A First-Order Primal-Dual Algorithm for Convex Problems with Applications to Imaging, *JMIV* 40(1) (2011) 120–145.
- [45] Y. Nesterov, Smooth Minimization of Non-Smooth Functions, *Mathematic Programming* 103 (2005) 127–152.
- [46] N. Galatsanos, A. Katsaggelos, Methods for choosing the regularization parameter and estimating the noise variance in image restoration and their relation, *Image Processing, IEEE Transactions on* 1 (3) (1992) 322–336.
- [47] W. C. Karl, Regularization in image restoration and reconstruction, *Handbook of Image and Video Processing* 2nd Ed. (2005) 183–202.
- [48] P. Hansen, D. O’Leary, The use of the l-curve in the regularization of discrete ill-posed problems, *SIAM Journal on Scientific Computing* 14 (6) (1993) 1487–1503.
- [49] R. M. Mersereau, S. J. Reeves, Optimal estimation of the regularization parameter and stabilizing functional for regularized image restoration, *Optical Engineering* 29 (5) (1990) 446–454.
- [50] C. M. Stein, Estimation of the mean of a multivariate normal distribution, *Ann. Statist.* 9 (6) (1981) 1135–1151.
- [51] S. Ramani, Z. Liu, J. Rosen, J. Nielsen, J. Fessler, Regularization parameter selection for nonlinear iterative image restoration and MRI reconstruction using gcv and sure-based methods, *Image Processing, IEEE Transactions on* 21 (8) (2012) 3659–3672.
- [52] S. Pieper, M. Halle, R. Kikinis, 3D Slicer, *ISBI* (2004) 632–635.
- [53] J. Anquez, E. D. Angelini, I. Bloch, Automatic segmentation of head structures on fetal MRI., in: *Biomedical Imaging (ISBI), International Symposium on*, IEEE, 2009, pp. 109–112.
- [54] Y. Taleb, M. Schweitzer, C. Studholme, M. Koob, J.-L. Dietemann, F. Rousseau, Automatic template-based brain extraction in fetal MR images, in: *Organization for Human Brain Mapping (OHBM) conference.*, 2013.

- [55] S. Tourbier, X. Bresson, P. Hagmann, M. Cagneaux, M. Schaer, L. Guibaud, J.-P. Thiran, R. Meuli, M. B. Cuadra, Automated Brain Extraction in Fetal MRI by Multi-Atlas Fusion Strategy: Study on Healthy and Pathological Subjects., Joint Annual Meeting ISMRM-ESMRMB, 2014.
- [56] M. Ison, E. Dittrich, R. e. Donner, G. Kasprian, D. Prayer, G. Langs, Fully automated brain extraction and orientation in raw fetal MRI, MICCAI workshop on Perinatal and Paediatric Imaging: PaPI (2012) 17–24.
- [57] K. Keraudren, M. Kuklisova-Murgasova, V. Kyriakopoulou, C. Malamateniou, M. Rutherford, B. Kainz, J. Hajnal, D. Rueckert, Automated fetal brain segmentation from 2D MRI slices for motion correction, *NeuroImage* 101 (2014) 633–643.
- [58] L. G. Nyúl, J. K. Udupa, X. Zhang, New variants of a method of MRI scale standardization, *Medical Imaging, IEEE Transactions on* 19 (2) (2000) 143–150.
- [59] T.S. Yoo and M. J. Ackerman and W. E. Lorensen and W. Schroeder and V. Chalana and S. Aylward and D. Metaxas and R. Whitaker, ITK - The Insight Toolkit, in: *Medicine Meets Virtual Reality, 2002*, pp. 586–592.
- [60] N. J. Tustison, B. B. Avants, P. A. Cook, Y. Zheng, A. Egan, P. A. Yushkevich, J. C. Gee, N4ITK: improved N3 bias correction, *Medical Imaging, IEEE Transactions on* 29 (6) (2010) 1310–20.
- [61] Z. Lin, H.-Y. Shum, Fundamental limits of reconstruction-based superresolution algorithms under local translation, *IEEE Transactions on Pattern Analysis and Machine Intelligence*.
- [62] S. Reeves, A. Higdon, Perceptual evaluation of the mean-square error choice of regularization parameter, *Image Processing, IEEE Transactions on* 4 (1) (1995) 107–110.

2

Automated Template-based Brain Localization and Extraction for Fetal Brain MRI Reconstruction

A 10-page conference paper of the work in this chapter was peer-reviewed and presented as a poster presentation at the IntellMR workshop of the International Conference on Medical Image Computing and Computer-Assisted Intervention (MICCAI) 2015 as S. Tourbier, V. Taimouri, C. Velasco-Annis, R. Meuli, S. W. Warfield, A. Gholipour and M. Bach Cuadra, **“Fully Automated Fetal Brain MRI Reconstruction”**. The dataset used in this chapter was currently being extended at the time this thesis was written to be submitted to the Journal NeuroImage as S. Tourbier, V. Taimouri, C. Velasco-Annis, R. Meuli, S. W. Warfield, A. Gholipour and M. Bach Cuadra, **“Automated Template-based Brain Localization and Extraction for Fetal Brain MRI Reconstruction”**. A first preliminary work on automatic brain extraction was presented as electronic poster at the annual 2014 meeting of the International Society for Magnetic Resonance in Medicine (ISMRM) as S. Tourbier, X. Bresson, P. Hagmann, M. Cagneaux, M. Schaer, L. Guibaud, J.-P. Thiran, R.Meuli, M. B. Cuadra, **“Automated Brain Extraction in Fetal MRI by Multi-Atlas Fusion Strategy: Study on Healthy and Pathological Subjects.”** A second preliminary work as been peer-reviewed, presented as oral presentation, and published in the proceedings of the SPIE Medical Imaging Conference as S. Tourbier, P. Hagmann, M. Cagneaux, L. Guibaud, S. Gorthi, M. Schaer, J.-P. Thiran, R.Meuli, M. B. Cuadra, **“Automatic brain extraction in fetal MRI using multi-atlas-based segmentation”**, in: *Proc. SPIE Medical Imaging*, Vol. 9413, 2015, pp. 94130Y–94130Y–7.

2.1 Introduction

Fetal MRI has attracted a lot of attention and is being incrementally used as a complementary diagnostic tool to prenatal ultrasound imaging as it provides a better soft tissue contrast. Fast

Chapter 2. Automated Template-based Brain Localization and Extraction for Fetal Brain MRI Reconstruction

single shot multi-slice MRI sequences are used to freeze maternal and fetal motion; but the acquisition of thick slices (about 2 to 4mm) is necessary to obtain acceptable Signal-to-Noise Ratio (SNR) given the short acquisition time used to avoid motion at each slice acquisition. Thick slices and inter-slice motion artifacts limit the accuracy of volumetric analysis for clinical diagnosis and neuroscience studies [1].

In the last years, interest in finding a high-resolution (HR) volumetric image given a set of low-resolution slices with inter-slice motion artifacts has grown considerably. In [2, 3], the first reconstruction techniques based on slice-to-volume registration and scattered data interpolation were introduced. Later, super-resolution (SR) techniques [4–10] have boosted the quality of the reconstructed image by modelling an inverse problem for fetal image reconstruction. By providing finer details of the fetal brain, such techniques have enabled the neuroscience community to perform new research on early human brain development [11–18].

The fetal MRI reconstruction pipeline consists of various image processing steps (intensity standardization, motion estimation, and SR reconstruction). In general, algorithms [2–10, 19] rely only on brain tissue-relevant voxels of low-resolution (LR) images to warrant the assumption of motion rigidity used in rigid motion correction. This is a crucial step of the reconstruction algorithms. Consequently, the fetal brain (or brain region) needs to be localized and extracted prior to motion estimation and SR reconstruction.

Fetal brain localization and extraction is typically done manually or semi-automatically, thus corresponds to the most time-consuming, non-automatic step of the entire pipeline. It is therefore not a realistic solution for large-scale studies. In the literature, even though accurate brain extraction tools have been developed for adult and infant brain MRI [20, 21], those tools are not readily applicable to fetal MRI. Fetal brain MRI differs in many ways from neonatal or adult brain MRI in terms of image content (with maternal tissues surrounding the fetal brain), image contrast, brain size, and especially the arbitrary (non-standard) fetal position and orientation which also changes due to motion. Recent studies have addressed this problem in fetal MRI by adopting either template-based segmentation [18, 22–25] or machine learning [26–29] techniques.

2.2 Contributions

In this work, we propose to automatize fetal brain localization and extraction using a template-based approach, and integrate it with SR reconstruction. Specifically, our contributions are:

- An automated *slice-by-slice* brain extraction method in every stack of thick slices (LR image). It couples an accelerated template-to-slice block matching method for automatic brain localization with a novel deformable slice-to-template brain extraction method.
- The combination of the masking process with intensity standardization, motion correction, and super-resolution reconstruction: In our proposed approach the brain masks

2.3. Overview of fetal brain localization and extraction

are refined in the spatial space of the template using a consensus fusion voting process and are re-applied to the LR images as the reconstruction proceeds.

- An extensive validation on clinical data including healthy and pathological cases where:
 - we evaluate the brain extraction performance in terms of overlap measures with manual delineations,
 - we study for the first time the impact of automatic brain extraction performance on the final reconstruction quality,
 - we conduct a perceptual evaluation by expert observers to compare the quality of the final reconstruction using brain masks obtained manually and automatically with the proposed technique, and
 - we investigate the potential of the brain mask refinement method to provide an estimate of the intra-cranial fetal brain volume in the HR reconstructed images.

The chapter is organized as follows. Section 2.4 presents the proposed template-based approach. Section 2.5 develops an extensive validation of the proposed method in terms of brain extraction performance as well as the impact on reconstruction quality and brain volumetry, and Section 2.6 involves the discussion and conclusions.

2.3 Overview of fetal brain localization and extraction

Several, relatively recent, studies have addressed the automatic localization and extraction of fetal brain in MRI through either template-based segmentation [18, 22–25] or machine learning [26–29] techniques. The first attempt [22] of fetal brain extraction proposed to estimate the location of the eyes (based on rigid template registration) in order to segment the fetal brain using contrast, morphological and biometrical prior information. This method gave precise results in 22 out of 24 MRI stacks of fetuses aged between 30 and 35 gestational weeks; however, they relied on the assumption of minor motion between slices, which limits the robustness of the method to clinical databases where moderate to large motion can occur. More recently, a supervised approach [26], based on a two-phase random forest classifier, was adopted in order to obtain a method applicable to all fetal ages and more robust with respect to motion between slices. This method has shown comparable results to the method in [22] but the whole brain was contained inside the final bounding box in only 28% (coronal) to 58% (transversal, sagittal) of the cases. Later, localization accuracy of the brain was drastically improved by combining prior knowledge of the fetal head size with maximally stable extremal regions detection, bundled Scale-Invariant Feature Transform (SIFT) features and a bag-of-words model: the whole brain was contained inside the final bounding box in 85% of the cases [27]. The method, limited to the localization of the fetal brain (bounding box), was recently further improved with the use of spherical Gabor descriptors and 2D level-sets to provide an accurate final segmentation of the fetal brain with a Dice overlap metric above 90% [28].

Chapter 2. Automated Template-based Brain Localization and Extraction for Fetal Brain MRI Reconstruction

More recently, those techniques have been integrated in the reconstruction pipeline. Multi-atlas based brain extraction has been combined with motion correction and SR reconstruction in [24]. However, brain localization was done manually by reorienting and cropping the LR images as a first step. Such manual interventions prevent an automatic reconstruction and processing pipeline. The authors in [29] have proposed to localize the fetal brain using a Bag-of-Words model using SIFT features plus the RANdom SAmple Consensus (RANSAC) method for robust fitting and to provide a segmentation of the brain using a combination of a random forest classifier and a 3D conditional Random Field. Brain extraction is then refined as the reconstruction progresses, generating a final segmentation of the reconstructed fetal brain with a mean Dice value of 93%. In contrast to the works in [24, 29], motion correction and reconstruction uses a bounding box around the fetal brain and brain extraction is only applied afterward. Nevertheless, maternal tissues may mislead the registration, which may limit the success of reconstruction.

While prior knowledge is learnt and used as features and scales based on gestational age in previous works [28, 29], we propose in this work to use age matched templates [30] as priors to automatize brain localization and extraction in the fetal brain MRI reconstruction pipeline. Our approach only requires approximate gestational age of the query subject and does not need to be retrained to be used in cases with abnormal brains. It localizes the brain in each slice and extracts it using a template-to-slice block matching approach and using label propagation through deformable registration, therefore effectively estimates a brain mask through the reconstruction process. We combine brain localization and extraction with intensity standardization, motion estimation, and SR reconstruction. The integration of this approach into the reconstruction pipeline improves image reconstruction.

2.4 Novel template-based brain localization and extraction for fetal MRI

The whole reconstruction pipeline is illustrated by Figure 2.1. Firstly, brain localization is performed in each of the original acquired stacks (Box I in Figure 2.1) using the technique described in Section 2.4.1. It generates an initial alignment of the stack and position of the brain that crops and reorients the image to the template space. Secondly, all stacks are automatically masked using the proposed brain extraction method (Box II in Figure 2.1 and Section 2.4.2) and stack intensities are made consistent through intensity standardization as described in Section 2.4.3. Thirdly, 6-*degrees-of-freedom* (DOF) rigid slice-to-volume registration is performed for motion estimation where the *NCC* (normalized cross correlation) is used as the optimization metric. This step includes firstly global stack registration to initialize the transformations followed by 6-DOF rigid slice-to-volume registration. To reduce the chance of the registration process to fall into local minima, LR images are first denoised. Once motion parameters of all slices are estimated, we refine the brain mask in the thick slices. Intensity standardization (Box III in Figure 2.1) and brain mask refinement (Box V in Figure 2.1) are repeated at each iteration of slice-to-volume registration for motion estimation (Box IV in

2.4. Novel template-based brain localization and extraction for fetal MRI

Figure 2.1). Finally, an HR image is reconstructed by solving the super-resolution inverse problem (Box VI in Figure 2.1) that follows the Total-Variation (TV) regularized SR algorithm developed in [8, 10]. All the code was implemented in C++ with Insight Toolkit [31] and Python.

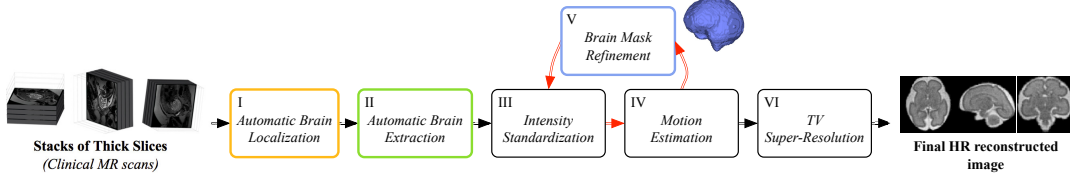


Figure 2.1 – Automated pipeline for fetal MRI reconstruction. The brain masks are progressively refined using the updated motion parameters.

2.4.1 Template-to-slice block matching brain localization

We aim to localize the brain in every stack of slices based on the technique preliminary presented in [25] where robustness to outlier slices has been improved. In contrast to the approach presented in [29], we use an age-matched template [30] as prior and match it directly to each slice through an accelerated block matching approach. The main benefit of this approach is not only it can retrieve the location of the brain in the image but it can also retrieve its global alignment in 3D. The localization problem is formulated as a block matching algorithm in which the similarity between each block, i.e. a whole 2D slice, extracted from the template and a query image (a fetal MRI slice) is maximized. However, the search space is large and the problem is computationally heavy as we do not know *a priori* the position of the fetal head. We decide to limit the search space by breaking the transformation model to rotation (θ) and translation (\mathbf{T}) parts for which parameters are estimated separately. We estimate the translation parameters for each rotation angle through the proposed block matching technique. The algorithm involves three steps: 1) block extraction and dimension reduction, 2) block matching using expectation maximization (EM), and 3) calculation of final transform by maximizing similarity.

Block extraction and dimension reduction A similarity matrix \mathbf{SM} is generated by computing the Sum of Square Distances (SSD) between a 2D block i in a template image and a 2D block j in the query image. \mathbf{SM}_{ij} is defined as:

$$\mathbf{SM}_{ij} = \frac{e^{-\text{SSD}_{ij}}}{\sum_k e^{-\text{SSD}_{ik}}} \quad (2.1)$$

Since SSD is not rotation invariant, the template image needs to be initially rotated using a rotation matrix (θ). Two-dimensional blocks are then extracted from the template and the similarity matrix \mathbf{SM}^θ is computed for each rotation matrix. In addition, computation of \mathbf{SM}^θ is accelerated by projection of each block to a lower dimensional space through a random

Chapter 2. Automated Template-based Brain Localization and Extraction for Fetal Brain MRI Reconstruction

matrix based on Johnson-Lindenstrauss Lemma [32].

Expectation maximization for match detection Let \mathbf{R} be the template image, \mathbf{S} be the query image, and \mathbf{M} be a binary matrix representing the match between blocks in the two images [33], thus $\mathbf{E}_{\mathbf{M}}[\mathbf{M}_{ij}] = P(\mathbf{M}_{ij} = 1)$. Matches between blocks and the translation are then iteratively updated within an EM framework. The expectation step corresponds to calculating

$$\mathbf{E}_{\mathbf{M}}[\mathbf{M}_{ij} | \mathbf{R}, \mathbf{S}, \mathbf{T}^\theta] = P(\mathbf{M}_{ij} = 1 | \mathbf{R}, \mathbf{S}, \mathbf{T}^\theta), \quad (2.2)$$

where \mathbf{T}^θ is the translation transferring the template to the fetal brain in the image after initial rotation θ . Then, the translation \mathbf{T} is initially set to zero, and iteratively updated to maximize the probability of the block r_i in \mathbf{R} being matched to the blocks s_j in \mathbf{S}

$$\arg \max_{\mathbf{T}^\theta} \mathbf{E}_{\mathbf{M}}[\log(P(\mathbf{R}, \mathbf{M} | \mathbf{S}, \mathbf{T}^\theta))] = \quad (2.3)$$

$$\arg \min_{\mathbf{T}^\theta} \sum_{ij} P(\mathbf{M}_{ij} = 1 | \mathbf{R}, \mathbf{S}, \mathbf{T}^\theta) \|\mathbf{T}^\theta \circ r_i - s_j\|_p. \quad (2.4)$$

where $\|\cdot\|_p$ is the L_p norm. If $P(s_j | r_i, \mathbf{T}^\theta)$ follows a normal Gaussian distribution, the optimal solution of Eq. (2.4) is obtained by $p = 2$, i.e. by least squares optimization. Nonetheless, because of outliers $P(s_j | r_i, \mathbf{T}^\theta)$ does not follow a Gaussian distribution. Robust estimation of the conditional probabilities in Eq. (2.4) is thus desired and achieved through L_1 norm optimization, i.e. $p = 1$.

Matches are iteratively updated through Eq. (2.2) and Eq. (2.4). Through iterations of the EM steps, weights are assigned to a set of blocks with highest similarity and are updated to find the best match.

Final transformation Once the translation \mathbf{T} is estimated, we apply \mathbf{T} and the initial rotation θ to the template, and calculate the similarity between the transformed template and the fetal image. Finally, we select the transformation maximizing the similarity value as the most probable transformation, that is,

$$\arg \max_{\theta, \mathbf{T}^\theta} NCC((\mathbf{T}^\theta \circ \theta) \mathbf{R}, \mathbf{S}) \quad (2.5)$$

where NCC corresponds to the Normalized Cross Correlation as image intensities may not be the same between the query and template images (see Figure 2.2).

Throughout the rest of this chapter, we will consider $\hat{\mathbf{T}}_s^1 = \hat{\mathbf{T}}^\theta \circ \hat{\theta}$ as the global rigid transformation estimated between the s -th query stack \mathbf{S} and the template.

2.4. Novel template-based brain localization and extraction for fetal MRI

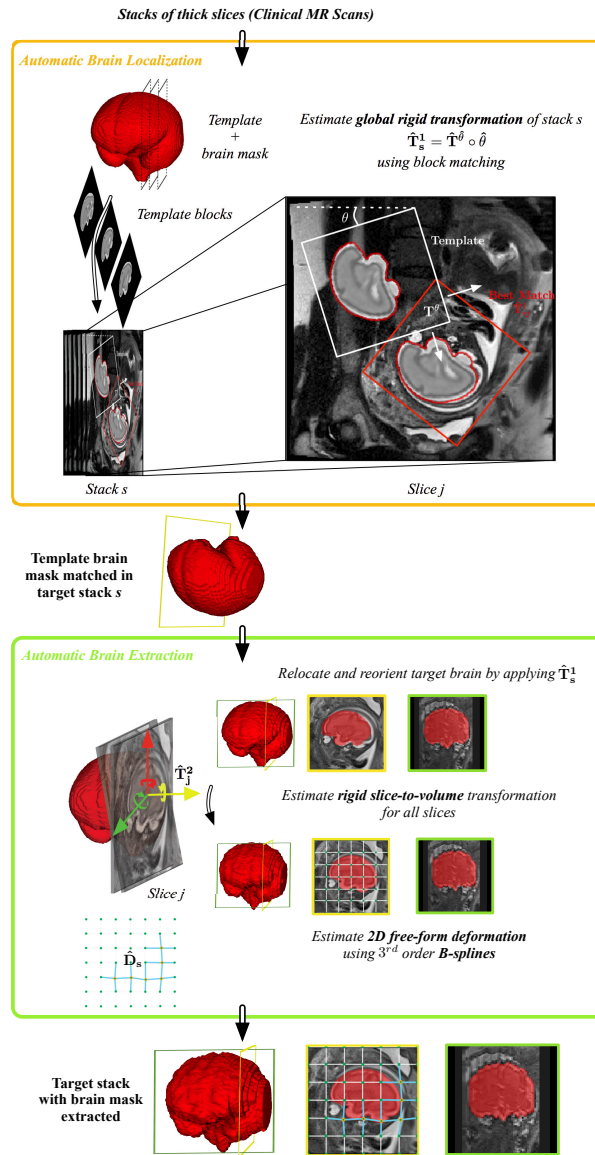


Figure 2.2 – Template-based brain localization and extraction from clinical MR scans. In each scan s , the initial global alignment and position of the fetal brain (global rigid transformation \hat{T}_s^1) is estimated using a block matching approach: 2D blocks of the age-matched template image are matched to slices in the fetal brain MRI scan. It corresponds to the brain localization step. The contour of the best match is indicated in red. Brain masks are then obtained through the brain extraction step. It consists of (i) cropping and reorienting the scan to the template space using \hat{T}_s^1 , (ii) performing rigid slice-to-template registration to refine the brain localization within the slice and to correct for inter-slice motion (rigid slice-to-template transformation \hat{T}_j^2), (iii) performing a 2D B-Spline deformable registration to take into account anatomical variability between the processed brain and the template brain (deformation field $\hat{D}_{s,j}$), and (iv) propagating the template brain mask to each slice, using the estimated transformations and deformation field.

2.4.2 Deformable slice-to-template brain extraction

Propagating the template brain mask by applying the global 3D rigid transformation estimated by the brain localization method may not be sufficient to obtain an accurate brain mask as 1) localization may not be perfect, 2) the shape of the template may be different from the query image, and 3) inter-slice motion can occur inside a stack of slices. In this section we develop a new deformable slice-to-template brain extraction method to obtain a more accurate brain mask to address these issues. The same template image used in the brain localization method is employed as reference here for brain extraction.

Deformable transformations: Let a local coordinate system be defined for every slice of every query stack s . The transformation between the slice in the s -th query stack and the template (high resolution volume) is defined as:

$$\mathbf{x}_{sj} = \underbrace{\mathbf{T}_j^2 \hat{\mathbf{T}}_s^1}_{\mathbf{T}_{sj}} \mathbf{y}_{sj}, \quad (2.6)$$

where \mathbf{x}_{sj} is slice voxel coordinate, \mathbf{y}_{sj} is the voxel coordinate in the template and \mathbf{T}_j^2 corresponds to the slice-to-template transformation. \mathbf{T}_j^2 is used to refine the brain localization within the slice and to correct for inter-slice motion. The deformation between the slice in the s -th query stack and the template (high resolution volume) is defined as:

$$\tilde{\mathbf{x}}_{sj} = \hat{\mathbf{T}}_{sj}^{-1} \mathbf{y}_{sj} + \mathbf{D}_j(\mathbf{y}_{sj}), \quad (2.7)$$

where $\tilde{\mathbf{x}}_{sj}$ is the voxel coordinate of the template deformed in the j -th slice of the s -th query stack, and \mathbf{D}_j is a 2D free-form deformation field. \mathbf{D}_j is modeled using B-Splines [34]. We determined a B-Spline order of 3 with grid size of 6×7 (as fetal brain is more elongated in the sagittal direction) yields the best compromise between an adequate amount of deformation and accuracy. It addresses the local anatomical variabilities/deformation that may exist between the template slice and the query slice. Therefore, the proposed method corrects for possible brain localization inaccuracy as well as for the inter-slice motion and takes into account anatomical variability between the processed brain and the template brain.

Metric and optimization: Similarly to the block matching algorithm, we select NCC as the optimization metric for both registration steps. Each registration phase is performed through maximizing NCC . Using NCC is very attractive as we can use common optimization algorithms. By considering this strategy in both steps, we first apply a regular-step gradient descent algorithm for the optimization of the slice-to-volume registration algorithm. The free-form deformation, however, has a much larger number of parameters as it is composed by the set of all the deformations associated with the nodes of the b-spline grid. For efficient optimization of the free-form deformation model, we choose to employ the Limited memory Broyden Fletcher Goldfarb Shannon optimization algorithm with simple Bounds (LBFGSB).

2.4. Novel template-based brain localization and extraction for fetal MRI

This optimization technique also gives us the opportunity to fix an upper bound, set to 4mm , on B-Spline control point displacements to prevent non-topology preserving deformations.

Brain label propagation: The brain mask in each slice is obtained by propagating the template brain mask to the slice using the estimated deformation field. Figure 2.2 illustrates the steps of our brain localization and extraction technique.

2.4.3 Intensity standardization

In fetal MRI, image intensities in the stacks may not be coherent with each other. This is due to inherent bias field inhomogeneity as well as possible maternal and fetal motions. To tackle this problem, we propose to successively correct *slice-by-slice* for the bias field using N4 [35] and standardize the intensities using 1) *slice-by-slice* mean intensity equalization and 2) *global* brain histogram equalization [36] (Box III in Figure 2.1). The rationale behind this approach is that the statistics and shape of the image histogram should be similar in the stacks as they represent the same brain anatomy.

2.4.4 Joint brain mask refinement and reconstruction

We propose to integrate our brain extraction method with the SR reconstruction process in an iterative fashion. The brain masks generated with our brain extraction method are more reliable for the central slices than those for the extremal slices; however, stacks are acquired in the three (approximately) orthogonal directions, and the masks of the extremal slices in one direction correspond to the masks of the central slices in the other two directions. Moreover, motion estimation and reconstruction is able to recover the alignment of slices in 3D HR space which allows refinement of the brain masks. We use these properties to design our brain mask refinement process, which is illustrated by the pipeline in Figure 2.3. It consists of:

- (i) mapping *slice-by-slice* every brain mask in the HR space using the estimated motion parameters,
- (ii) adopting a fusion strategy to obtain a unique HR brain mask,
- (iii) filtering using a Markov Random Field to obtain a coherent and smooth HR brain mask, and finally
- (iv) mapping back the HR brain mask to each slice of every stack.

Brain masks mapped in the HR space are combined ((ii) in Figure 2.3) using Simultaneous Truth And Performance Level Estimate (STAPLE) [37].

Let \mathbf{H} be the hidden binary refined HR brain mask and \mathbf{P} be the propagated brain masks. The STAPLE fusion consists of computing the most likely binary refined HR brain mask. STAPLE

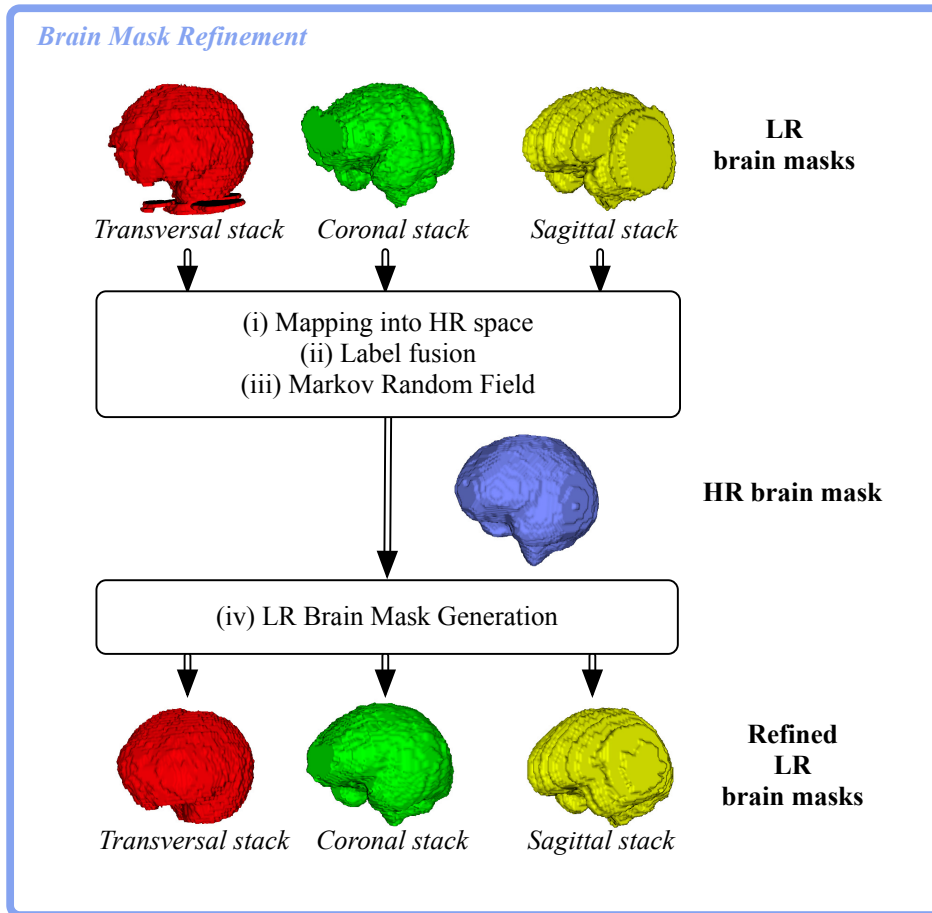


Figure 2.3 – Pipeline for refining LR brain masks. (i) maps *slice-by-slice* the brain mask of every stack into the HR space using the motion parameters estimated during motion estimation. (ii) applies a voting strategy to obtain a unique HR brain mask. (iii) applies a Markov Random Field filter to obtain a coherent HR brain mask. (iv) maps the refined HR brain mask back to each slice of the stacks. Note that this has been simplified for illustration; there are usually more than one stack of slices with their corresponding masks in each direction.

simultaneously estimates a probabilistic consensus brain mask and the quality of each brain mask using an Expectation-Maximization (EM) framework. It aims to estimate the sensitivity and specificity parameters (\mathbf{p}, \mathbf{q}) characterising the quality of the brain mask that maximizes the log likelihood function

$$\hat{\mathbf{p}}, \hat{\mathbf{q}} = \operatorname{argmax}_{\mathbf{p}, \mathbf{q}} \ln f(\mathbf{P}, \mathbf{H} | \mathbf{p}, \mathbf{q}) \quad (2.8)$$

where $f(\mathbf{P}, \mathbf{H} | \mathbf{p}, \mathbf{q})$ represents the probability mass function of the complete data. The process to identify quality parameters of the propagated brain mask and the HR brain mask is performed through iterations between 1) estimating the hidden HR mask given a previous estimate of the quality parameters of the propagated brain masks, and 2) estimating the quality parameters based on how accurate they are given the new estimate of the HR mask.

A binary estimate of the HR brain mask is made by thresholding the probabilistic HR brain mask at 0.5. However, it may result in a mask with holes due to motion-induced scattered nature of the acquisitions (the fetal brain might not be entirely covered by the acquired slices, thus the computed HR brain mask may contain gaps and holes.). To tackle this problem, we adopt an approach based on Markov Random Fields (MRF) ((iii) in Figure 2.3). Let \mathcal{C}_1 and \mathcal{C}_2 be a set of two classes. Let's consider \mathbf{H}_i (i -th voxel of the HR brain mask) belongs to \mathcal{C}_2 with centroid of 1 if it is a brain voxel, otherwise to \mathcal{C}_1 with centroid of 0. The generation of the binary estimate of the HR brain mask is performed as follows. A distance classifier is first employed to determine the Euclidean distance between each voxel to \mathcal{C}_1 and \mathcal{C}_2 . Then the distances of each voxel are updated by evaluating the influence of its neighbors based on a MRF model in a $7 \times 7 \times 3$ neighborhood. Influence of the neighbor voxels (in the same slice or in neighboring slices) are assumed to be equal with a weight value of 1. We used the iterated conditional modes (ICM) algorithm [38] to minimize the MRF labeling function. Each voxel is then classified to the class for which it has the minimum distance, and we obtain a closed binary estimate of the HR brain mask.

Finally, the HR brain mask is mapped back to each slice of every stack using the estimated motion parameters. As the reconstruction progresses, the segmentation of the original slices is refined thanks to their recovered alignment in 3D space.

2.5 Results

We carried out quantitative evaluation on clinical datasets. Firstly, we evaluate the performance of the proposed brain extraction technique compared to manual brain extraction. Secondly, we study the impact of rigid slice-to-template registration and 2D B-Spline deformation on the quality of the reconstructed image. Thirdly, we conduct a perceptual evaluation of the reconstructed images by expert observers. Finally, we investigate the potential of the brain mask refinement method to estimate the intra-cranial fetal brain volume in the reconstructed images. We assessed statistical significance of the results using the Wilcoxon signed-rank test.

2.5.1 Material

Our clinical dataset is formed by 87 stacks of thick slices coming from clinical MRI scans of 15 fetuses with normal brain and 5 fetuses with abnormal brain, aged between 25 and 35 weeks GA (see Table 2.1). Brain pathologies in this study were: abnormal cerebellum (P1), limited but normal gyration (P2), unilateral ventriculomegaly (P3), occipital meningocele (P4), and cerebellar hypoplasia (P5). Each fetal MRI scan consists of a set of 3 to 6 stacks, where at least one stack is available in each anatomical direction. Cases F1-F15, P1, P3 and P4 were scanned at Boston Children's Hospital, Boston, USA, using three different MRI scanners, including (1) a 1.5T Philips Achieva using a T2-weighted SSH-TSE sequence with a resolution of $1.29 \times 1.29 \times 2mm^3$ (TE/TR = 120/12500ms), (2) a 3T Siemens Trio using a T2-weighted HASTE sequence with a resolution of $1.17 \times 1.17 \times 3mm^3$ (TE/TR = 121/1600ms), and (3) a

Chapter 2. Automated Template-based Brain Localization and Extraction for Fetal Brain MRI Reconstruction

3T Siemens Skyra using a T2-weighted HASTE sequence with a resolution of $1 \times 1 \times 2 \text{mm}^3$ (TE/TR = 116-119/1600ms). Case P2 was scanned at Centre Hospital Universitaire de Vaud (CHUV), Lausanne, CH, using a 1.5T Siemens Aera and a T2-weighted HASTE sequence with a resolution of $1.13 \times 1.13 \times 4.8 \text{mm}^3$ (TE/TR = 89/1000ms). Case P5 was scanned at Hôpital Femme Mère Enfant, Lyon, France, using a 1.5T Philips Achieva and a T2-weighted SSH-TSE sequence with a resolution of $1.09 \times 1.09 \times 5.4 \text{mm}^3$ (TE/TR = 180/7000ms). Our acquisition settings allows us to acquire a majority of scans only affected by minor to moderate motion. We did not include scans with severe motion in the analysis.

Table 2.1 – Clinical datasets.

Case	GA	Stacks	Scanner	Sequence	Resolution
Healthy					
F1	27weeks	5	3.0T Siemens Skyra	HASTE	$1.00 \times 1.00 \times 2 \text{mm}^3$
F2	28weeks	5	1.5T Philips Achieva	SSH-TSE	$1.29 \times 1.29 \times 2 \text{mm}^3$
F3	28weeks	3	1.5T Philips Achieva	SSH-TSE	$1.29 \times 1.29 \times 2 \text{mm}^3$
F4	29weeks	4	1.5T Philips Achieva	SSH-TSE	$1.29 \times 1.29 \times 2 \text{mm}^3$
F5	29weeks	4	3.0T Siemens Skyra	HASTE	$1.00 \times 1.00 \times 2 \text{mm}^3$
F6	30weeks	5	1.5T Philips Achieva	SSH-TSE	$1.29 \times 1.29 \times 2 \text{mm}^3$
F7	30weeks	6	3.0T Siemens Skyra	HASTE	$1.00 \times 1.00 \times 2 \text{mm}^3$
F8	31weeks	4	1.5T Philips Achieva	SSH-TSE	$1.29 \times 1.29 \times 2 \text{mm}^3$
F9	31weeks	3	3.0T Siemens Skyra	HASTE	$1.00 \times 1.00 \times 2 \text{mm}^3$
F10	32weeks	6	3.0T Siemens Trio	HASTE	$1.17 \times 1.17 \times 3 \text{mm}^3$
F11	33weeks	3	1.5T Philips Achieva	SSH-TSE	$1.29 \times 1.29 \times 2 \text{mm}^3$
F12	33weeks	5	3.0T Siemens Skyra	HASTE	$1.00 \times 1.00 \times 2 \text{mm}^3$
F13	34weeks	5	1.5T Philips Achieva	SSH-TSE	$1.29 \times 1.29 \times 2 \text{mm}^3$
F14	35weeks	3	1.5T Philips Achieva	SSH-TSE	$1.29 \times 1.29 \times 2 \text{mm}^3$
F15	35weeks	4	1.5T Philips Achieva	SSH-TSE	$1.29 \times 1.29 \times 2 \text{mm}^3$
Pathological					
P1	25weeks	4	3.0T Siemens Trio	HASTE	$1.17 \times 1.17 \times 3 \text{mm}^3$
P2	26weeks	3	1.5T Siemens Aera	HASTE	$1.12 \times 1.12 \times 4.8 \text{mm}^3$
P3	26weeks	6	3.0T Siemens Trio	HASTE	$1.17 \times 1.17 \times 3 \text{mm}^3$
P4	30weeks	4	3.0T Siemens Trio	HASTE	$1.17 \times 1.17 \times 3 \text{mm}^3$
P5	34weeks	5	1.5T Philips Achieva	SSH-TSE	$1.09 \times 1.09 \times 5.4 \text{mm}^3$
Total		87			

The patient information from all data used in this study was anonymized and de-identified prior to analysis. Retrospective analysis of this data was approved by the corresponding committee / institutional review board committee: USA (institutional review board committee at Boston Children’s Hospital), Switzerland (Cantonal Research Ethics Committee of Vaud) and France (Comité de Protection des Personnes).

2.5.2 Performance of brain extraction

We assess the evolution of the performance of our *slice-to-template* brain extraction in terms of brain segmentation quality, as motion-estimation and brain mask refinement progress, using manual delineation as *ground truth*. Manual delineations were performed for every stack after they were reoriented and cropped around the fetal brain thanks to the brain localization method. Similar to [29], the performance is quantified by three overlap metrics: Dice, recall and precision. While Dice summarizes recall and precision, recall quantifies the proportion of true positive brain voxels included in the mask and precision quantifies the proportion of non-brain voxels excluded. We compare the full brain extraction method that combines global rigid block matching with rigid slice-to-template registration and 2D B-Spline deformation with a method that uses only the rigid slice-to-template registration without deformation. The experiment was performed by repeating the brain mask refinement loop *three* times. The results of the rigid-only and the full brain extraction methods as well as results obtained right after brain localization are reported in Table 2.2. Figure 2.4 illustrates the evolution of the brain mask of one coronal stack through the developed pipeline.

Table 2.2 – Evolution of brain extraction performance as reconstruction progresses using (i) rigid-only slice-to-template registration and (ii) rigid and B-Spline based deformable slice-to-template registration (full method). Loop # L corresponds to the L^{th} brain mask refinement loop. Loop #0 corresponds to the performance of brain extraction without any refinement. Best results, specifically in terms of the overall agreement with manual delineation (Dice) and in terms of the proportion of true positive brain voxels included in the mask (recall), can be observed using the full method after repeating *two* times the refinement loop.

	Dice	Recall	Precision
Localization	92.0 ± 3.5	89.8 ± 5.3	94.6 ± 4.0
Extraction			
Loop #0			
Rigid-only	93.4 ± 2.6	92.7 ± 2.6	94.3 ± 4.3
Full	93.5 ± 2.7	92.9 ± 2.9	94.3 ± 4.3
Loop #1			
Rigid-only	94.2 ± 1.9	94.3 ± 2.8	94.1 ± 2.6
Full	94.5 ± 1.6	94.6 ± 2.6	94.4 ± 2.7
Loop #2			
Rigid-only	94.3 ± 1.6	94.8 ± 2.4	94.0 ± 2.5
Full	94.5 ± 1.5	94.9 ± 2.4	94.2 ± 2.5
Loop #3			
Rigid-only	94.4 ± 1.6	94.7 ± 2.4	94.1 ± 2.6
Full	94.5 ± 1.6	94.9 ± 2.5	94.1 ± 2.6

It is clear that the proposed brain extraction method improves the quality of the brain masks obtained from brain localization, i.e., only global alignment. The results also show that the full pipeline helps to enhance the quality of the brain masks compared to the rigid-only

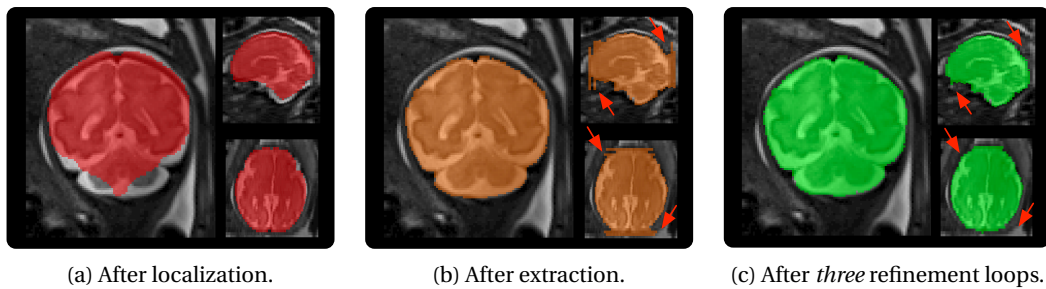


Figure 2.4 – Brain mask evolution. Arrows indicate extremal slices where the proposed slice-to-template brain extraction method failed. The brain masks are progressively refined thanks to motion estimation and reconstruction that helped recovering the slice alignment in 3D HR space.

approach. This shows it is important to take into account anatomical variability between the age-matched template brain and the target brain to obtain accurate brain masks. Finally, it is observed that the proposed iterative strategy to refine the brain masks as the motion estimation and reconstruction proceed, improves the quality of the brain masks particularly with an increase in the proportion of true positive brain voxels (recall). This shows that brain masks in orthogonal stacks are complimentary to each other. Alignment in 3D HR space recovered by motion estimation can indeed serve as a useful feedback to refine the extremal slices of stacks where the *slice-to-template* brain extraction method may fail (See arrows in Fig. 2.4 (b) and (c)).

2.5.3 Influence of brain extraction on reconstruction quality

Our ultimate goal is to reconstruct high-resolution, high-quality images of the fetal brain while we achieve brain segmentation simultaneously. Statistically significant improvement of the quality of brain extraction is however not an indicator of an improvement of the quality of the reconstructed image. We propose to investigate for the first time the influence of automatic brain extraction on the reconstruction quality. To do so, we compare the reconstruction quality in terms of Peak Signal-to Noise Ratio (PSNR) of the final HR image reconstructed using brain masks obtained by performing (i) only brain localization (no *slice-to-template* registration), denoted as Localization, (ii) both brain localization and extraction while using rigid-only *slice-to-template* registration, denoted as Rigid-only, and (iii) both brain localization and extraction while using the full *slice-to-template* brain extraction method (rigid and B-Spline deformation), denoted as Full. The HR image reconstructed using manual brain masks is considered the reference for PSNR calculation. We also study the evolution of the image reconstruction quality as we iterate over motion-estimation and brain mask refinement. Figure 2.5 shows the boxplot analysis of the evolution of the PSNR values of 20 cases for 3 methods. Figure 2.6 gives a comparison of the reconstructed images with the different approaches for one case, representative of all cases.

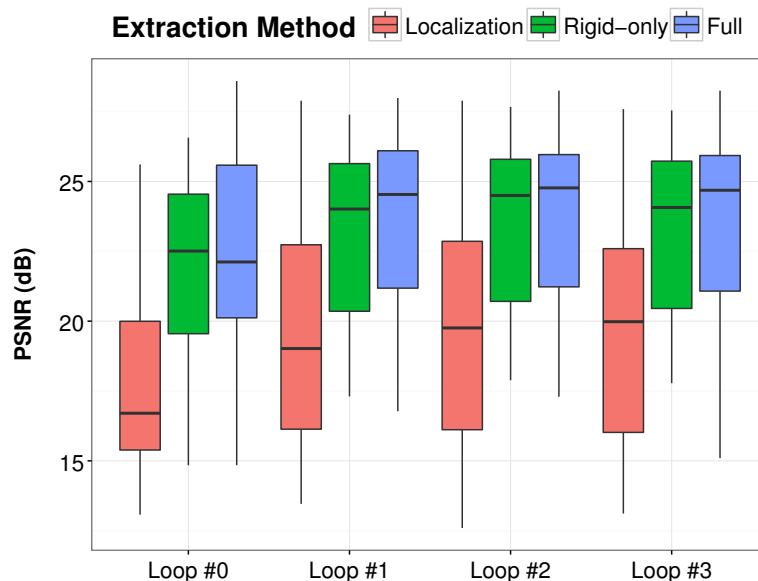


Figure 2.5 – Influence of brain extraction on image reconstruction quality in terms of Peak-Signal-to-Noise Ratios (PSNR) as reconstruction progresses using (i) only brain localization (Localization-only), (ii) rigid-only *slice-to-template* registration (Rigid-only) and (iii) the full method (Full). We use as reference the image reconstructed with the help of brain masks manually drawn after brain localization. Loop # L corresponds to the L^{th} brain mask refinement loop. Loop #0 corresponds to the first image reconstructed using brain masks without any refinement. We can observe a significant improvement of the PSNR values after the first refinement (Loop #1) that becomes not significant after the second refinement (Loop #2). Adopting a rigid-only *slice-to-template* registration significantly improves the quality of the reconstructed HR image obtained at Loop #2 with an average increase of 3.8dB (p-value= $5.9e-4$) in the PSNR value. Using the full method allows us to further enhance the quality with an average increase of 4.1dB (p-value= $3.9e-4$) with respect to using only brain localization and an average increase of 0.3dB (p-value= 0.047) with respect to using the rigid-only method.

Quantitative results and visual inspection confirm that a better brain extraction performance (as shown in Section 2.5.2) results in a better final reconstruction quality. We can observe a significant increase of the PSNR value after the first refinement loop (Loop #1 in Figure 2.5) that, in conjunction to the brain extraction performance, stabilizes after the second refinement (Loop #2 in Figure 2.5), *independently* of the method adopted. In addition, we can also clearly see that adopting a rigid-only *slice-to-template* registration significantly improves the quality of the reconstructed HR image obtained at Loop #2 with an average increase of 3.8dB (p-value= $5.9e-4$) in the PSNR value. Using the full method allows us to further enhance the quality with an average increase of 4.1dB (p-value= $3.9e-4$) with respect to using only brain localization and an average increase of 0.3dB (p-value= 0.047) with respect to using the rigid-only method. This indicates that best brain extraction performance and best reconstruction quality are obtained with the proposed pipeline after repeating only *two* refinement loops. Based on these observations, for the next analyses we used images reconstructed by the

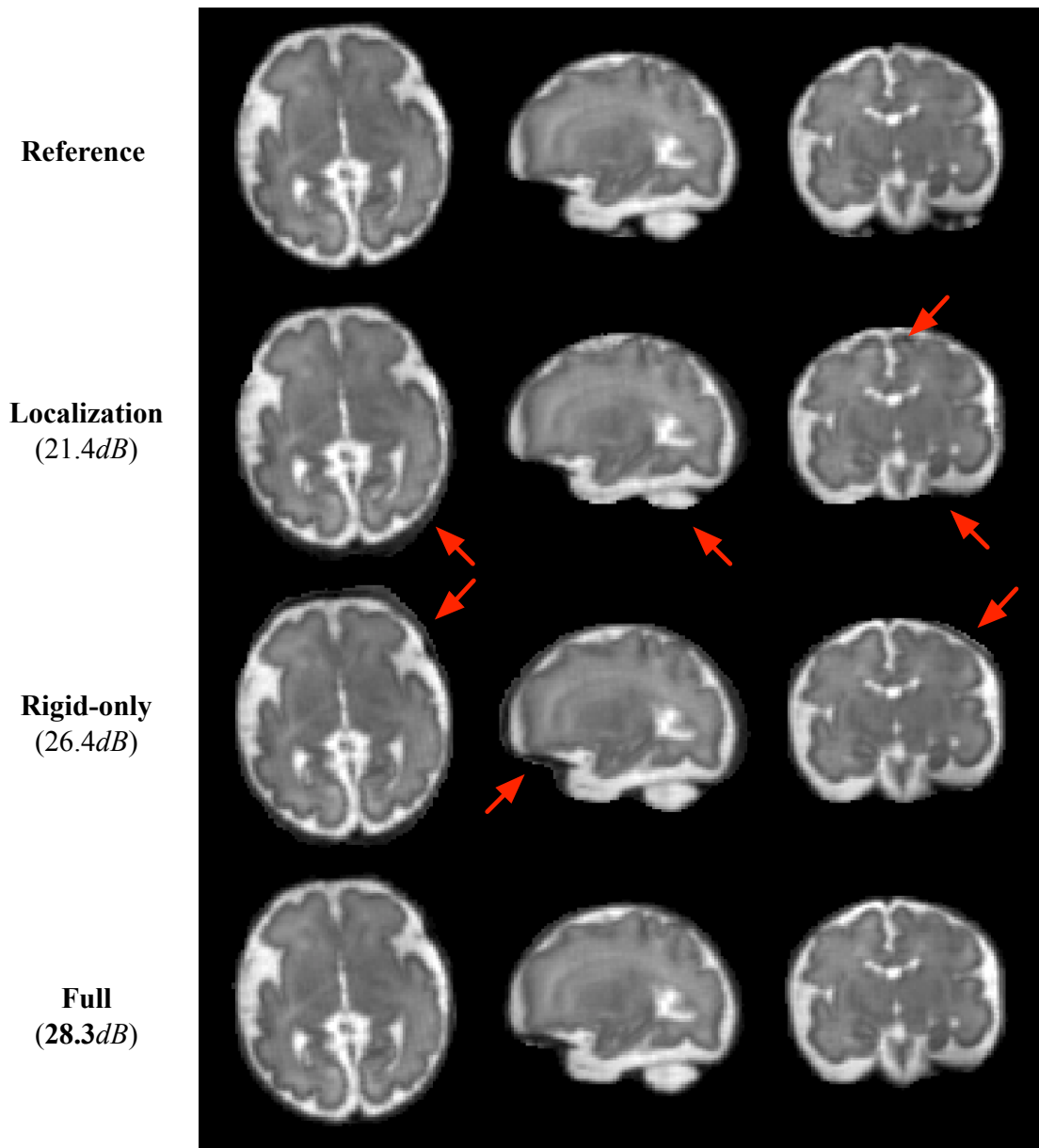


Figure 2.6 – Comparison of reconstruction results of case F10 using (i) only brain localization (Localization-only), (ii) rigid-only *slice-to-template* registration (Rigid-only) and (iii) the full method (Full). Arrows indicate artifacts and non-brain regions included in the reconstructed image. In general, we can observe a reconstructed image of poor quality when we use brain masks obtained right after localization (method (i)). Using the brain masks obtained by methods (ii) and (iii) allows us to have a reconstructed image with a quality very similar to the quality of the image obtained using manually drawn brain masks (Reference). Only small differences can be observed at the periphery of the brain.

proposed pipeline after *two* refinement loops.

2.5.4 Perceptual evaluation of final reconstruction by expert observers

Quantitative evaluation of the quality of the reconstruction and perceived visual quality may differ in clinical settings. We propose in this section to conduct a perceptual evaluation by expert observers to compare the reconstructed images using the fully automated reconstruction pipeline with *two* brain mask refinement loops (as supported by results presented in Sections 2.5.2 and 2.5.3) against images reconstructed using manually drawn brain masks. We adopted a multi-alternative force-choice approach where we asked two expert observers to indicate the best HR image in terms of perceived image quality. The two reconstructed images were presented in random order. The experts had the choice between either choosing one of the images as the best or judging both having similar quality. Ratings of the two expert observers are reported in Table 2.3, and representative reconstructed images of a pathological brain (Figure 2.7a), diagnosed with unilateral ventriculomegaly, and a healthy brain (Figure 2.7b) are shown in Figure 2.7.

Table 2.3 – Qualitative rating of final reconstruction by two expert observers. Experts were asked to indicate the best HR image in terms of perceived image quality between images reconstructed using the full reconstruction pipeline and images reconstructed using manually drawn brain masks. For each expert, we report the number of cases when he preferred the image reconstructed using manually drawn brain masks (Manual), the image reconstructed with the full reconstruction pipeline (Full), or when both images were judged having similar quality (Similar).

	Manual	Full	Similar
Expert #1	7	7	6
Expert #2	8	4	8

In summary, images reconstructed by the proposed automatic pipeline were respectively judged in 13 / 12 cases as having similar or better quality to images reconstructed where manual brain masks were used. We found three reasons why images reconstructed using manual brain masks were preferred: 1) the reconstruction quality of both images was similar but small regions of the brain were missing in the reconstructed image; 2) the reconstruction quality of both images was similar but small regions outside the brain were included in the image reconstructed by the proposed pipeline (Figure 2.7b); 3) the region reconstructed containing the brain was similar in both images but a few more artifacts were present in the image reconstructed by the proposed pipeline. Finally, successful reconstruction of brain images with severe pathologies such as the unilateral ventriculomegaly (in Figure 2.7a) demonstrates that the proposed pipeline can be used for fully automatic fetal brain MRI reconstruction process for both healthy and pathological cases without compromising reconstruction quality.

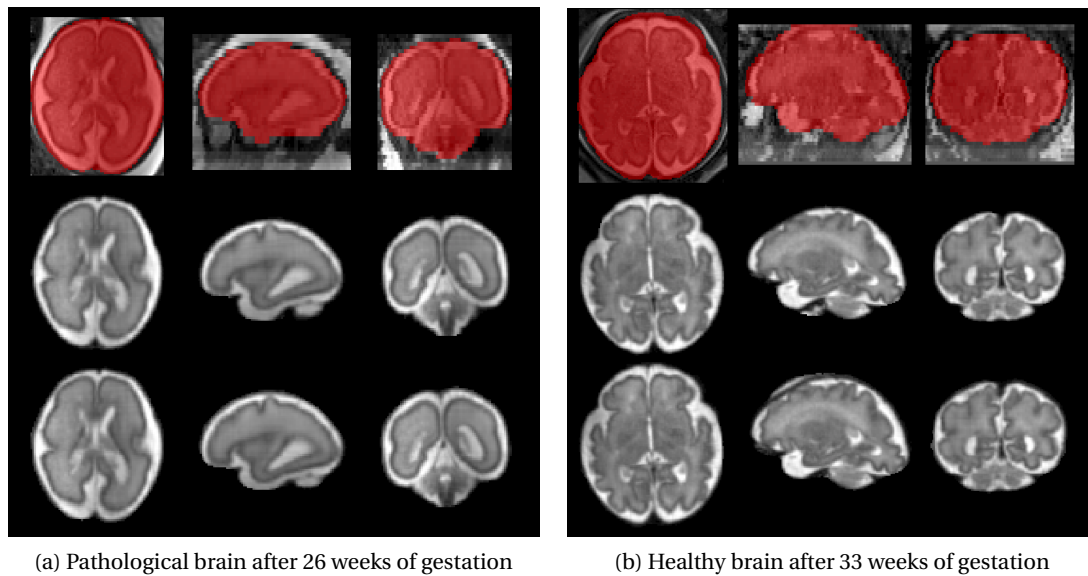


Figure 2.7 – Brain extraction and reconstruction results of one pathological brain diagnosed with unilateral ventriculomegaly (Case P3) and one healthy brain (Case F12). An overlay of the original low-resolution image with the brain mask automatically extracted is shown in the first row. The reconstruction results obtained using the brain masks manually drawn and the brain masks automatically extracted are shown in the second and third row respectively. Case P3 illustrates one case where the expert observers judged both reconstructed images having the same quality. Case F12 illustrates one case where the expert observers preferred the image reconstructed using manual brain masks as a small region outside the brain was included in the fully automated reconstruction. These results, representative of all, showed that using the proposed method allowed us to obtain fully automatic high-quality reconstructions without the need for manual brain localization or extraction.

2.5.5 Application to intra-cranial fetal brain volumetry

In this section we evaluate the potential of the proposed full brain extraction method combined with the proposed brain mask refinement method to estimate intra-cranial fetal brain volumes in millilitres (mL). We compare the volumes estimated after one iteration of the proposed pipeline where we use the brain masks manually drawn after brain localization (hence no need of mask refinement) against volumes automatically estimated using the full method. The total intra-cranial volume was estimated from the refined HR brain mask. Figure 2.8 shows the results of Bland-Altman analysis.

This analysis indicates that volumes obtained automatically are highly correlated with the volumes obtained using manual brain masks. This indicates that the combination of the proposed brain extraction and brain mask refinement methods (originally designed to update brain masks in the stacks of slices) can be used to estimate the intra-cranial fetal brain volume with an average approximate accuracy of -3.1% . But the analysis also shows a tendency to slightly underestimating the volumes with a mean difference of $-8mL$ while using the

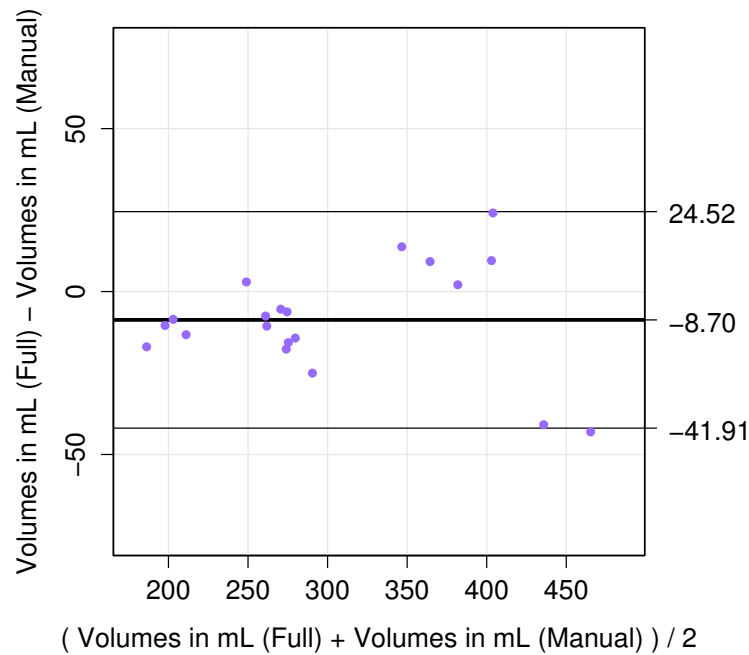


Figure 2.8 – Bland-Altman plot of intra-cranial fetal brain volumetry results. It shows a good correlation between volumes estimated using manually drawn brain masks and volumes estimated using brain masks obtained by the full method. However, we can observe a tendency to slightly underestimate the volumes (-8.7mL on average) while using the automatic brain masks.

automatically extracted brain masks.

2.6 Discussion

The proposed method enables automatic brain masking, showing an average Dice overlap measure of 94.5% with respect to manually-drawn brain masks. In addition, the success of motion correction is highly dependent on the initial alignment of all stacks. After brain localization, the orientation of the brain in each stack is known as the localization method aims to estimate the global rigid transformation between each stack and the template brain which is correctly oriented. Thus, after brain localization and application of the rigid transform, each stack is oriented to template orientation making the alignment of all stacks consistent.

The study of the evolution of brain extraction performance (Section 2.5.2) and its impact on reconstruction quality (Section 2.5.3) shows that it is crucial to refine the global 3D alignment *slice-by-slice* as slice acquisition is interleaved and fetal and maternal motion may result in the inclusion of non-brain tissue and amniotic fluid that can decrease the quality of motion estimation and consequently image reconstruction. In addition, the inclusion of 2D B-Spline

Chapter 2. Automated Template-based Brain Localization and Extraction for Fetal Brain MRI Reconstruction

deformable registration in the *slice-to-template* extraction method has shown to generate 1) superior brain extraction performance, and 2) superior-quality reconstructions compared to rigid alignment methods. This confirms the importance of taking into account anatomical variability between the age-matched template brain and the target brain in the brain extraction framework.

Results point out the success of the integration of the proposed localization and extraction method into our new reconstruction pipeline that iterates over intensity standardization, inter-slice motion estimation and brain mask refinement, statistically improving both brain extraction performance and image reconstruction quality. It has also shown to be a very promising way to automatically estimate at the same time the intra-cranial fetal brain volume in the final reconstructed image.

Successful brain localization, extraction, and reconstruction is highly dependent on good image acquisition practice and on the robustness of the automatic image processing algorithms [1]. Good image acquisition practice addresses the need for 1) appropriate MRI sequence parameters that allow motion-robust slice acquisitions at about few hundred milliseconds instant of k -space sampling for each slice and 2) multiple repeated scans to provide the required redundancy for brain extraction refinement, motion estimation, and reconstruction. Even if good acquisition practice is fulfilled, minor to severe motions can still occur resulting in minor to severe artifacts in the acquired slices. This justifies the need for automatic robust image processing algorithms that can detect and reject bad data and use only good-quality data with minor to moderate motion for reconstruction. With the design and development of smart motion detection algorithms and robust reconstruction beyond the methods proposed in [4, 6], it will be possible to handle fetal MRI cases with severe motion artifacts. Such developments are expected to significantly improve the efficacy of fetal MRI in terms of accuracy, reliability, and may in-turn lead to much shorter overall scan times while providing high-quality results.

2.7 Conclusion

In summary, we proposed and evaluated a novel template-based approach automatizing localization, extraction and refinement of the fetal brain in the fetal MRI reconstruction pipeline. It combines *template-to-slice* block matching to localize the brain, a novel *slice-to-template* brain extraction approach to find automatically, *slice-by-slice*, the brain masks, and a novel brain mask refinement method that updates the mask as reconstruction proceeds. The results confirm the success of the method: a template-based approach adopted for automatic brain localization, is followed by brain extraction and brain mask refinement, to generate 3D reconstructed images of the fetal brain from stacks of slices corrupted with minor to moderate inter-slice motion artifacts. Automatic brain extraction and reconstruction mitigates the need for manual brain localization and the subjectivity of manual delineation.

Next chapter will take advantage of this completely automated HR image reconstruction

pipeline to investigate the feasibility of designing a completely automatic image processing pipeline for in utero cortical folding quantification.

Acknowledgment

This work was supported in part by the Swiss National Science Foundation under PhD Mobility Grant SNSF-141283, the CIBM of Geneva-Lausanne Universities and EPFL, the Fondation Leenaards and Fondation Louis-Jeantet, and in part by the National Institutes of Health (NIH) grants R01EB0118988, R01EB013248, and R03DE22109. The authors would like to thank Prof. Laurent Guibaud for providing access to the SSFSE data.

Bibliography

- [1] A. Gholipour, J. A. Estroff, C. E. Barnewolt, R. L. Robertson, P. E. Grant, B. Gagoski, S. K. Warfield, O. Afacan, S. A. Connolly, J. J. Neil, et al., Fetal MRI: A technical update with educational aspirations, *Concepts in Magnetic Resonance Part A* 43 (6) (2014) 237–266.
- [2] F. Rousseau, O. A. Glenn, B. Iordanova, C. Rodriguez-Carranza, D. B. Vigneron, J. A. Barkovich, C. Studholme, Registration-based approach for reconstruction of high-resolution in utero fetal MR brain images, *Academic Radiology* 13 (9) (2006) 1072–1081.
- [3] S. Jiang, H. Xue, A. Glover, M. Rutherford, D. Rueckert, J. Hajnal, MRI of moving subjects using multislice snapshot images with volume reconstruction (SVR): Application to fetal, neonatal, and adult brain studies, *Medical Imaging, IEEE Transactions on* 26 (7) (2007) 967–980.
- [4] A. Gholipour, J. Estroff, S. Warfield, Robust super-resolution volume reconstruction from slice acquisitions: Application to fetal brain MRI, *Medical Imaging, IEEE Transactions on* 29 (10) (2010) 1739–1758.
- [5] F. Rousseau, E. Oubel, J. Pontabry, M. Schweitzer, C. Studholme, M. Koob, J.-L. Dietemann, BTK: An open-source toolkit for fetal brain MR image processing, *Computer Methods and Programs in Biomedicine* 109 (1) (2013) 65–73.
- [6] M. Kuklisova-Murgasova, G. Quaghebeur, M. A. Rutherford, J. V. Hajnal, J. A. Schnabel, Reconstruction of fetal brain MRI with intensity matching and complete outlier removal, *Medical Image Analysis* 16 (8) (2012) 1550–1564.
- [7] M. Fogtmann, S. Seshamani, K. Kim, T. Chapman, C. Studholme, A unified approach for motion estimation and super resolution reconstruction from structural magnetic resonance imaging on moving objects, in: *MICCAI workshop on Perinatal and Paediatric Imaging: PaPI*, 2012, pp. 9–16.
- [8] S. Tourbier, X. Bresson, P. Hagmann, J.-P. Thiran, R. Meuli, M. Bach Cuadra, Efficient total variation algorithm for fetal brain MRI reconstruction, in: P. Golland, N. Hata, C. Barillot, J. Hornegger, R. Howe (Eds.), *Medical Image Computing and Computer Assisted Intervention (MICCAI)*, International Conference on, no. 8674 in *Lecture Notes in Computer Science*, Springer, 2014, pp. 252–259.
- [9] B. Kainz, M. Steinberger, W. Wein, M. Kuklisova-Murgasova, C. Malamateniou, K. Keraudren, T. Torsney-Weir, M. Rutherford, P. Aljabar, J. V. Hajnal, et al., Fast volume reconstruction from motion corrupted stacks of 2D slices, *Medical Imaging, IEEE Transactions on* 34 (9) (2015) 1901–1913.
- [10] S. Tourbier, X. Bresson, P. Hagmann, J.-P. Thiran, R. Meuli, M. B. Cuadra, An efficient total variation algorithm for super-resolution in fetal brain MRI with adaptive regularization, *NeuroImage* 118 (2015) 584–597.

Chapter 2. Automated Template-based Brain Localization and Extraction for Fetal Brain MRI Reconstruction

- [11] B. Caldairou, N. Passat, P. A. Habas, C. Studholme, M. Koob, J.-L. Dietemann, F. Rousseau, Segmentation of the cortex in fetal MRI using a topological model, in: *Biomedical Imaging (ISBI), International Symposium on, IEEE, 2011*, pp. 2045–2048.
- [12] J. Corbett-Detig, P. Habas, J. Scott, K. Kim, V. Rajagopalan, P. McQuillen, A. Barkovich, O. Glenn, C. Studholme, 3D global and regional patterns of human fetal subplate growth determined in utero, *Brain Structure and Function* 215 (2011) 255–263.
- [13] P. A. Habas, J. A. Scott, A. Roosta, V. Rajagopalan, K. Kim, F. Rousseau, A. J. Barkovich, O. A. Glenn, C. Studholme, Early folding patterns and asymmetries of the normal human brain detected from in utero MRI, *Cerebral Cortex* 22 (1) (2012) 13–25.
- [14] J. A. Scott, P. A. Habas, K. Kim, V. Rajagopalan, K. S. Hamzelou, J. M. Corbett-Detig, A. J. Barkovich, O. A. Glenn, C. Studholme, Growth trajectories of the human fetal brain tissues estimated from 3D reconstructed in utero MRI, *International Journal of Developmental Neuroscience* 29 (5) (2011) 529–536.
- [15] A. Gholipour, A. Akhondi-Asl, J. A. Estroff, S. K. Warfield, Multi-atlas multi-shape segmentation of fetal brain MRI for volumetric and morphometric analysis of ventriculomegaly, *NeuroImage* 60 (3) (2012) 1819–1831.
- [16] C. Clouchoux, D. Kudelski, A. Gholipour, S. K. Warfield, S. Viseur, M. Bouyssi-Kobar, J.-L. Mari, A. C. Evans, A. J. Du Plessis, C. Limperopoulos, Quantitative in vivo MRI measurement of cortical development in the fetus, *Brain Structure and Function* 217 (1) (2012) 127–139.
- [17] C. Clouchoux, A. Du Plessis, M. Bouyssi-Kobar, W. Tworetzky, D. McElhinney, D. Brown, A. Gholipour, D. Kudelski, S. Warfield, R. McCarter, et al., Delayed cortical development in fetuses with complex congenital heart disease, *Cerebral Cortex* 23 (12) (2013) 2932–2943.
- [18] R. Wright, V. Kyriakopoulou, C. Ledig, M. Rutherford, J. Hajnal, D. Rueckert, P. Aljabar, Automatic quantification of normal cortical folding patterns from fetal brain MRI, *NeuroImage* 91 (0) (2014) 21–32.
- [19] K. Kim, P. Habas, F. Rousseau, O. Glenn, A. Barkovich, C. Studholme, Intersection based motion correction of multislice MRI for 3-D in utero fetal brain image formation, *Medical Imaging, IEEE Transactions on* 29 (1) (2010) 146–158.
- [20] S. M. Smith, Fast robust automated brain extraction., *Human Brain Mapping* 17 (3) (2002) 143–155.
- [21] F. Shi, L. Wang, J. H. Gilmore, W. Lin, D. Shen, Learning-based meta-algorithm for MRI brain extraction, in: *Medical Image Computing and Computer Assisted Intervention (MICCAI), International Conference on*, no. 6893 in *Lecture Notes in Computer Science*, Springer, 2011, pp. 313–321.

-
- [22] J. Anquez, E. D. Angelini, I. Bloch, Automatic segmentation of head structures on fetal MRI., in: Biomedical Imaging (ISBI), International Symposium on, IEEE, 2009, pp. 109–112.
- [23] Y. Taleb, M. Schweitzer, C. Studholme, M. Koob, J.-L. Dietemann, F. Rousseau, Automatic template-based brain extraction in fetal MR images, in: Organization for Human Brain Mapping (OHBM) conference., 2013.
- [24] S. Tourbier, P. Haggmann, M. Cagneaux, L. Guibaud, S. Gorthi, M. Schaer, J.-P. Thiran, R. Meuli, M. B. Cuadra, Automatic brain extraction in fetal MRI using multi-atlas-based segmentation, in: Proc. SPIE Medical Imaging, Vol. 9413, 2015, pp. 94130Y–94130Y–7.
- [25] V. Taimouri, A. Gholipour, C. Velasco-Annis, J. Estroff, S. K. Warfield, A template-to-slice block matching approach for automatic localization of brain in fetal MRI, in: Biomedical Imaging (ISBI), International Symposium on, IEEE, 2015, pp. 144–147.
- [26] M. Ison, E. Dittrich, R. e. Donner, G. Kaspran, D. Prayer, G. Langs, Fully automated brain extraction and orientation in raw fetal MRI, MICCAI workshop on Perinatal and Paediatric Imaging: PaPI (2012) 17–24.
- [27] K. Keraudren, V. Kyriakopoulou, M. A. Rutherford, J. V. Hajnal, D. Rueckert, Localisation of the brain in fetal MRI using bundled SIFT features., in: K. Mori, I. Sakuma, Y. Sato, C. Barillot, N. Navab (Eds.), Medical Image Computing and Computer Assisted Intervention (MICCAI), International Conference on, Vol. 8149 of Lecture Notes in Computer Science, Springer, 2013, pp. 582–589.
- [28] B. Kainz, K. Keraudren, V. Kyriakopoulou, M. Rutherford, J. V. Hajnal, D. Rueckert, Fast fully automatic brain detection in fetal MRI using dense rotation invariant image descriptors, in: Biomedical Imaging (ISBI), International Symposium on, IEEE, 2014, pp. 1230–1233.
- [29] K. Keraudren, M. Kuklisova-Murgasova, V. Kyriakopoulou, C. Malamateniou, M. Rutherford, B. Kainz, J. Hajnal, D. Rueckert, Automated fetal brain segmentation from 2D MRI slices for motion correction, NeuroImage 101 (2014) 633–643.
- [30] A. Gholipour, C. Limperopoulos, S. Clancy, C. Clouchoux, A. Akhondi-Asl, J. A. Estroff, S. K. Warfield, Construction of a deformable spatiotemporal MRI atlas of the fetal brain: Evaluation of similarity metrics and deformation models, in: P. Golland, N. Hata, C. Barillot, J. Hornegger, R. Howe (Eds.), Medical Image Computing and Computer Assisted Intervention (MICCAI), International Conference on, Vol. 8674 of Lecture Notes in Computer Science, Springer, 2014, pp. 292–299.
- [31] T. S. Yoo, M. J. Ackerman, W. E. Lorensen, W. Schroeder, V. Chalana, S. Aylward, D. Metaxas, R. Whitaker, Engineering and algorithm design for an image processing API: A technical report on ITK - the Insight Toolkit, in: J. Westwood (Ed.), Proc. of Medicine Meets Virtual Reality, Vol. 85, IOS Press Amsterdam, 2002, pp. 586–592.

Chapter 2. Automated Template-based Brain Localization and Extraction for Fetal Brain MRI Reconstruction

- [32] W. Johnson, J. Lindenstrauss, Extensions of Lipschitz mappings into a Hilbert space, in: Conference in modern analysis and probability, Vol. 26 of Contemporary Mathematics, American Mathematical Society, 1984, pp. 189–206.
- [33] S. Granger, X. Pennec, Multi-scale EM-ICP: A fast and robust approach for surface registration, in: A. Heyden, G. Sparr, M. Nielsen, P. Johansen (Eds.), European Conference on Computer Vision, Vol. 2353 of Lecture Notes in Computer Science, Springer Berlin Heidelberg, 2002, pp. 418–432.
- [34] D. Rueckert, L. I. Sonoda, C. Hayes, D. L. Hill, M. O. Leach, D. J. Hawkes, Nonrigid registration using free-form deformations: application to breast MR images, *Medical Imaging, IEEE Transactions on* 18 (8) (1999) 712–721.
- [35] N. J. Tustison, B. B. Avants, P. A. Cook, Y. Zheng, A. Egan, P. A. Yushkevich, J. C. Gee, N4ITK: improved N3 bias correction, *Medical Imaging, IEEE Transactions on* 29 (6) (2010) 1310–20.
- [36] L. G. Nyúl, J. K. Udupa, X. Zhang, New variants of a method of MRI scale standardization, *Medical Imaging, IEEE Transactions on* 19 (2) (2000) 143–150.
- [37] S. Warfield, K. Zou, W. Wells, Simultaneous truth and performance level estimation (STAPLE): an algorithm for the validation of image segmentation, *Medical Imaging, IEEE Transactions on* 23 (7) (2004) 903–921.
- [38] J. Besag, On the statistical analysis of dirty pictures, *Journal of the Royal Statistical Society. Series B* 48 (3) (1986) 259–302.

3

Quantification of Fetal Cortical Folding using Super-Resolution MRI Reconstruction and FreeSurfer

The work in this chapter was presented as first author for poster presentation at the Organization for Human Brain Mapping (OHBM) 2016 meeting as [S. Tourbier](#), M. Schaer, S. K. Warfield, R. Meuli, A. Gholipour, M. Bach Cuadra, “**Quantification of Fetal Cortical Folding using Slice-to-Volume Reconstructed MRI and FreeSurfer**”.

3.1 Introduction

The excellent contrast between cortical gray matter (GM) and adjacent white matter (WM) provided by SST2W imaging and the reconstruction of motion-free high-resolution (HR) MR images of the fetal brain has opened new research perspectives in the analysis of cortical folding in early brain development. Cortical folding, also known as gyrification is a good indicator of fetal brain maturation as it is one of the most dramatic structural changes happening during gestation. Especially, major changes occur after around 24 weeks, leading to a dramatic increase in cortical surface area without any similar increase in cortical thickness. This process allows more neurons to be organized in the limited intra-cranial spaces and it is thought to be correlated to human intelligence. It is in turn critical to normal development and early diagnosis could allow better care for the patient. Brain tissue segmentation with accurate delineation of the inner surface of the cortical plate is an essential step towards successful cortical folding quantification in the developing fetal brain.

Segmentation of the cortical GM is very challenging in fetal brain MRI, even with reconstructed motion-free HR images, primarily because a significant partial volume effect is still present in cortical GM, which is often only 1 or 2 voxels thick, and which creates ambiguous boundaries with the adjacent cerebrospinal fluid and white matter tissue. To date, few studies have

Chapter 3. Quantification of Fetal Cortical Folding using Super-Resolution MRI Reconstruction and FreeSurfer

extracted the cerebral cortex and quantified its folding in early development stage.

The authors in [1] proposed for the first time to reconstruct 3D cortical surfaces from MR images and to compute the global gyrification index to investigate fetal cortical folding patterns happening in the 25 to 35 GA range. Cortical GM was extracted using a traditional age-dependent atlas-based segmentation method followed by manual corrections for an accurate delineation. The authors in [2] proposed to model early folding in the normal fetal brain in the 20 to 28 GA range using morphometric analysis of the cortical plate. Cortical GM was segmented adopting the expectation-maximization with Markovian regularization (EM-MRF) framework [3] which uses a spatio-temporal probabilistic atlas as prior. Based on the same EM-MRF segmentation framework, the authors in [4] have contributed with a local approach where the local mean curvature of the inner cortical plate is computed to quantify folding in the 22 to 25.5 GA range. Recently, the authors in [5] presented a completely automatic image processing framework for successful quantification of cortical folding patterns over a wide GA range (22 to 39 weeks) involving HR image reconstruction, extraction of the cortical surface and computation of six different curvature measures. The EM-MRF framework was also adopted in this work to extract the cortical GM but an additional second order MRF penalization term was introduced for addressing the partial volume problem at cortical boundaries, essential in late gestational fetal brain with complex cortical structures. It was subsequently extended to the construction of a spatio-temporal cortical surface atlas [6]. In all existing works, cortical surfaces have been reconstructed using their own designed method based either on spherical-mesh deformation algorithms [1, 5, 6] or using topology-preserving marching cubes algorithms [2, 4].

In this chapter, I will take advantage of the completely automated HR image reconstruction pipeline, presented in Chapter 2, and I will investigate the feasibility of designing a completely automatic image processing pipeline for in vivo prenatal cortical folding quantification. For this purpose, I propose as a first step to use the age-specific multi-atlas-based brain tissue segmentation method, which has shown to capture well anatomic variability in severe forms of ventriculomegaly, to segment the brain into different tissue types which can be then used to create the WM volume. As a second step, I use FreeSurfer (<http://surfer.nmr.mgh.harvard.edu>), an open-source brain imaging software, widely adopted in the neuroscientist community for analysis and visualization of adult brain MRI, for the analysis of in-vivo fetal cortical folding from MR images reconstructed with the proposed automated pipeline. This approach explore the feasibility of taking advantages of the existing set of automated tools provided of the adult brain's cortical surface to 1) extract fetal cortical surfaces, 2) to compute brain maturation indicators, and 3) to render the results. Preliminary results on three fetuses in the 27 to 32 GA range will show that quality of the images reconstructed with the proposed pipeline is now adapted to subsequent tissue segmentation and cortical folding quantification tasks.

3.2 Contributions

This work was initiated during a short visit at the Cognitive and Systems Neuroscience Laboratory, Stanford, USA. My personal contributions are the following:

- I collected clinical fetal scans at the Boston Children's Hospital and reconstructed the HR image using the automated pipeline that I designed.
- I familiarized with the multi-atlas multi-shape segmentation algorithm, performed tissue segmentation of the reconstructed images, and formed the WM volume by combining the tissue labels lying inside.
- I investigated and identified, in collaboration with Dr. Marie Schaer, a FreeSurfer expert in cortical folding quantification, which parts of the FreeSurfer recon-all pipeline should be used and how they be adapted when applied to fetal brain MRI to extract cortical surfaces and compute folding features.
- I extracted cortical (inner, pial, outer-pial) surfaces and computed the curvature maps as well as the local gyrification index.
- I rendered the results using the FreeSurfer tksurfer visualization tool.
- A generic script has been provided to facilitate reproducibility of this work.

3.3 Methods

The proposed image processing framework (Figure 3.1) consists of combining: (1) automatic reconstruction of a HR motion-corrected image where fetal brain is isolated (Steps 1.1 and 1.2 in Figure 3.1), (2) automatic estimation of the white matter (WM) volume (Steps 2.1 and 2.2 in Figure 3.1), and (3) automatic extraction of the cortical surface (Step 3.1 in Figure 3.1) and computation of folding measures (Step 3.2 in Figure 3.1).

Automated image reconstruction The HR image is reconstructed using an entirely automated reconstruction pipeline. It involves brain localization and extraction, intensity standardization, motion estimation, brain mask refinement, detailed in Chapter 2, and the efficient TV SR reconstruction, detailed in Chapter 1. In addition, the active surface algorithm used to extract the pial surface was designed for adult brain T1W MR images and is looking for a bright region as a stopping criteria of surface evolution which is not observed in fetal MRI. As a result, a white halo (width of 2 voxels) is added around the brain, which reduces the risk of infinite evolution of the pial surface into the background. This creates the initial MR image that will be used by FreeSurfer (referred as T1.mgz after data preparation and format conversion).

Chapter 3. Quantification of Fetal Cortical Folding using Super-Resolution MRI Reconstruction and FreeSurfer

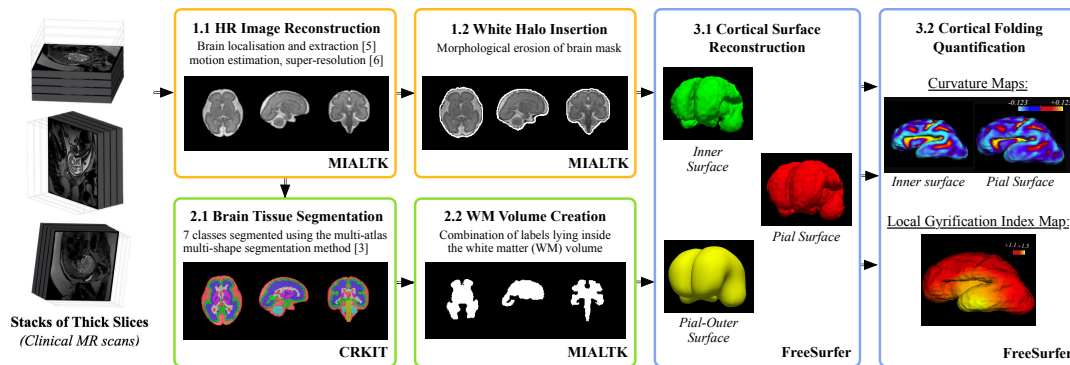


Figure 3.1 – Image processing pipeline for in-vivo fetal cortical folding quantification taking advantage of the set of tools provided by FreeSurfer. Automatic high-resolution image reconstruction, insertion of the white halo, automatic brain tissue segmentation and creation of the white matter volume are implemented in C++ with the help of the ITK library.

Brain tissue segmentation Seven classes of tissue are segmented in the HR image using the multi-atlas multi-shape segmentation method [7]. In contrast to the EM-MRF framework which incorporates prior information from a spatio-temporal probabilistic atlas, this approach is based on the recent probabilistic shape optimization framework [8] which incorporates shape model of structures, regional intensity values and prior information from multi-atlas segmentations. The multi-atlas segmentation consists of using multiple atlases, applying a pairwise registration between the target image and each atlas followed by label propagation, and the multi-atlas segmentation is obtained using a robust label fusion strategy. The STAPLE algorithm is used for robust label fusion which gives less weight to less reliable propagated labels from registered atlases than those from more reliable ones. Multi-atlas approach have been supported by a large number of works in the literature to allow an increase in segmentation accuracy and robustness when compared to a single-best-atlas approach [9]. However, the success of multi-atlas approaches is strongly influenced by the accuracy of inter-subject registration, and thus may not be enough accurate in the presence of large anatomical variations, even while a robust voting is adopted. Using shape models and intensity-based information from multi-atlas segmentation as priors in the shape optimization framework has shown to achieve robust and accurate segmentation of the ventricles in severe forms of ventriculomegaly where there exist a large anatomical variability. After brain tissue segmentation, the initial WM volume used by FreeSurfer is created (referred as `wm.mgz` after data preparation and format conversion), by combining all tissue labels lying inside it.

Cortical folding quantification The whole sequence of instructions for preparing data and performing surface extraction and cortical folding quantification using FreeSurfer is detailed in a generic script (Figure 3.2). Data preparation involves creation of the subject directory (routine `mksubdirs`), data conversion to “MGZ” format (routine `mri_convert`), creation of additional input images required by FreeSurfer, computation of the sagittal and transversal

cutting planes based on the corpus callosum and pons coordinates and generation of two solid masses of connected voxels using a connected components analysis, each representing a single cortical hemisphere (routine “`mri_fill`”). This is followed by the execution of specific parts of the FreeSurfer “`recon-all`” pipeline intended to extract the cortical surfaces and compute the folding measures. First, a two-pass procedure is performed to extract smooth inner and pial cortical surfaces using surface triangle-based tessellation (flag “`-tessellate`”) of the two cortical masses followed by a deformable surface algorithm guided by local MRI intensity values (flags “`-smooth1`” and “`-smooth2`”), interleaved by surface inflation (flag “`-inflate1`”), quasi-homeomorphic spherical transformation (flag “`-qsphere`”), topological defects removal (flag “`-fix`”) and creation of the new topology-corrected tessellation (flag “`-white`”). The resulting smooth inner and pial surfaces are then inflated (flag “`-inflate2`”), necessary in order to then perform a spherical transformation (flag “`-sphere`”) and register the transformed surface to the spherical atlas (flag “`-surfreg`”). The step “`-jacobian_white`” computes the amount of distortion encountered by the white surface during the registration to the spherical atlas (Step “`-surfreg`”). The step “`-avgcurv`” resamples the average curvature maps from the atlas to that of the subject. Finally, all cortical surfaces are generated (routine “`mris_make_surfaces`”) and the local gyrification index is computed at each point of the inner and pial surfaces (recon-all called with the flag “`-localGI`” only).

3.4 Results

We process three fetuses with normal brain, denoted as C1, C2 and C3. Acquisitions were performed at the Boston Children’s Hospital respectively during the 27th (C1), the 30th (C2) and the 32th (C3) week of gestation. A Siemens Skyra 3T MR scanner with HASTE sequences (TE/TR = 121/1600ms) was used to acquire 5 (C1), 6 (C2) and 6 (C3) 3D orthogonal stacks of thick 2D T2w MR images (1.2x1.2x2mm³), with at least 1 stack per anatomical direction. Figure 3.3 presents quantitative results obtained with the proposed image processing pipeline, with extracted surfaces, curvature and local gyrification measures. The atlas dataset used in this work is composed by a set of age-specific MR template images in the 21 to 37 GA range [?] and a set of 80 reconstructed HR images of subjects. Templates and reconstructed images in the same GA range of the target fetal brain were used in atlas-based segmentation. Manual correction of the original WM volume were not performed in this study but would be required for an accurate quantification, which was beyond the scope of this work.

3.5 Discussion

Figure 3.3 shows that the quality of reconstructed HR images has enabled brain tissue segmentation and cortical folding quantification tasks. Despite significant differences in size, shape, and complexity of the fetal brain and adult brain, the use of active surface deformation algorithms such as the one provided by FreeSurfer seems to be helpful in characterizing fetal cortical surface features. Thanks to the curvature maps, we can well observe sulci (areas with

Chapter 3. Quantification of Fetal Cortical Folding using Super-Resolution MRI Reconstruction and FreeSurfer

```
1 #!/bin/bash
3 ## Go into the FreeSurfer "subjects" directory.
  cd $SUBJECTS_DIR
5
7 ## Creation of a new subject directory (XXX).
  mkdir XXX
9
11 ## Go into the subject directory.
  cd XXX
13
15 ## Copy your HR reconstructed image (with the white halo) and its the corresponding WM
  volume image into the "orig" folder.
17 cp "YOUR_HR_IMAGE_WITH_HALO_FULL_PATH" "orig/HR_halo_image.nii"
  cp "YOUR_WHITE_MATTER_VOLUME_IMAGE_FULL_PATH" "orig/wm.nii"
19
21 ## Convert images in the FreeSurfer "MGZ" format. Flag "-cm" is very important for the
  WM volume image; if not set, the "mri_fill" routine will fail.
23 mri_convert orig/HR_halo_image.nii T1.mgz
  mri_convert -cm orig/wm.nii wm.mgz
25
27 ## Prepare the input images required by FreeSurfer routines (brain.mgz, norm.mgz, bain.
  finalsurfs.mgz).
29 cp T1.mgz brain.mgz
  cp T1.mgz norm.mgz
31 cp brain.mgz brain.finalsurfs.mgz
33
35 ## Create the subcortical mass from which the "orig" surface is built. You need here to
  provide the voxel coordinates of both the corpus callosum and the pons. They can
  be identified using the "tkmedit" program.
37 mri_fill -PV 128 132 128 -CV 128 110 138 wm.mgz filled.mgz
39
41 ## Normalize the HR image
  mri_normalize T1.mgz brain.mgz
43
45 ## Estimate cortical surfaces and compute average curvatures.
  recon-all -tessellate -smooth1 -inflate1 -qsphere -fix -noaseg -white -smooth2 -
  inflate2 -sphere -surfreg -jacobian_white -avgcurv -s XXX
47
49 ## Create cortical surfaces
  mris_make_surfaces -white NOWRITE -mgz -T1 brain -noaparc -noasef XXX lh
  mris_make_surfaces -white NOWRITE -mgz -T1 brain -noaparc -noasef XXX rh
51
53 ## Compute global/local gyrification indexes (GI/LGI)
  recon-all -no-isrunning -s XXX -localGI
```

Figure 3.2 – Generic bash script that uses FreeSurfer to extract cortical surfaces and quantify cortical folding.

positive value) and gyri (areas with negative value) of the cortex. Visual assessment confirms that cortical folding is more pronounced as the fetus is older. In addition, we can see in the LGI map that the Sylvian fissure corresponds to the region where the most important amount of cortex is buried within the sulcal folds in its surroundings. However, it can be noticed that

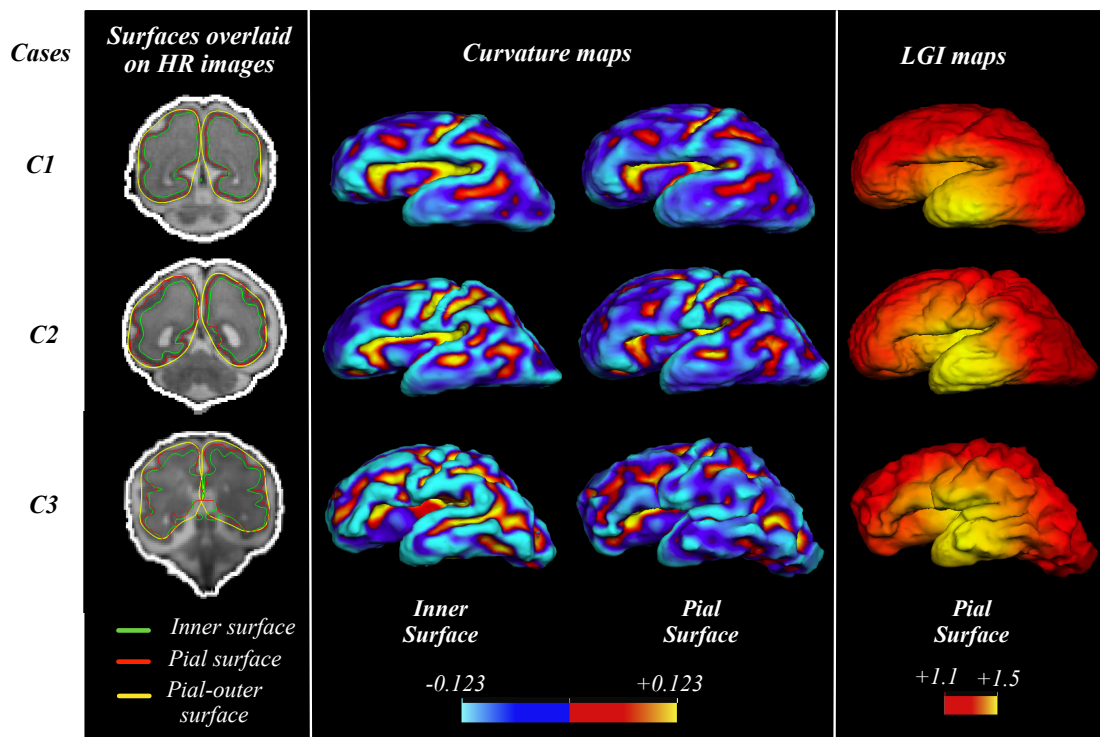


Figure 3.3 – Reconstructed cortical surfaces from fetal MRI and resulting quantitative maps of cortical folding for cases C1, C2 and C3 diagnosed with normal brains.

deformation towards the pial surface fails in some region because the algorithm originally developed for the adult brain is based on strong assumptions on image contrast, which differ between T1w adult and T2w fetal brain MRI, to guide it and stop it. The accuracy of the estimation of the cortical surfaces could also thus be increased by adapting the intensity-based prior to contrasts observed in fetal MRI. Moreover, manual correction of the original white matter volume were not performed in this study but would be required for an accurate quantification, which was beyond the scope of this work.

3.6 Conclusion

Results have shown the reconstruction of HR images using *state-of-the-art* TV SR, combined with *state-of-the-art* brain tissue segmentation and active surface deformation algorithms can provide meaningful indicators of brain maturation. However, the proposed approach has still few limitations. Firstly, a white halo has to be inserted around the fetal brain in the reconstructed high-resolution image to avoid the risk of infinite deformation of the pial surface as the surface deformation algorithm provided by FreeSurfer is looking apriori for a bright region to stop. Secondly, the quality of cortical surface reconstruction highly depends on the quality of prior automatic tissue segmentation. We have noticed the proposed pipeline performs relatively well on young fetus (around 24-28 GA) as cortex is a quite smooth structure

Chapter 3. Quantification of Fetal Cortical Folding using Super-Resolution MRI Reconstruction and FreeSurfer

that facilitates the success of cortex segmentation. Delineation of the inner cortical plate nonetheless may not be perfect which may require manual correction tasks in the white matter volume for accurate cortical quantification, as it was done in [1]. Working with older fetuses may involve more manual correction as cortical folding is more pronounced, which makes the segmentation more prone to errors (challenging). Future work can extend the database to study if a statistical group comparison could be also performed using FreeSurfer as it is commonly used in adult brain MRI studies.

Chapter 4 will present new methodological improvements of the reconstruction pipeline aiming at improving the segmentation and consequently the quantification, whose accuracy highly depend on the quality and resolution of the reconstructed image.

Acknowledgment

This work was supported in part by the Swiss National Science Foundation under Grant and PhD Mobility Grant SNSF-141283, the CIBM of Geneva-Lausanne Universities and EPFL, the Fondation Leenaards and Fondation Louis-Jeantet, and in part by the National Institutes of Health (NIH) grants R01EB0118988, R01EB013248, and R03DE22109.

Bibliography

- [1] C. Clouchoux, D. Kudelski, A. Gholipour, S. K. Warfield, S. Viseur, M. Bouyssi-Kobar, J.-L. Mari, A. C. Evans, A. J. Du Plessis, C. Limperopoulos, Quantitative in vivo MRI measurement of cortical development in the fetus, *Brain Structure and Function* 217 (1) (2012) 127–139.
- [2] P. A. Habas, J. A. Scott, A. Roosta, V. Rajagopalan, K. Kim, F. Rousseau, A. J. Barkovich, O. A. Glenn, C. Studholme, Early folding patterns and asymmetries of the normal human brain detected from in utero MRI, *Cerebral Cortex* 22 (1) (2012) 13–25.
- [3] P. A. Habas, K. Kim, F. Rousseau, O. A. Glenn, A. J. Barkovich, C. Studholme, Atlas-based segmentation of developing tissues in the human brain with quantitative validation in young fetuses, *Human Brain Mapping* 31 (9) (2010) 1348–1358.
- [4] J. A. Scott, P. A. Habas, V. Rajagopalan, K. Kim, A. J. Barkovich, O. A. Glenn, C. Studholme, Volumetric and surface-based 3D MRI analyses of fetal isolated mild ventriculomegaly, *Brain Structure and Function* 218 (3) (2013) 645–655.
- [5] R. Wright, V. Kyriakopoulou, C. Ledig, M. Rutherford, J. Hajnal, D. Rueckert, P. Aljabar, Automatic quantification of normal cortical folding patterns from fetal brain MRI, *NeuroImage* 91 (0) (2014) 21–32.
- [6] R. Wright, A. Makropoulos, V. Kyriakopoulou, P. Patkee, L. Koch, M. Rutherford, J. Hajnal, D. Rueckert, P. Aljabar, Construction of a fetal spatio-temporal cortical surface atlas from in utero MRI: Application of spectral surface matching, *NeuroImage* 120 (2015) 467 – 480.
- [7] A. Gholipour, A. Akhondi-Asl, J. A. Estroff, S. K. Warfield, Multi-atlas multi-shape segmentation of fetal brain MRI for volumetric and morphometric analysis of ventriculomegaly, *NeuroImage* 60 (3) (2012) 1819–1831.

4

Further Improvements

4.1 Introduction

The main contributions of this thesis have been developed with the aim of providing a more standardized and efficient motion-free HR reconstruction of fetal brain MR images, whose resolution-related problem was addressed in the slice-select dimension. In this chapter, we present new improvements with the aims to coherently correct slice-by-slice bias field intensity inhomogeneities, make the Total Variation algorithm robust to outliers, join segmentation and reconstruction processes, and reduce the partial volume effect, with the ultimate goal to allow a more accurate quantitative analysis.

Section 4.3 will present a new slice-by-slice bias field inhomogeneity correction method that takes advantage of the iterative reconstruction framework to estimate a coherent bias field in the reconstructed image which is then propagated to each slice of the scans. This approach allows the reconstruction of HR images free of smooth bias field intensity inhomogeneities. In addition, reconstructed images using the currently designed TV algorithm might be corrupted by non-Gaussian noise and the presence of outliers in the data emerging from possible intensity inhomogeneities and inaccurate slice motion estimation. Section 4.4 will present a new TV algorithm for super-resolution which incorporates the robust Huber norm in the fidelity term to improve its robustness to more generic outliers, as adopted by the authors in [1]. Section 4.5 will present a novel framework where reconstruction and segmentation are seen as joint processes. As segmentation strongly depends on the quality of the reconstruction, such an approach can produce images with enhanced edge information that will ultimately improve their segmentation. Finally, another remaining problem is the segmentation of thin structures, such as the cortical GM, which are still affected by a significant partial volume effect in the

in-plane dimensions which might mislead the capture of the boundaries between the interface of the tissues. Increasing the isotropic resolution of the HR image, e.g. addressing the spatial resolution increase in the through-plane dimension as well as in the in-plane dimensions, becomes very attractive to reduce this problem. Although there still exists a controversy in the MRI SR community and especially motivated by the works presented in [2, 3], Section 4.6 will investigate the feasibility of increasing the isotropic resolution by refining the mapping between voxels in the scans and voxels in the reconstructed HR image and taking advantage of sub-voxel motion that can occur prior to imaging.

For the sake of clarity, I recall here the contribution of this thesis presented in Chapter 2, the primal-dual TV formulation of the super-resolution problem:

$$\min_{\mathbf{X} \in S_X} \max_{\mathbf{P} \in S_Y} \underbrace{\langle \mathbf{D}\mathbf{X}, \mathbf{P} \rangle - F^*(\mathbf{P})}_{\|\mathbf{X}\|_{TV}} + \frac{\lambda}{2} \sum_{kl}^K \underbrace{\|\mathbf{H}_{kl}\mathbf{X} - \mathbf{X}_{kl}^{LR}\|}_{\mathbf{e}_{kl}}^2 + \underbrace{\delta_C(\mathbf{X})}_{\mathbf{X} \geq 0}. \quad (4.1)$$

where \mathbf{X} corresponds to the original primal variable (the image to be reconstructed) and \mathbf{P} corresponds to the dual variable introduced, F^* denotes the barrier function of the ℓ_∞ unit ball, that is $F^*(\mathbf{P}) = 0$ if $|\mathbf{P}_i| \leq 1$ for $1 \leq i \leq n$, otherwise $F^*(\mathbf{P}) = +\infty$ and $\delta_C(\mathbf{X})$ is a barrier function of the convex set $C := \{\mathbf{X} \geq 0\}$. This contribution will be extended in Sections 4.5, 4.4 and 4.6.

4.2 Contributions

In this chapter, I present new improvements aiming at providing better quality images for a more accurate quantitative analysis. The contributions consist of:

- The design and implementation of a new bias field correction method that can estimate a coherent bias field in the reconstructed image which is then used to correct the bias field in the original LR images taking advantage of the super-resolution framework. Such an approach has shown to be able to reconstruct a HR image with reduced artifacts and quasi free of bias field inhomogeneities.
- The design and implementation of a new robust TV algorithm based on the robust Huber norm where I preliminary show on simulated fetal data, where a number motion error residual have been introduced, that it can provide more robust reconstruction at higher peak-to-signal ratio.
- The design and implementation of a novel joint reconstruction-segmentation frame with a new segmentation-driven TV SR algorithm. Preliminary results show how discriminative segmentation included in the super-resolution model could potentially influence segmentation and how segmentation could potentially influence image contrast in an iterative reconstruction-segmentation setup.

4.3. Slice-by-slice intensity inhomogeneity correction from a globally-estimated bias field

- A last contribution is the redefinition of the SR formulation in order to address in-plane resolution improvement, where I preliminary compared the impact in the frequency domain with adopting super-resolution followed by interpolation and I preliminary show that segmentation and consecutive quantitative volumetry results are well influenced by the resolution.

4.3 Slice-by-slice intensity inhomogeneity correction from a globally-estimated bias field

4.3.1 Motivation

Bias field correction constitutes an important preprocessing step for subsequent image analysis tasks of MRI. The bias field is a low-frequency and smooth signal corrupting MR images due to inhomogeneities in the magnetic fields of the scanner. It reduces the high frequency content of the image and changes intensity values of voxels in the way the same tissue can follow different graylevel distribution across the image. It can degrade the performance of segmentation algorithms that use graylevel intensity values of the pixels in the processed image. During the last years, several approaches have been developed for correcting the non-uniform intensity caused by the bias field signal. The two most popular are the parametric bias field correction (PABIC) [4] and the improved nonparametric nonuniform intensity normalization (N4) algorithms [5]. The main difference between the two is: PABIC has to be supervised with an *a priori* knowledge on the tissue intensity class mean and standard deviation while N4 is fully automatic.

Bias field corruption is highly present in fetal MRI scans because of the distance of the fetal brain from the receiver coils, and even emphasized when SST2W imaging is performed at 3T. Moreover, intensity inconsistencies could affect the performance of motion estimation and reconstruction resulting in undesired artifacts in the reconstructed images, which reinforces the importance of bias field correction in fetal MRI reconstruction. Different solutions have been proposed in the literature to address this problem, either as a image preprocessing task [1, 6, 7] or integrated in the reconstruction framework [8].

In our previous works, it has been addressed as a preprocessing step where each scan was independently corrected using N4. N4 was initially performed in the whole scan volume (3D) (Chapter 1) and then a slice by slice (2D) correction was adopted which better took into account fetal motion (Chapter 2). Despite the last technique in combination with inter-slice mean shift correction and brain intensity histogram equalization has shown to make intensity more coherent over most all slices providing satisfactory reconstruction results, a global and smooth intensity bias field may still be present in the reconstructed image, which will affect the performance of further brain tissue segmentation tasks. This section will present a novel bias field correction method that takes advantage of the reconstruction framework to provide a reconstructed image free of smooth bias field inhomogeneities.

4.3.2 Method

The approach estimates using N4 a coherent and smooth bias field (step (IX) in Figure 4.1) from the reconstructed image, which is then propagated to each slice of the scans using the estimated motion and each slice is corrected (step (X) in Figure 4.1). N4 is employed as it requires no *a priori* knowledge and has shown to be relatively performant in a variety of imaging acquisition strategies. It assumes that the bias field has a multiplicative model where the formation of an MR image is:

$$\mathbf{X}(i) = \mathbf{U}^{HR}(i) \times \mathbf{I}^{HR}(i) + \mathbf{n}(i), \quad (4.2)$$

where \mathbf{X} is the intensity in the reconstructed image, \mathbf{I}^{HR} is the bias field inhomogeneity, \mathbf{U}^{HR} is the true intensity and \mathbf{n} is the noise. The bias field is estimated in the log space, making the model additive:

$$\begin{aligned} \log(\mathbf{X} - \mathbf{n}) &= \log(\mathbf{U}^{HR}) + \log(\mathbf{I}^{HR}), \\ \log(\mathbf{U}^{HR}) &= \log(\mathbf{X} - \mathbf{n}) - \log(\mathbf{I}^{HR}). \end{aligned} \quad (4.3)$$

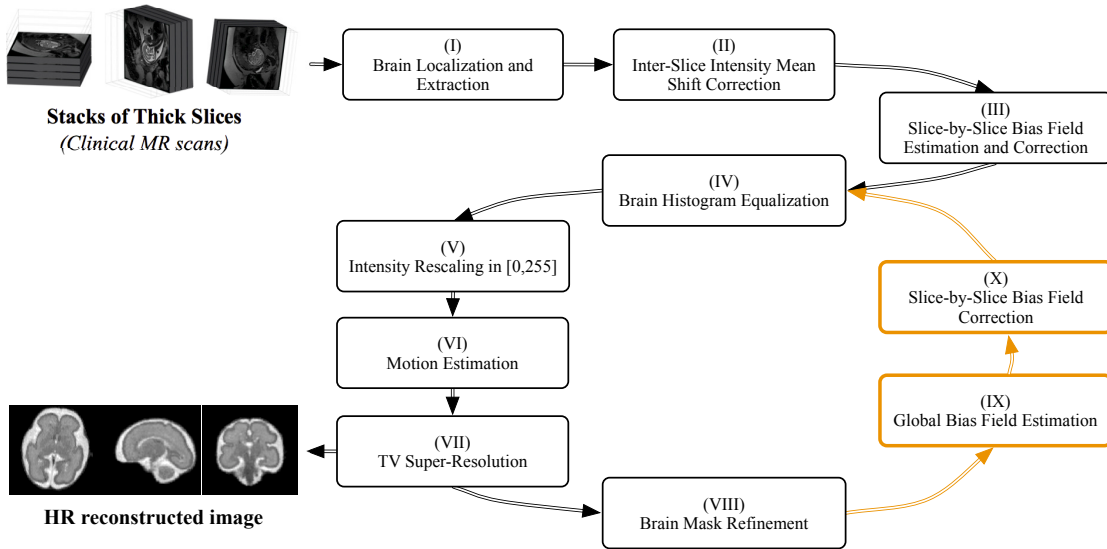


Figure 4.1 – Reconstruction pipeline for fetal MRI using the proposed bias field correction method. The approach takes advantage of the reconstruction framework to provide a reconstructed image free of smooth bias field inhomogeneities. New processes involved in the reconstruction pipeline are highlighted in red. Step (IX) estimates a coherent and smooth bias field from the image reconstructed at step (VII) using N4 [5], which is then propagated to each slice of the scans using the motion estimated at step (VI) and used to correct bias field inhomogeneity in each slice (Step (X)). Our solution is thus able to take into account inter-slice motion and to correct for the smooth bias field. Note that the previous independent slice-by-slice bias field correction is performed at the first loop (Step (III)) since the method is dependent on the preceding motion estimation and super-resolution steps.

4.3. Slice-by-slice intensity inhomogeneity correction from a globally-estimated bias field

The N4 method seeks iteratively the smooth multiplicative field that maximizes the high frequency content of the distribution of tissue intensity. Specifically, N4 performs a bias correction step on the corrected image from the previous iteration to estimate the residual bias field. As it is designed to converge such that the residual bias field tends to 0, the total bias field estimated at iteration n became the sum of the first n residual bias field. Once the bias field \mathbf{I}^{HR} is estimated from the reconstructed image, the bias field \mathbf{I}_{kl}^{LR} of each slice of the scans is generated through the propagation of \mathbf{I}^{HR} using the forward model of the super-resolution problem:

$$\mathbf{I}_{kl}^{LR} = \mathbf{H}_{kl}\mathbf{I}^{HR}, \quad (4.4)$$

and each slice \mathbf{Y}_{kl} is corrected from its bias field:

$$\mathbf{U}_{kl}^{LR}(i) = \mathbf{Y}_{kl}(i)/\mathbf{I}_{kl}^{LR}. \quad (4.5)$$

Therefore, the global bias field can be more coherently corrected slice-by-slice, accounting for possible inter-slice motions, which results in the reconstruction of images free of the smooth bias field. A proof of concept will be provided in the next section.

4.3.3 Results

To illustrate the improvement in reconstruction quality, we will show in this section the reconstruction results we obtained for one specific subject diagnosed with unilateral ventriculomegaly, illustrative of all. Acquisition was performed during the 26th week GA at Boston Children's Hospital, Boston, USA, using a 3T Siemens Skyra with a T2-weighted HASTE sequence (TE/TR = 116-119/1600ms). The dataset is formed by 6 orthogonal scans of thick slices, two per anatomical direction, with an anisotropic resolution of $1 \times 1 \times 2 \text{ mm}^3$. An HR image has been reconstructed using (1) the previous pipeline where independent slice-by-slice bias field estimation and correction were performed (see Chapter 2 for more details) and (2) the new pipeline integrating our coherent slice-by-slice bias field correction approach (Figure 4.1). Figure 4.2 shows the reconstruction results as well as the bias fields estimated using the two different approaches.

Visual inspection shows clearly that our method allows the estimation of a coherent bias field (c) which provides a reconstructed image quasi free of smooth intensity inhomogeneities. It can also be observed that the uncoherency of the bias field used previously introduces intensity artifacts that are removed with the new approach. This new pipeline will be adopted in the rest of the works presented in this chapter.

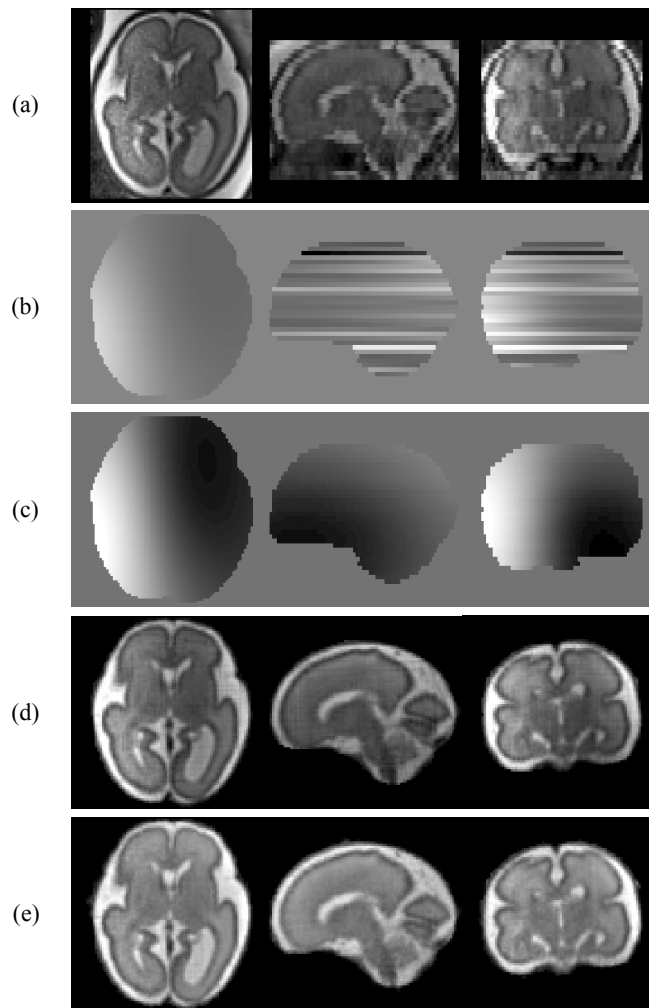


Figure 4.2 – Visual comparison of reconstruction results obtained using the previous and the improved slice-by-slice bias field correction methods. (a) presents one of the original acquired scan. (b) presents the bias field estimated independently slice by slice using the previous method. (c) presents the bias field estimated using the improved method and projected into the space of the scan. (d) presents the HR image reconstructed when using the previous bias field correction method. (e) presents the HR image reconstructed when using the improved method. It can be observed that the proposed method allow the estimation of a coherent bias field (c) which provides a reconstructed image quasi free of smooth intensity inhomogeneities. It can also be observed that the uncoherency of the bias field used previously introduces intensity artifacts that are removed with the new approach.

4.4 A robust Total Variation algorithm based on the Huber norm

4.4.1 Motivation

The currently designed TV algorithm assumes a Gaussian noise. However, possible intensity inhomogeneities can remain and inaccurate slice motion estimation can occur, which might

4.4. A robust Total Variation algorithm based on the Huber norm

modify the nature of the noise and might create the presence of outliers in the data. The current ℓ_2 -norm estimation adopted is not robust to such a circumstance since its corresponding influence function is not bounded. Different solutions have been proposed in the literature to tackle this problem, either by adopting a robust M-estimation SR formulation based on the Huber norm [1] or by integrating a probabilistic outlier model in the SR formulation [8]. Although the probabilistic approach has proven to be the most performant [8], the Huber norm in the robust M-estimation approach is convex and therefore, the same fast optimization scheme can be used, as presented in Chapter 1. This constitutes a great advantage over the probabilistic approach.

In this section, I will extend the robust M-estimation as described by the authors in [1] to our efficient TV SR algorithm in order to improve its robustness to outliers.

4.4.2 Method

In this section, I will present a new Total Variation SR algorithm where the ℓ_2 -norm of the error \mathbf{e}_{kl} in Equation (4.1) has been replaced by the robust Huber error norm function ρ_H defined as

$$\rho_H(e) = \begin{cases} e^2/2, & \text{if } |e| < \kappa \\ \kappa|e| - \kappa^2/2, & \text{if } |e| > \kappa \end{cases} \quad (4.6)$$

where κ is a tuning parameter. It allows the estimation to be close to the ℓ_2 -norm estimation when κ is large and to be close to the ℓ_1 -norm estimation when κ is small (Figure 4.3).

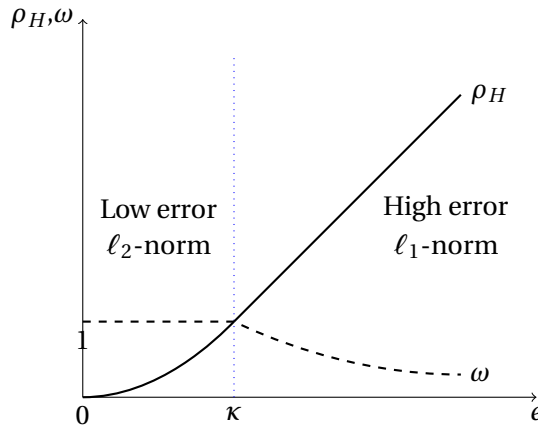


Figure 4.3 – Plots of the Huber error norm function and its associated weight function.

In this work, the parameter κ of the Huber norm is calculated based on the median absolute deviation (MAD) method [9] so that

$$\kappa = t \times K \times \text{median}(|\mathbf{e} - \text{median}(\mathbf{e})|), \quad (4.7)$$

where \mathbf{e} is the error vector, $K = 1.4826$ is a consistency constant, t is the number of MADs from the median the huber norm threshold κ is. Adopting the MAD allows a consistent estimator of the standard deviation of the errors. We set the value of t depending on the severity of motion in the scans. Based on [10, 11], we take $t = 3$ to be very conservative when a little/no motion occurs, $t = 2.5$ to be moderately conservative when more motion occurs, and $t = 2$ to be poorly conservative when severe motion occurs. When a significant number of observations are available, statistical methods are however considered to be more reliable for detecting and rejecting extreme outliers as compared to poorly tuned redescending influence functions [?].

By taking its associated weight function ω , defined as $\omega(e) = (1/e) * d\rho_H(e)/de$ (Figure 4.3), the primal-dual TV formulation of the super-resolution problem becomes

$$\min_{\mathbf{X} \in \mathcal{S}_X} \max_{\mathbf{P} \in \mathcal{S}_Y} \underbrace{\langle \mathbf{D}\mathbf{X}, \mathbf{P} \rangle - F^*(\mathbf{P})}_{\|\mathbf{X}\|_{TV}} + \frac{\lambda}{2} \sum_{kl} \|\mathbf{\Omega}_{kl}(\mathbf{e}_{kl})\|_2^2 + \underbrace{\delta_C(\mathbf{X})}_{\mathbf{X} \geq 0}, \quad (4.8)$$

where $\mathbf{\Omega}_{kl}$ is a weighting diagonal matrix with its i -th diagonal element defined by $\omega(\mathbf{e}_{kli})\omega(\mathbf{e}_{kl})$ where the weighting functions of the individual voxel error and the slice error are $\omega(\mathbf{e}_{kli}) = \min(1, \kappa_1/|\mathbf{e}_{kli}|)$ and $\omega(\mathbf{e}_{kl}) = \min(1, \kappa_2/\|\mathbf{e}_{kl}\|_2^2)$ respectively. It allows us to penalize high error values by giving them ℓ_2 -norm weights while giving to low error values ℓ_1 -norm weights (Figure 4.3). The new algorithm consists now in iterating

$$\mathbf{P}^{n+1} = \text{prox}_{\sigma^n F^*}(\mathbf{P}^n + \sigma^n \mathbf{D}\bar{\mathbf{X}}^n) \quad (4.9)$$

$$\mathbf{X}^{n+1} = \min_{\mathbf{X} \geq 0} \frac{\lambda}{2} \sum_{kl} \|\mathbf{\Omega}_{kl}(\mathbf{H}_{kl}\mathbf{X}^n - \mathbf{X}_{kl}^{LR})\|_2^2 + \frac{1}{2\tau^n} \|\mathbf{X} - \mathbf{X}^n - \tau^n \mathbf{D}^t \mathbf{P}^{n+1}\|^2 \quad (4.10)$$

$$\begin{aligned} \theta^{n+1} &= 1/\sqrt{1+2\rho\tau^n}, \quad \tau^{n+1} = \theta^{n+1}\tau^n, \\ \sigma^{n+1} &= \sigma^n/\theta^{n+1} \end{aligned} \quad (4.11)$$

$$\bar{\mathbf{X}}^{n+1} = \mathbf{X}^{n+1} + \theta^{n+1}(\mathbf{X}^{n+1} - \mathbf{X}^n) \quad (4.12)$$

where the Euler-Lagrange solution of Eq. (4.10) is $\lambda\tau^n(\mathbf{\Omega}\mathbf{X} - \mathbf{X}^{LR}) + \mathbf{X} - \mathbf{W} = 0$ where $\mathbf{\Omega} := \sum_{kl} (\mathbf{\Omega}_{kl}\mathbf{H}_{kl})^t \mathbf{\Omega}_{kl}\mathbf{H}_{kl}$ and $\mathbf{X}^{LR} := \sum_{kl} (\mathbf{\Omega}_{kl}\mathbf{H}_{kl})^t \mathbf{X}_k^{LR}$ (note that $\mathbf{\Omega}$ and \mathbf{X}^{LR} should be computed at each iteration) and the iterative semi-implicit scheme is defined as $\mathbf{X}^{l+1} = \mathcal{P}_C(\mathbf{X}^l - \Delta t \lambda \tau^n (\mathbf{\Omega}\mathbf{X}^l - \mathbf{X}^{LR}) + \Delta t \mathbf{W}) / (1 + \Delta t)$ where \mathcal{P}_C is the projection operator onto the set $\mathbf{X} \geq 0$ and $\Delta t = 0.1$ in all experiments.

4.4.3 Results

To evaluate the robustness of our algorithm, we used simulated fetal data where controlled slice motion estimation errors were introduced. A T2-weighted TurboFLASH image of a mature newborn was used to simulate fetal brain MRIs, as in [1, 8]. The image was acquired on a 3T Siemens Tim Trio scanner ($TR/TE = 4000/3.7ms$, with $1.2mm$ slice thickness and

4.5. A segmentation-driven Total Variation super-resolution algorithm

$0.78mm^2$ in-plane resolution. We consider the isotropic HR image as the original image that was bias field corrected [5] and isotropically interpolated to a resolution of $1mm$ using B-Splines. Six LR images, two per acquisition direction, with $1mm^2$ in-plane resolution and $3mm$ slice thickness, were simulated from the isotropic HR image by applying downsampling and blurring operations. Shifts of $1mm$ were also introduced in images with similar acquisition direction.

We assess the performance of our algorithm w.r.t. the residual motion error by randomly affecting 1/5 (modest), 2/5 (moderate), 3/5 (high) of the slices in each LR images. The amounts of residual motion errors were randomly added to both translation and rotation transform parameters, similarly to [12] and following [1, 6, 13]. Translation errors were selected in $[-5mm, 5mm]$ and rotation errors were selected in $[-10^\circ, 10^\circ]$. The reconstruction quality was evaluated with the Peak-Signal-To-Noise Ratio (PSNR). We used as reference the image reconstructed using the original TV algorithm where no residual motion errors were introduced. Results are presented in Figure 4.4.

We observe that the reconstruction quality always degrades independently of the data fidelity term adopted as the number of slices affected by error motion residual is important. A robust norm used in the data fidelity term has shown to be able to provide reconstructed images with better quality (higher PSNR) a reduced amount of artifacts coming from outliers. In addition, the Huber norm of the new algorithm is less sensitive to residual errors of the motion estimation than the previous ℓ_2 -norm. Finally, we observe that the Huber-norm threshold providing the best restoration decreases as the number of affected slices increases. This confirms that the Huber norm threshold should be set with respect to the severity of motion in the scans. The new robust TV algorithm will be adopted in the rest of this chapter.

4.5 A segmentation-driven Total Variation super-resolution algorithm

4.5.1 Motivation

Medical image segmentation and reconstruction have traditionally been regarded as separate processes, even though segmentation performance directly depends on the quality the image reconstructed. Adopting an integrated reconstruction-segmentation process can provide a more efficient and accurate segmentation solution. A joint reconstruction-segmentation framework has been recently proposed by the authors in [14] that combines reconstruction of MR images from undersampled k-space (known as compressed-sensing) with segmentation based on Gaussian mixture models (GMM). Results have demonstrated that the incorporation of the GMM term in the reconstruction process provides a segmentation that degrades less with increasing undersampling compared to separated reconstruction and segmentation.

In this section, we extend this framework to perform for the first time a joint segmentation-reconstruction process in fetal brain MRI data. In contrast to the initial framework where reconstruction was addressing a compressed-sensing problem (reconstruction of anatomical

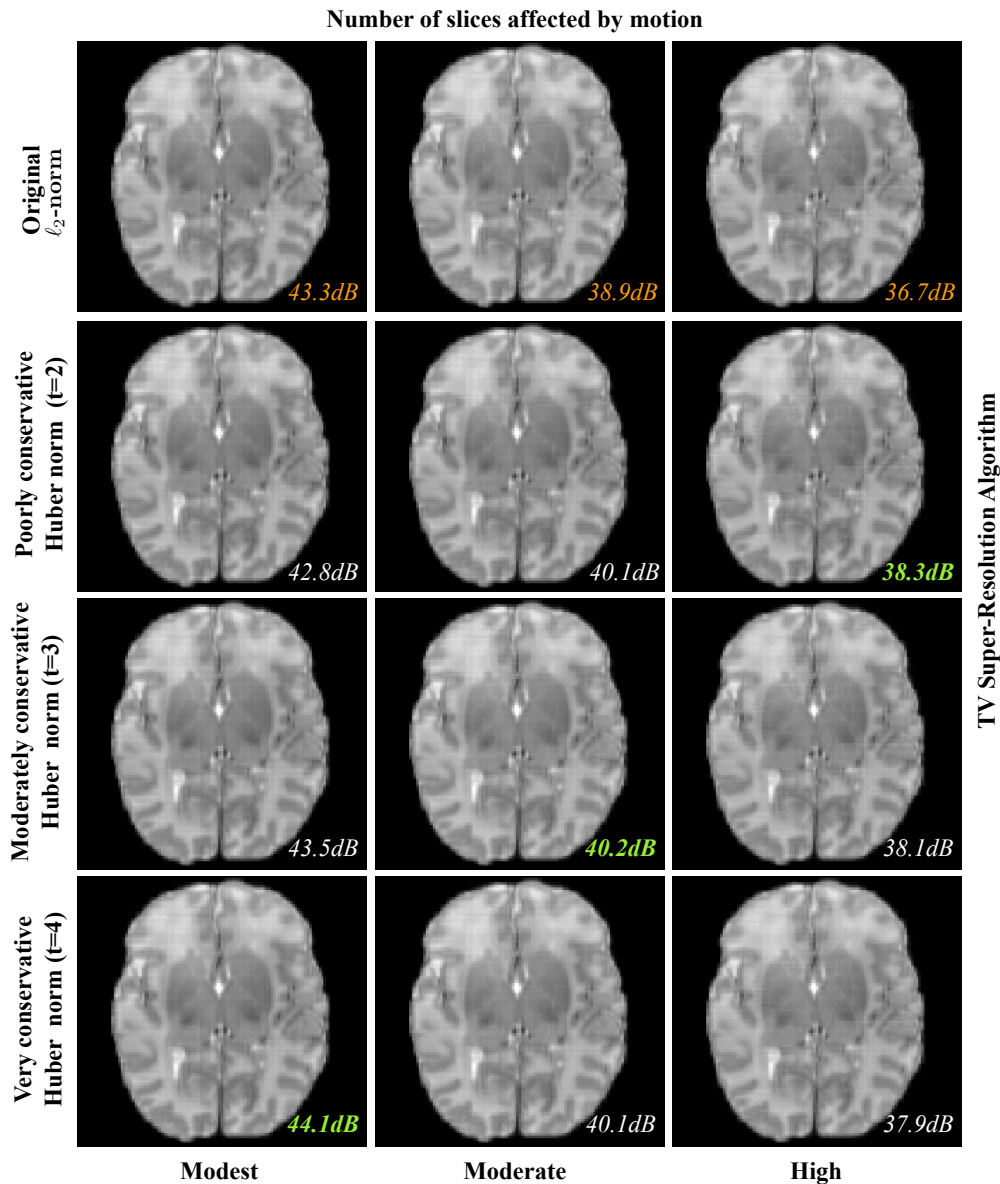


Figure 4.4 – Comparison of Total Variation Super-Resolution algorithms using in the data fidelity term the ℓ_2 -norm (first row), a poorly conservative Huber norm (second row), a moderately conservative Huber norm (third row), and a very conservative Huber norm (fourth row), for 1/5 (Modest), 2/5 (Moderate), 3/5 (High) of slices affected by error motion residual. Their PSNR measures with respect to the image reconstructed which no introduced residual motion error are reported in their bottom-right corner. We can that a robust norm adopted in the presence of outliers due to inaccurate slice motion estimation is able to provide reconstructed images with higher PSNR. This shows that our algorithm is less sensitive to such outliers than the previous ℓ_2 -norm-based algorithm.

images from undersampled k-space), in our framework, reconstruction is addressing the super-resolution problem in the spatial domain.

4.5.2 Methods

Our joint segmentation-reconstruction framework for fetal brain MRI has involved the design and implementation of a new TV SR algorithm which incorporates an additional discriminative GMM term as prior information. For joint segmentation-reconstruction purpose, an image processing pipeline has been designed. The image processing pipeline and each image processing step will be described in this section.

Image processing pipeline Figure 4.5 shows the image processing pipeline designed to jointly perform reconstruction and segmentation. It is composed of (1) brain tissue segmentation, (2) estimation of GMM parameters, and (3) segmentation-driven TV super-resolution, repeated until the segmentation reaches convergence. It allows the reconstruction to evolve conjointly with segmentation ultimately improving the segmentation of the reconstructed image.

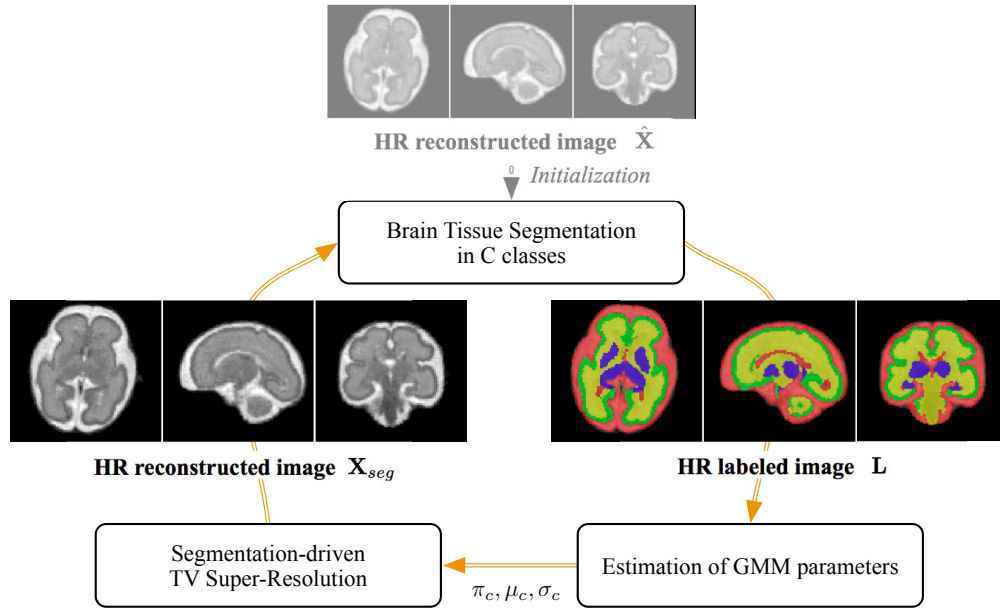


Figure 4.5 – Image processing pipeline for joint reconstruction-segmentation.

Segmentation-driven Total Variation SR algorithm Let each voxel $\mathbf{X}_{seg}(i)$ in the segmentation-driven reconstructed image \mathbf{X}_{seg} be expressed by a mixture of C Gaussians such as $P(\mathbf{X}_{seg}(i)) = \sum_{c=1}^C \pi_c(i) \mathcal{N}(\mathbf{X}_{seg}(i) | \mu_c, \sigma_c)$ where μ, σ and $\pi(i)$ are the means, standard deviations and local (voxel-wise) mixture weightings of the Gaussians. The segmentation-driven super-resolution formulates reconstruction imposing a model on the data that weights the modified TV energy

Chapter 4. Further Improvements

(Equation 4.8) and a GMM representation:

$$\min_{\mathbf{X}_{seg} \in S_X} \max_{\mathbf{P} \in S_Y} \underbrace{(\mathbf{D}\mathbf{X}_{seg}, \mathbf{P}) - F^*(\mathbf{P})}_{\|\mathbf{X}_{seg}\|_{TV}} + \frac{\lambda}{2} \sum_{kl} \|\mathbf{\Omega}_{kl}(\mathbf{e}_{kl})\|^2 + \underbrace{\delta_C(\mathbf{X}_{seg})}_{\mathbf{X}_{seg} \geq 0} + \underbrace{\beta \ln P(\mathbf{X}_{seg} | \boldsymbol{\mu}, \boldsymbol{\sigma}, \boldsymbol{\pi})}_{\text{GMM}}, \quad (4.13)$$

where

$$\ln P(\mathbf{X}_{seg} | \boldsymbol{\mu}, \boldsymbol{\sigma}, \boldsymbol{\pi}) = \sum_{i=1}^N \ln \left(\sum_{c=1}^C \pi_c(i) \mathcal{N}(\mathbf{X}_{seg}(i) | \boldsymbol{\mu}_c, \boldsymbol{\sigma}_c) \right) \quad (4.14)$$

which corresponds to summing over every voxel i the logarithm of the value of the mixture of Gaussians. If $\beta = 0$, the problem is the same as in Equation (4.8) and is purely reconstructive as the GMM model is not used. For $\beta > 0$, the reconstructed intensities need to be consistent with the GMM emerging as a by-product of the reconstruction. The larger the penalisation of this term is, the closer intensities are to the means of Gaussians, so effectively it homogenises intensities within a region and reduces the number of intensities sitting around the boundaries of two regions. At the extreme $\beta \rightarrow \infty$, each pixel intensity is set to the mean of the Gaussian that is the most likely to have generated it. Our new algorithm consists now in iterating

$$\mathbf{P}^{n+1} = \text{prox}_{\sigma^n F^*}(\mathbf{P}^n + \sigma^n \mathbf{D}\bar{\mathbf{X}}_{seg}^n) \quad (4.15)$$

$$\mathbf{X}_{seg}^{n+1} = \min_{\mathbf{X}_{seg} \geq 0} \frac{\lambda}{2} \sum_{kl} \|\mathbf{\Omega}_{kl}^n(\mathbf{H}_{kl}\mathbf{X}_{seg}^n - \mathbf{X}_{kl}^{LR})\|^2 + \frac{1}{2\tau^n} \|\mathbf{X}_{seg} - \mathbf{X}_{seg}^n - \tau^n \mathbf{D}^t \mathbf{P}^{n+1}\|^2 + \beta \ln P(\mathbf{X}_{seg}^n | \boldsymbol{\mu}, \boldsymbol{\sigma}, \boldsymbol{\pi}) \quad (4.16)$$

$$\theta^{n+1} = 1/\sqrt{1+2\rho\tau^n}, \quad \tau^{n+1} = \theta^{n+1}\tau^n, \quad \sigma^{n+1} = \sigma^n/\theta^{n+1} \quad (4.17)$$

$$\bar{\mathbf{X}}_{seg}^{n+1} = \mathbf{X}_{seg}^{n+1} + \theta^{n+1}(\mathbf{X}_{seg}^{n+1} - \mathbf{X}_{seg}^n) \quad (4.18)$$

where the Euler-Lagrange solution of the modified least-square problem Eq. (4.16) is $\lambda\tau^n(\mathbf{\Omega}\mathbf{X}_{seg} - \mathbf{X}^{LR}) + \beta\tau^n\mathbf{GMM} + \mathbf{X}_{seg} - \mathbf{W} = 0$ where the i -th element of GMM is defined as $\mathbf{GMM}_i = \frac{d \ln P(\mathbf{X}_{seg}^n | \boldsymbol{\mu}, \boldsymbol{\sigma}, \boldsymbol{\pi})}{d\mathbf{X}_{seg}(i)}$ is defined as

$$\mathbf{GMM}(i) = \frac{\sum_c \frac{\pi_c(i)(\boldsymbol{\mu}_c - \mathbf{X}_{seg}(i))}{\sigma_c} \mathcal{N}(\mathbf{X}_{seg}(i) | \boldsymbol{\mu}_c, \boldsymbol{\sigma}_c)}{\sum_c \pi_c(i) \mathcal{N}(\mathbf{X}_{seg}(i) | \boldsymbol{\mu}_c, \boldsymbol{\sigma}_c)} \quad (4.19)$$

and the iterative semi-implicit scheme is defined as $\mathbf{X}_{seg}^{l+1} = \mathcal{P}_C(\mathbf{X}_{seg}^l - \Delta t \lambda \tau^n (\mathbf{\Omega}\mathbf{X}_{seg}^l - \mathbf{X}_{seg}^{LR}) - \Delta t \beta \tau^n \mathbf{GMM} + \Delta t \mathbf{W}) / (1 + \Delta t)$ where \mathcal{P}_C is the projection operator onto the set $\mathbf{X}_{seg} \geq 0$ and $\Delta t = 0.1$ in all experiments. To adopt global weights, we only have to take $\pi_c(i) = \pi_c$, i.e., the weights of each class c are constant over all voxels of \mathbf{X}_{seg} .

4.5. A segmentation-driven Total Variation super-resolution algorithm

Gaussian parameter estimation Gaussian parameters π, μ, σ can be estimated from a labeled image coming from any type of segmentation methods. In this work, five classes of tissues or structures have been automatically segmented using the multi-atlas multi-shape segmentation method [15]. They consist of WM, cortical GM (GM1), central nervous system (GM2), ventricles (V) and pericerebral CSF (CSF). The mean and standard deviations are estimated from the voxel population of each class. The weight of each voxel is computed as the proportion of voxels of each class within a patch-neighborhood patch (Figure ??). This approach allows us to describe (1) voxels whose patches remain completely inside a tissue as a unique graylevel intensity Gaussian distribution describing the tissue, and (2) voxels at tissue interface as a mixture of graylevel intensity Gaussian distributions. It has therefore the advantage to incorporate prior information about partial voluming in the reconstruction process.

4.5.3 Results

In this section, we will investigate for the first time the effect of reconstruction on segmentation and vice versa on small clinical fetal dataset. Three fetuses were processed: C1 and C2 were normal brains, and C3 was diagnosed with an unilateral ventriculomegaly. Acquisitions were performed at the Boston Children’s Hospital respectively during the 27th (C1), the 30th (C2) and the 32th (C3) week of gestation (GA). A Siemens Skyra 3T MR scanner with HASTE sequences (TE/TR = 121/1600ms) was used to acquire 5 (C1), 6 (C2) and 6 (C3) 3D orthogonal stacks of thick 2D T2w MR images ($1 \times 1 \times 2mm^3$), with at least 1 stack per anatomical direction. A very conservative Huber norm threshold ($t = 4$) was selected as scans were modestly affected by motion. For each case, a first HR image was reconstructed using the improved reconstruction pipeline (Figure 4.1). Then, the joint reconstruction-segmentation pipeline, as described in the last section, was adopted.

Segmentation of CSF, GM1, GM2, V, and WM was performed using the multi-atlas multi-shape segmentation approach [15]. The atlas dataset used in this work is composed by a set of age-specific MR template images in the 21 to 37 GA range [16]. Templates and reconstructed images in the same GA range of the target fetal brain were used in atlas-based segmentation. Segmentation-driven image reconstruction was performed using the proposed TV algorithm using different contribution weight β of the GMMs ($\beta = [0.3, 0.5, 1, 5]$) in the reconstruction process. Figure 4.6 shows the reconstruction results. A two-tailed Wilcoxon signed-rank test is used for evaluating the statistical significance of the differences in estimated volumetry (# of samples = 12, significance level = 0.05).

To quantitatively evaluate the impact of the segmentation on the contrast of the reconstructed images, we compute the brain histogram spread, a metric proposed in [17], based on the shape of the histogram able to distinguish between the images having different contrast level. The histogram spread (HS) of an image X is the ratio between the quartile distance and the

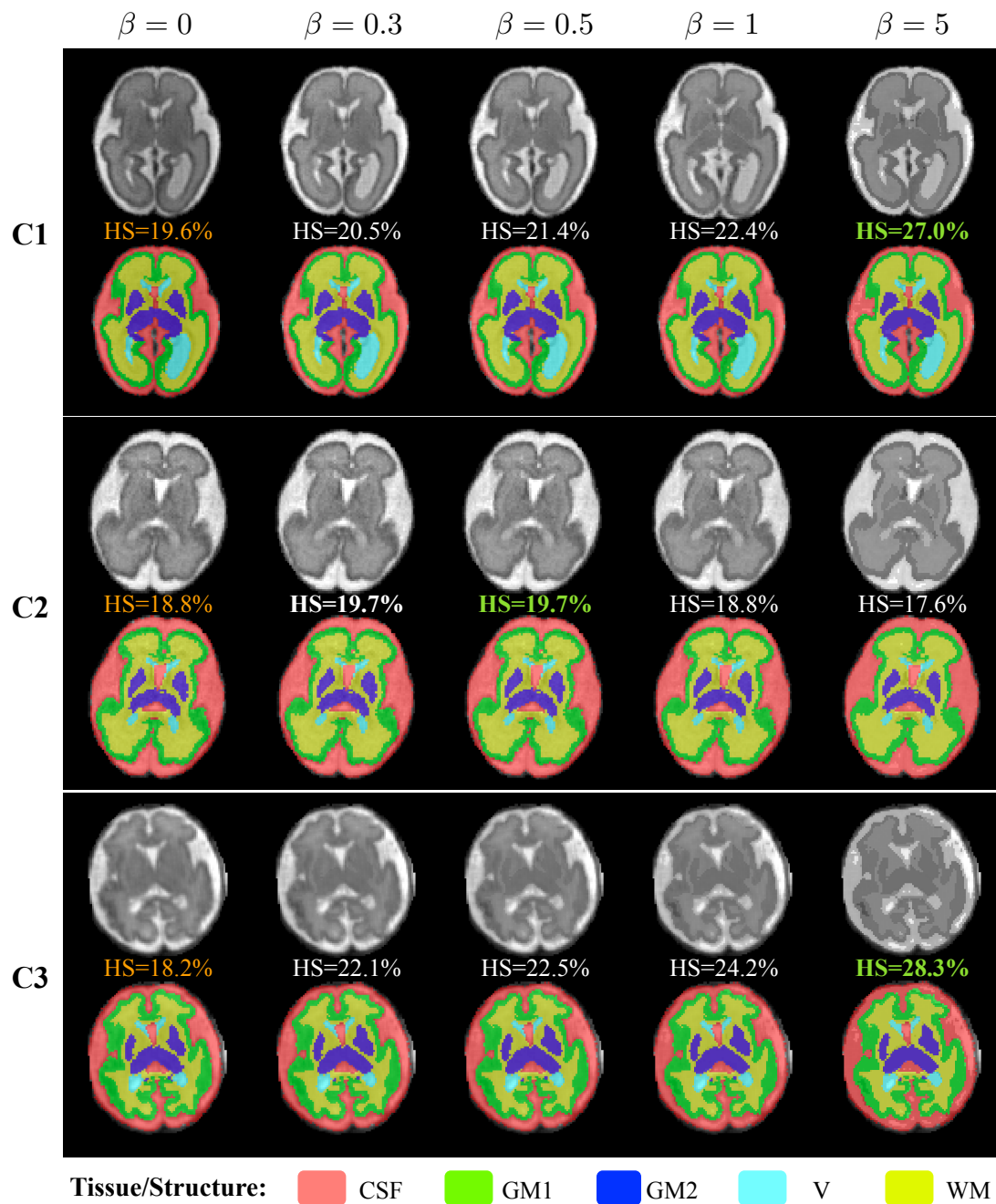


Figure 4.6 – Reconstruction and segmentation results for cases C1 (first and second rows), C2 (third and fourth rows), and C3 (fifth and sixth rows), when using our joint reconstruction-segmentation pipeline for a varying segmentation (GMM) contribution weight $\beta = [0.3, 0.5, 1, 5]$ in the super-resolution process. The first row illustrates reconstructed images and their segmentations which correspond to the initial images reconstructed before segmentation-reconstruction. The contrast in the image is evaluated using the histogram spread metric, as suggested by [17], and shown below each reconstructed image.

4.5. A segmentation-driven Total Variation super-resolution algorithm

range of the histogram

$$HS = \frac{Q3 - Q1}{\max(X) - \min(X)}, \quad (4.20)$$

where Q3 and Q1 corresponds respectively to the 3rd and 1st quartile of the histogram. A higher HS means a higher contrast. Results are reported below each reconstructed image in Figure 4.6. A second segmentation of CSF, GM1, GM2, V, and WM was performed using the images reconstructed with $\beta = [0.3, 0.5, 1, 5]$.

To quantitatively evaluate the impact of reconstruction on segmentation and further quantitative analysis, we compute the volumes of each label before and after segmentation-driven reconstruction for $\beta = [0.3, 0.5, 1, 5]$. Figure 4.6 shows the segmentation results. Volumetry results are reported in Figure 4.7. Differences were found statistically significant for GM1 ($p = 0.011$), GM2 ($p = 0.004$), V ($p = 0.004$), and WM ($p = 0.015$), except for CSF ($p = 0.478$).

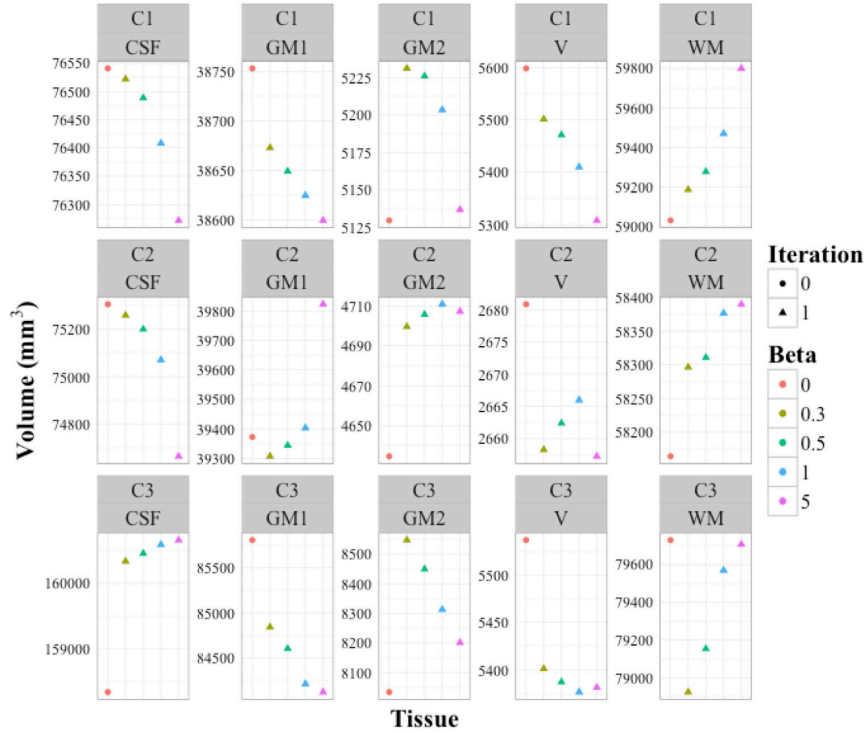


Figure 4.7 – Impact of segmentation-driven reconstruction on further automatic volumetric analysis of pericerebral CSF (CSF), cortical gray matter (GM1), central nervous system (GM2), ventricles (V), and white matter (WM). We can clearly see differences in volumetric measurements between measurements initially performed before the segmentation-reconstruction pipeline and measurements performed after segmentation-reconstruction. Statistically significant differences have been found for GM1, GM2, V, and WM. This confirms that segmentation results are in fact driven by the segmentation-driven reconstruction. Further evaluation of segmentation performance in terms of region overlap and surface distance should nonetheless be conducted to conclude if the segmentation results are ultimately improved.

Results clearly demonstrate the inter-dependence existing between reconstruction, segmentation and the resulting quantitative analysis (volumetry). Quantitative evaluation of the contrast-related histogram spread shows higher contrast in images reconstructed using the segmentation-driven approach than in initial images reconstructed by the improved reconstruction-only pipeline. This might suggest that our new approach allow the reconstruction of better contrasted tissues. We can also observe that the stronger the contribution of the GMM term is, the more homogenized are the intensities within a region, the more reduced is the number of intensities sitting around the boundaries of two regions, and the closer reconstructed images are to their segmentation. There are indeed not exactly the same as the TV term preserves edges with respect to the reconstructed image. Differences obtained in the volumetric measurements indicate that segmentation results are driven by the segmentation-driven reconstruction.

Note that in this work, we have been limited in performing the segmentation-reconstruction loop only once in order to avoid a risk of circularity as our segmentation method is not completely atlas-free. However, it would be possible to repeat it until convergence of the segmentation if an accurate and completely atlas-free segmentation method is adopted, such as one based on topological and/or intensity priors, but currently available atlas-free segmentation methods in fetal brain MRI have not shown to be sufficiently accurate yet.

4.6 Super-resolution to increasing in-plane fetal MRI resolution

4.6.1 Motivation

Although segmentation of large structures from HR images reconstructed can be accurately handled, thick structures such as the thick cortical GM layer still suffer from a significant partial volume effect which degrades the accuracy of their delineation. On the acquisition side, resolution of the acquired scans could not be increased with current MRI sequences constrained by a compromise between fast acquisition speed and sufficient SNR. On the retrospective HR image reconstruction side, models in current fetal SR algorithms are designed such that they could provide isotropic HR images reconstructed only at the in-plane resolution of the acquired scans. However, the super-resolution framework (Equation 4.1) allows the reconstruction of images at increased resolution in any dimension. Despite the debate that exists about the feasibility of addressing the resolution improvement in the in-plane dimensions by acquiring scans with shifted FOV (in these dimensions), a relatively recent work has shown that such an improvement is theoretically possible, if motion occurs prior to imaging [3].

As Fetal MRI fully satisfied the condition of motion prior imaging and attracted to reduce the partial volume for subsequent segmentation and quantification tasks, this section will give a redefinition of the fetal super-resolution problem able to increase the resolution of the reconstructed image by a given upsampling factor and will investigate the feasibility of such an approach in a joint segmentation-reconstruction framework.

4.6.2 Method

In this section, I will redefine the SR formulation given by Equation 4.1 to allow SR reconstruction at increased isotropic resolution. It will consist of (1) making a new assumption on the isotropic voxel spacing of the reconstructed image and (2) adapting the construction of \mathbf{H}_{kl} to the new mapping between the scan voxels and the upsampled voxels in the reconstructed image. Let $\mathbf{X}^{\uparrow v}$ be the image to be reconstructed at the increased voxel resolution $\Delta\mathbf{X}^{\uparrow v}$ such that $\Delta\mathbf{X}^{\uparrow v} = v\Delta_{xy}^{LR}$ where Δ_{xy}^{LR} is the in-plane voxel resolution of the scans and v is the upsampling factor. The only change will affect the construction of \mathbf{H} , for which voxels in the scans would be mapped to a bigger amount of upsampled voxels in the reconstructed image. As a result, the TV SR problem keeps exactly the same primal-dual formulation

$$\min_{\mathbf{X}^{\uparrow v} \in \mathcal{S}_X^{\uparrow v}} \max_{\mathbf{P} \in \mathcal{S}_Y} \underbrace{\langle \mathbf{D}\mathbf{X}^{\uparrow v}, \mathbf{P} \rangle - F^*(\mathbf{P})}_{\|\mathbf{X}^{\uparrow v}\|_{TV}} + \frac{\lambda}{2} \sum_{kl} \underbrace{\|\mathbf{H}_{kl}\mathbf{X}^{\uparrow v} - \mathbf{X}_{kl}^{LR}\|}_{\mathbf{e}_{kl}}^2 + \underbrace{\delta_C(\mathbf{X}^{\uparrow v})}_{\mathbf{X}^{\uparrow v} \geq 0}, \quad (4.21)$$

and the iterative optimization scheme is unchanged. Figure 4.8 illustrates the new mapping between each scan voxel and each voxel of the reconstructed image. Figure 4.9 illustrates the SR problem for reconstruction at increased isotropic resolution side by side with the construction of \mathbf{H}_{kl} s. Depending on the sparsity and size of the problem (number of HR voxels mapped to each LR voxel and number of HR voxels representing the brain), computational time of SR at resolution $\Delta\mathbf{X}^{\uparrow v}$ is expected to be in the order of $v\frac{\Delta_{xy}^{LR}}{\Delta_X}$ times longer than SR at resolution Δ_X .

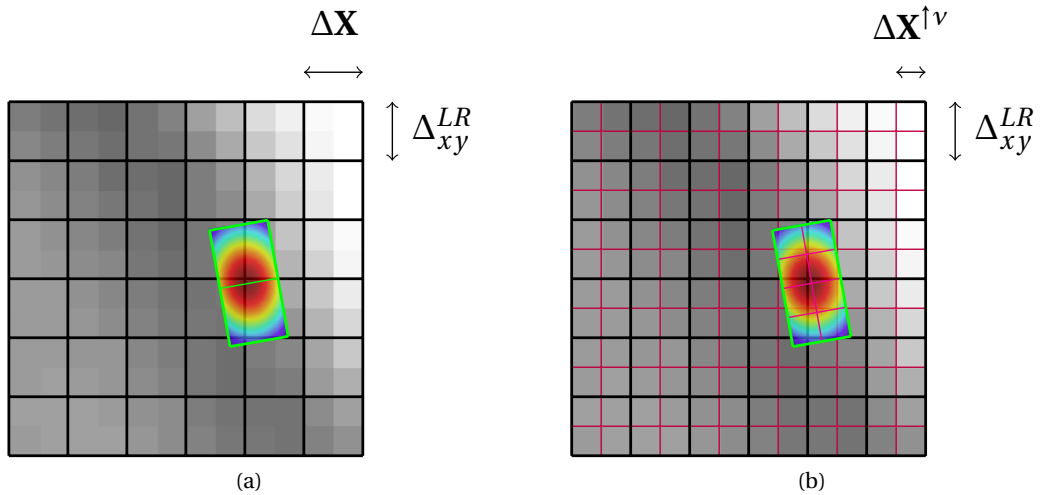


Figure 4.8 – Comparison between (a) the mapping used previously and (b) the mapping proposed for increased resolution in the in-plane dimensions. The black represents the original in-plane isotropic resolution ($\Delta\mathbf{X} = \Delta_{xy}^{LR}$). The red grid represents the increased resolution by an upsampling factor of 2 ($\Delta\mathbf{X}^{\uparrow v} = \frac{1}{2}\Delta_{xy}^{LR}$).

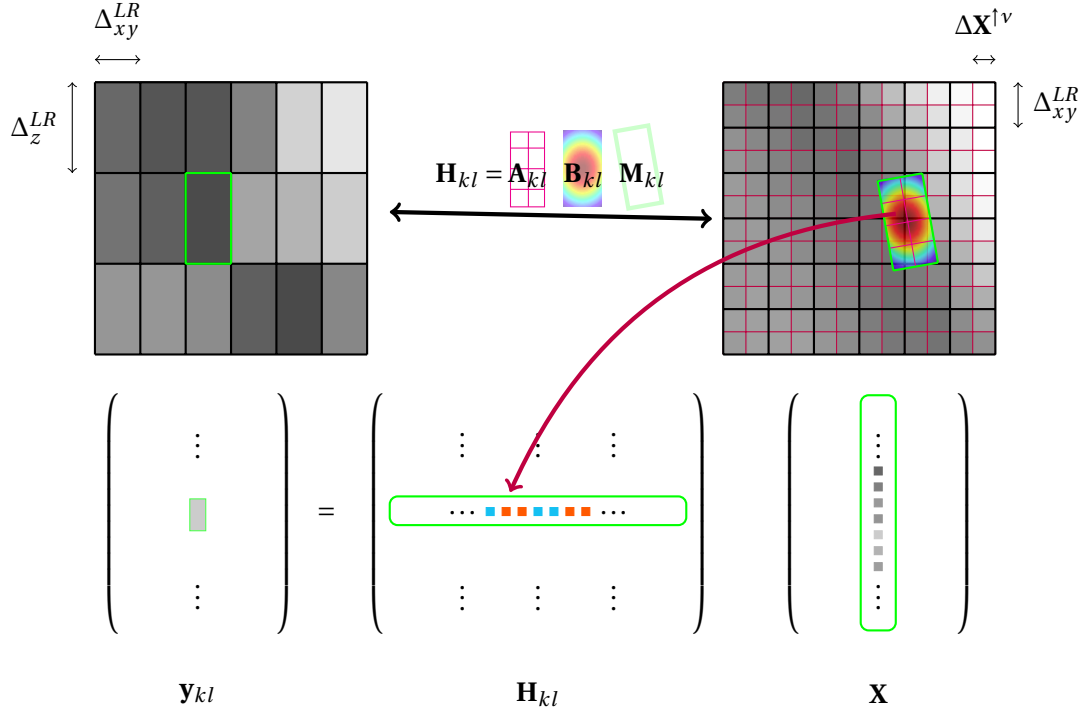


Figure 4.9 – Mapping between anisotropic voxels of the scans (left) and voxels of the reconstructed image (right). Δ_{xy}^{LR} and Δ_z^{LR} denote the in-plane and the slice-select direction resolution of the acquired scans. $\Delta \mathbf{X}^{1v}$ denotes the desired increased resolution. In this example, we consider an upsampling factor v of 2 that corresponds to have $\Delta \mathbf{X}^{1v} = 0.5 \Delta_{\mathbf{x}_{xy}^{LR}}$. We construct \mathbf{H}_{kl} such that voxels $\mathbf{X}^{1v}(j)$ s of the image \mathbf{X}^{1v} contributing to the value of each scan voxel $\mathbf{y}_{kl}(i)$ of the dataset lie in the region described by the anisotropic voxel after applying the upsampling operator \mathbf{A}_{kl} the estimated motion \mathbf{M}_{kl} . Weight $\mathbf{H}_{kl}(i, j)$ is computed from our Gaussian-based point spread function \mathbf{B}_{kl} modeling the image degradation and overlaid on the reconstructed image. Illustration is done in 2D for simplification but it works the same in 3D.

4.6.3 Results

In this section, we will investigate for the first time the impact of in-plane resolution improvement on fetal brain volumetry through super-resolution in fetal MRI using the small clinical fetal dataset described and used in Section 4.5. For each case, three HR images were reconstructed at $1 \times 1 \times 1 \text{ mm}^3$, $0.8 \times 0.8 \times 0.8 \text{ mm}^3$ (atlas resolution), and $0.5 \times 0.5 \times 0.5 \text{ mm}^3$ using the improved reconstruction pipeline (Figure 4.1). A very conservative Huber norm threshold ($t = 3$) was selected as scans were modestly affected by motion.

To preliminary investigate the impact on quantitative analysis, we performed the same joint reconstruction-segmentation procedure as adopted in the last section. Quantitative volumetry

4.6. Super-resolution to increasing in-plane fetal MRI resolution

and image contrast results are respectively presented in Figure 4.10 and 4.11. Reconstruction and segmentation results for case C1 are presented in Figure 4.12. Visual inspection and

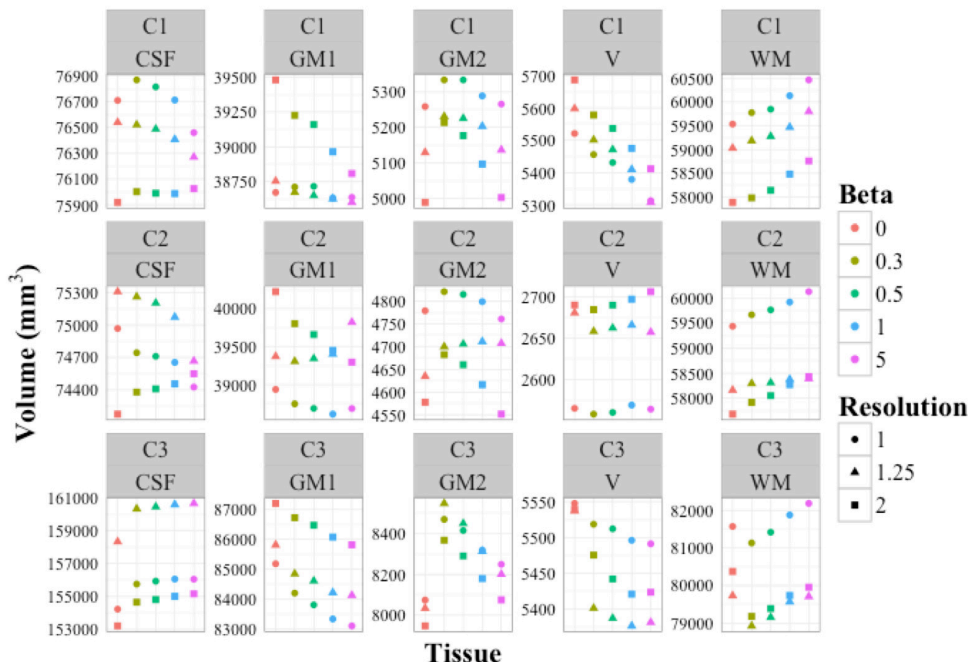


Figure 4.10 – Impact of segmentation-driven reconstruction on further volumetric analysis using image reconstructed with increased isotropic resolution on further volumetric analysis of pericerebral CSF (CSF), cortical gray matter (GM1), central nervous system (GM2), ventricles (V), and white matter (WM). Resolution corresponds to the upsampling factor relative to the original in-plane resolution of the scans. We can clearly see differences in the volumetric measurements between measurements performed at different reconstructed image resolution before and after the segmentation-reconstruction pipeline. This suggests that segmentation results are in fact affected by the resolution of the reconstruction image. Further evaluation of segmentation performance in terms of region overlap and surface distance should be conducted to conclude if the segmentation results are improved.

quantitative results confirms the interdependence between resolution, reconstruction and segmentation. In general, we can observe that increasing the resolution allows segmentation to recover smoother interfaces between tissues, suggesting that the partial volume effect might be reduced by reconstructing images at higher resolution. Although we cannot observe a clear general improvement in terms of contrast, we can see a clear increase in the contrast metric for cases C2 and C3 when the image is reconstructed at $0.5 \times 0.5 \times 0.5mm^3$, and for case C3 when the image is reconstructed at $0.8 \times 0.8 \times 0.8mm^3$ (which fits the resolution of the reconstructed image to the resolution of the atlas). This suggests that adopting a segmentation-driven approach with increased output resolution could potentially allow the reconstruction of images with better contrasted tissues but this has to be taken cautiously as it could not be generalized yet. Differences in the volumetric measurements at different reconstructed image resolution before and after the segmentation-reconstruction pipeline

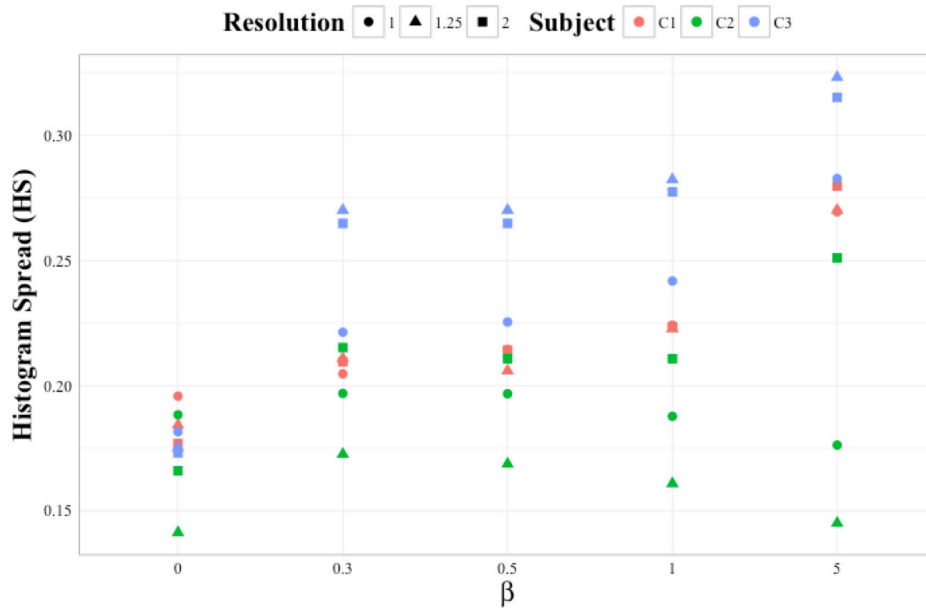


Figure 4.11 – Impact of segmentation-driven reconstruction on reconstructed image contrast using image reconstructed with increased isotropic resolution. The contrast in the image is evaluated, similarly to the segmentation-reconstruction study previously presented, using the histogram spread metric, presented in [17]. Resolution corresponds to the upsampling factor relative to the original in-plane resolution of the scans. Although we cannot observe a clear general improvement in terms of contrast, we can see a clear increase in the contrast metric for cases C2 and C3 when using an upsampling factor 2, and for case C3 when using an upsampling factor of 1.25 (which fits the resolution of the reconstructed image to the resolution of the atlas). This suggests that adopting a segmentation-driven approach with increased output resolution could potentially allow the reconstruction of images with better contrasted tissues but this could not be generalized yet. We can finally observe, similarly than in the previous segmentation-reconstruction study, that the stronger the contribution of the GMM term is, the stronger the contrast is. This is especially true for all β values when reconstructing images at a resolution upsampling factor of 2.

suggest that segmentation results are in fact affected by the resolution of the reconstruction image. In order to to conclude if the segmentation results are improved, further evaluation of segmentation performance in terms of region overlap and surface distance should be conducted.

4.7 Conclusion

In the chapter I have presented further promising improvements that could allow a more accurate image analysis. Firstly, new methods have been proposed to improve the reconstruction pipeline. Our bias field correction method integrated in the super-resolution framework allows the reconstruction of an image quasi free of the smooth magnetic bias field (Section4.3).

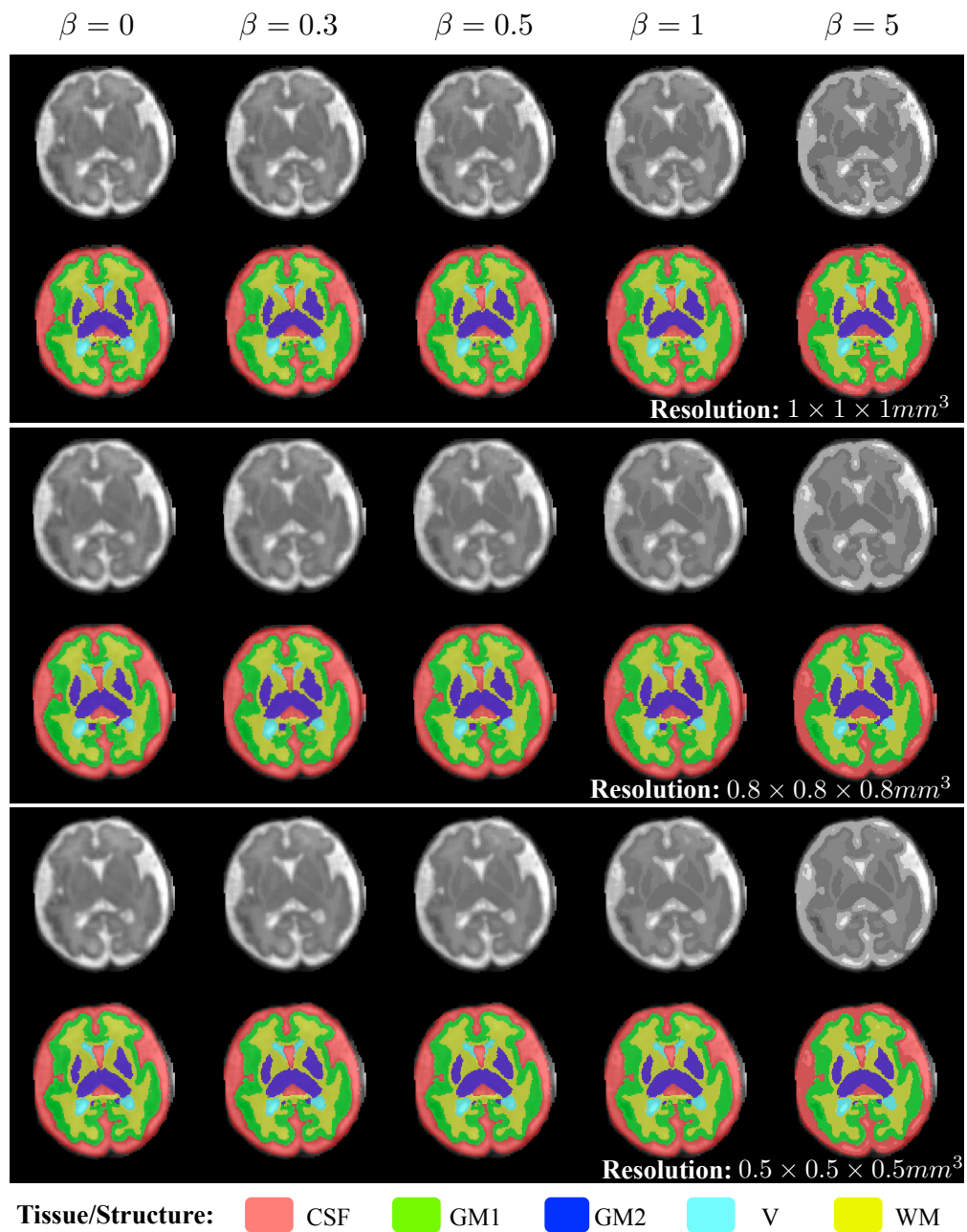


Figure 4.12 – Reconstruction and segmentation results for cases C3, when using our joint reconstruction-segmentation pipeline for a varying segmentation (GMM) contribution weight $\beta = [0.3, 0.5, 1, 5]$ and at varying resolution $\Delta X^{1v} = v\Delta X_{xy}^{LR}$ with $v = [1.0, 0.8, 0.5]$ in the super-resolution process. The first row illustrates reconstructed images and their segmentations which correspond to the initial images reconstructed before segmentation-reconstruction. We can observe that increasing the resolution allows to recover smoother interfaces between tissues. This suggests that the partial volume effect might be reduced by providing images at higher resolution.

Chapter 4. Further Improvements

The integration of the Huber norm in the TV algorithm allows the reconstruction to be more robust to inaccurate slice alignments (Section 4.4). Secondly, a novel segmentation-driven TV algorithm as well as a reconstruction-segmentation framework have been presented to perform jointly reconstruction and segmentation (Section 4.5). Results indicate segmentation might allow the reconstruction of better contrasted tissues. They also indicate that volumetry and thus segmentation results change when using segmentation-driven reconstructed images. This supports that such an approach could produce images with enhanced edge information that would change their segmentation. However, current results do not provide an answer yet to whether or not such an approach could improve segmentation results. Further performance evaluation of segmentation should thus be performed. Finally, we have preliminary investigated the feasibility of using super-resolution to increase the final isotropic resolution and the potential impact of higher resolution on volumetry results coming from segmentations (Section 4.6).

The next chapter will give the conclusion of this thesis and it will suggest new research perspectives.

Acknowledgment

This work was supported in part by the Swiss National Science Foundation under Grant and PhD Mobility Grant SNSF-141283, the CIBM of Geneva-Lausanne Universities and EPFL, the Fondation Leenaards and Fondation Louis-Jeantet, and in part by the National Institutes of Health (NIH) grants R01EB0118988, R01EB013248, and R03DE22109.

Bibliography

- [1] A. Gholipour, J. Estroff, S. Warfield, Robust super-resolution volume reconstruction from slice acquisitions: Application to fetal brain MRI, *Medical Imaging, IEEE Transactions on* 29 (10) (2010) 1739–1758.
- [2] E. Carmi, S. Liu, N. Alon, A. Fiat, D. Fiat, Resolution enhancement in MRI, *Magnetic Resonance Imaging* 24 (2) (2006) 133–154.
- [3] G. S. Mayer, E. R. Vrscay, *Mathematical Analysis of “Phase Ramping” for Super-Resolution Magnetic Resonance Imaging*, Springer, 2006, pp. 82–93.
- [4] M. Styner, C. Brechbuhler, G. Szckely, G. Gerig, Parametric estimate of intensity inhomogeneities applied to MRI, *Medical Imaging, IEEE Transactions on* 19 (3) (2000) 153–165.
- [5] N. J. Tustison, B. B. Avants, P. A. Cook, Y. Zheng, A. Egan, P. A. Yushkevich, J. C. Gee, N4ITK: improved N3 bias correction, *Medical Imaging, IEEE Transactions on* 29 (6) (2010) 1310–20.
- [6] F. Rousseau, O. A. Glenn, B. Iordanova, C. Rodriguez-Carranza, D. B. Vigneron, J. A. Barkovich, C. Studholme, Registration-based approach for reconstruction of high-resolution in utero fetal MR brain images, *Academic Radiology* 13 (9) (2006) 1072–1081.
- [7] K. Kim, P. Habas, F. Rousseau, O. Glenn, A. Barkovich, C. Studholme, Intersection based motion correction of multislice MRI for 3-D in utero fetal brain image formation, *Medical Imaging, IEEE Transactions on* 29 (1) (2010) 146–158.
- [8] M. Kuklisova-Murgasova, G. Quaghebeur, M. A. Rutherford, J. V. Hajnal, J. A. Schnabel, Reconstruction of fetal brain MRI with intensity matching and complete outlier removal, *Medical Image Analysis* 16 (8) (2012) 1550–1564.
- [9] M. J. Black, G. Sapiro, D. H. Marimont, D. Heeger, Robust anisotropic diffusion, *IEEE Transactions on Image Processing* 7 (3) (1998) 421–432.
- [10] J. Miller, Short report: Reaction time analysis with outlier exclusion: Bias varies with sample size, *The Quarterly Journal of Experimental Psychology Section A* 43 (4) (1991) 907–912.
- [11] C. Leys, C. Ley, O. Klein, P. Bernard, L. Licata, Detecting outliers: Do not use standard deviation around the mean, use absolute deviation around the median, *Journal of Experimental Social Psychology* 49 (4) (2013) 764–766.
- [12] S. Tourbier, X. Bresson, P. Hagmann, J.-P. Thiran, R. Meuli, M. B. Cuadra, An efficient total variation algorithm for super-resolution in fetal brain MRI with adaptive regularization, *NeuroImage* 118 (2015) 584–597.

- [13] S. Jiang, H. Xue, A. Glover, M. Rutherford, D. Rueckert, J. Hajnal, MRI of moving subjects using multislice snapshot images with volume reconstruction (SVR): Application to fetal, neonatal, and adult brain studies, *Medical Imaging, IEEE Transactions on* 26 (7) (2007) 967–980.
- [14] J. Caballero, W. Bai, A. N. Price, D. Rueckert, J. V. Hajnal, Application-driven MRI: Joint reconstruction and segmentation from undersampled mri data, in: P. Golland, N. Hata, C. Barillot, J. Hornegger, R. Howe (Eds.), *Medical Image Computing and Computer Assisted Intervention (MICCAI), International Conference on*, Springer, 2014, pp. 106–113.
- [15] A. Gholipour, A. Akhondi-Asl, J. A. Estroff, S. K. Warfield, Multi-atlas multi-shape segmentation of fetal brain MRI for volumetric and morphometric analysis of ventriculomegaly, *NeuroImage* 60 (3) (2012) 1819–1831.
- [16] A. Gholipour, C. Limperopoulos, S. Clancy, C. Clouchoux, A. Akhondi-Asl, J. A. Estroff, S. K. Warfield, Construction of a deformable spatiotemporal MRI atlas of the fetal brain: Evaluation of similarity metrics and deformation models, in: P. Golland, N. Hata, C. Barillot, J. Hornegger, R. Howe (Eds.), *Medical Image Computing and Computer Assisted Intervention (MICCAI), International Conference on*, Vol. 8674 of *Lecture Notes in Computer Science*, Springer, 2014, pp. 292–299.
- [17] A. K. Tripathi, S. Mukhopadhyay, A. K. Dhara, Performance metrics for image contrast, in: *Image Information Processing (ICIIP), 2011 International Conference on*, IEEE, 2011, pp. 1–4.

5

Conclusion and perspectives

Conclusion

In this thesis I have presented novel advanced image processing methods that have proven to improve current *state-of-the-art* fetal MRI reconstruction in terms of efficiency, robustness and minimized user-interactions. I will give a brief summary according to these properties.

Efficiency An efficient SR algorithm that combines exact Total Variation regularization with fast convex optimization has been presented and extensively validated in Chapter 1. This algorithm has shown to be more efficient thanks to its optimality in the sense of convex optimization theory, and more robust to motion estimation errors than Tikhonov- and approximated TV-regularized based algorithms [1, 2]. An extension of this algorithm has been presented and preliminary evaluated in Chapter 4 where an additional discriminative GMM term estimated from segmentation has been introduced in order to enable joint reconstruction-segmentation.

Robustness A first image preprocessing pipeline has been presented in Chapter 1 to guarantee the success of motion estimation and super-resolution processes. It combines brain localization and extraction to isolate brain-relevant voxels from the surrounding tissues and intensity standardization through global bias field correction and brain histogram equalization. An improved bias field correction method has been presented in Chapter 2 which estimates and corrects the bias field slice-by-slice taking into account possible inter-slice motion. Although this approach has shown to perform relatively well in most cases, few intensity artifacts were still present in the reconstructed image and more importantly the

reconstructed images were still corrupted by the smooth magnetic bias field inherent in MRI. A further improved bias field correction method has been presented in Chapter 4 that has shown to correct more consistently and more coherently the bias field, which indeed enables the reconstruction of images quasi free of the smooth magnetic bias field. Last but not least, the ℓ_2 -norm of the efficient algorithm, as presented in Chapter 1, might be still sensitive to misaligned slices and artifacts might be still present in the reconstructed images. A more robust TV algorithm based on the Huber norm has been presented and preliminary evaluated in Chapter 4.

Minimized user-interaction The intensity standardization methods involved in the image preprocessing pipeline, as presented in Chapter 1 and improved in Chapters 2 and 4, are non-parametric so that it is completely user interaction free. Moreover, to automatize the first two inherent steps of the image preprocessing pipeline, involving fetal brain localization and extraction, has been preliminary addressed using a multi-atlas strategy with reconstructed images of patient [3, 4]. The technique has been improved and a novel age-matched template-based method based on template-to-slice block matching and deformable slice-to-template registration has been presented and extensively validated in Chapter 2. The proposed slice-by-slice approach has shown to be more robust than a global rigid 3D template-registration-based approach as it allows brain extraction to take into account for inter-slice motion. Moreover, the proposed automatic pipeline has demonstrated to achieve similar reconstruction quality to reference reconstruction based on manually drawn masks without any effort. Open perspective of complete automatic cortical folding quantification, one of the best indicators of brain maturation, has been presented in Chapter 3 by combining the automatic reconstruction pipeline, proposed in Chapter 2, with the *state-of-the-art* multi-atlas multi-shape brain tissue segmentation method [5], and with existing automated tools provided for adult brain's cortical folding quantification. Results have indicated that the proposed automatic reconstruction pipeline could in turn provide HR images with sufficient quality that enable the use of surface tessellation and active surface algorithms similar to those developed for adult brains to extract meaningful information about fetal brain maturation [6].

Perspectives

In this thesis, I have shown that fetal MRI reconstruction techniques have been taken to the stage where a high-resolution image can now be automatically, efficiently and robustly reconstructed. However, the **quality of the reconstruction is highly dependent on the acquisition**. One should follow the **25s one scan acquisition golden rule** [7] to minimize risk of motion artifacts. We also would like to remind the reader that the ill-posedness of the subsequent super-resolution problem is function of the squared of the super-resolution factor (ratio between in-plane resolution $\Delta\mathbf{X}_{xy}^{LR}$ and slice thickness $\Delta\mathbf{X}_{xy}^{LR}$). In addition, a limited number of observation emphasizes the ill-posedness of the inverse problem that requires more regularization to be stable and will result in less details in the reconstructed image. Therefore, we advise to

take a resolution ratio in the order of 2-3, which means a number in the order of 4-9 scans are theoretically needed for quasi optimal reconstruction. This setup has demonstrated to allow the reconstruction of good quality images when one or two scans at least are acquired per anatomical direction.

Despite the implementation of algorithms robust to misaligned slices, they might fail if highly motion- and intensity- corrupted data is present in one of the scans. Such scans are typically visually identified and discarded from the reconstruction pipeline beforehand. Automated methods could be developed to address this **quality control** problem. For instance, a machine learning system could be designed and trained in order to detect and reject bad slices and scans. An other approach could be to use the generalized cross validation method to quantify the effect of removing a slice or a scan on the reconstruction quality to detect and reject them.

There exists in the literature a number of quantitative studies of fetal brain development and maturation but most of the works are limited to the study of the normal developing brain and relies on atlas-based segmentation approaches. Although the most promising method [5] incorporates shape models of structures as well as regional intensity values and prior information coming from multi-atlas segmentations into a probabilistic optimization framework to address to segmentation of ventricles in severe forms of ventriculomegaly where large anatomical variability can be observed, such approaches are strongly influenced by anatomical atlas priors, and therefore prone to give potentially biased results with pathological data, as each brain is deformed to the atlas anatomy. However, **application to pathological data is essential in clinical practice**. Moreover, such approaches might limit new research perspectives. For instance, Chapter 4 has presented a novel and very promising framework to address jointly reconstruction and segmentation processes but this framework is currently limited by the risk of circularity of the segmentation method adopted.

The development of an **accurate atlas-free segmentation methods** for fetal brain MRI would be of great importance to overcome circularity in this joint reconstruction and segmentation process. Only a few fetal brain segmentation methods have been proposed in the literature to address this problem, from which one of the most promising method uses structural constraints based on a topological model and a morphological filter to identify the regions where the cortex appears the most likely [8]. An other direction would be to use non-local information, extracted from a graph representation of the image [9]. Indeed such segmentation framework has shown to be performant in a variety of application. It has also shown to provide the flexibility in incorporating many soft prior, including local spatial priors, sparsity constraints (like the Total Variation regularization), or data-driven priors from labels. Ultimately, this would open new perspectives to jointly perform reconstruction and segmentation until segmentation has converged.

Fetal MRI reconstruction techniques can provide high-resolution images but a significant partial volume effect is still present in fine structures such as the cortex, which degrades the estimation of the interface boundary between tissues. Increasing the resolution would also be

of great importance to reduce this problem. As seen in the introduction, resolution cannot be more improved with current dense-k-space-sampling multi-slice acquisition sequences. A retrospective solution has been investigated in Chapter 4 by addressing in-plane resolution improvement through super-resolution. Preliminary results shows output resolution of the image influences segmentation and consecutive volumetric analysis. Despite preliminary results remain inconclusive about the feasibility of super-resolution to improve the in-plane resolution in fetal MRI, such an approach is theoretically supported as fetal motion occurs prior to imaging of each good quality slice. In addition, results has shown the potential using prior information from segmentation in a reconstruction-segmentation framework could benefit in regularizing super-resolution at increased resolution.

A last but not least solution would be the **development of new multi-slice sequences taking advantage of compressed-sensing** [10, 11], a new emerging field of techniques in MRI that aims at reconstructing images from downsampled k-space, where the Nyquist sampling criterion is not fulfilled anymore. We refer to [12] for a detailed review of compressed sensing MRI. Porting compressed-sensing to SST2W sequences would involve (1) the design of an adequate k-space undersampling scheme in the phase-encoding direction and (2) the development of new compressed-sensing algorithms. By adopting compressed-sensing, one could expect either to reach an acquisition acceleration speed-up or a resolution improvement in the order of the undersampling k-space factor.

In summary, retrospective fetal MRI reconstruction techniques are now well established. Despite they have demonstrated their advantages in a number of papers in the neuroscience community, few methods are publicly available [13–16] but are not very easily accessible or not easy-to-use for the clinical community and consequently not well integrated into clinical practice. However, as stated in this thesis, the **translation of these techniques into clinical practice** have a great potential in significantly facilitating diagnosis and prognosis of the developing fetus. Typically, medical centers with Siemens scanners use the vendor-provided imaging software *syngo.via* in clinics. The recently developed *syngo.via* Frontier would allow us to integrate our own algorithms into the routinely used *syngo.via* software in a transparent way for the clinicians. This would enable to test and further improve these techniques in close link with the clinicians able to evaluate their potential impacts.

Bibliography

- [1] S. Tourbier, X. Bresson, P. Haggmann, J.-P. Thiran, R. Meuli, M. Bach Cuadra, Efficient total variation algorithm for fetal brain MRI reconstruction, in: P. Golland, N. Hata, C. Barillot, J. Hornegger, R. Howe (Eds.), *Medical Image Computing and Computer Assisted Intervention (MICCAI)*, International Conference on, no. 8674 in *Lecture Notes in Computer Science*, Springer, 2014, pp. 252–259.
- [2] S. Tourbier, X. Bresson, P. Haggmann, J.-P. Thiran, R. Meuli, M. B. Cuadra, An efficient total variation algorithm for super-resolution in fetal brain MRI with adaptive regularization, *NeuroImage* 118 (2015) 584–597.
- [3] S. Tourbier, X. Bresson, P. Haggmann, M. Cagneaux, M. Schaer, L. Guibaud, J.-P. Thiran, R. Meuli, M. B. Cuadra, Automated Brain Extraction in Fetal MRI by Multi-Atlas Fusion Strategy: Study on Healthy and Pathological Subjects., *Joint Annual Meeting ISMRM-ESMRMB*, 2014.
- [4] S. Tourbier, P. Haggmann, M. Cagneaux, L. Guibaud, S. Gorthi, M. Schaer, J.-P. Thiran, R. Meuli, M. B. Cuadra, Automatic brain extraction in fetal MRI using multi-atlas-based segmentation, in: *Proc. SPIE Medical Imaging*, Vol. 9413, 2015, pp. 94130Y–94130Y–7.
- [5] A. Gholipour, A. Akhondi-Asl, J. A. Estroff, S. K. Warfield, Multi-atlas multi-shape segmentation of fetal brain MRI for volumetric and morphometric analysis of ventriculomegaly, *NeuroImage* 60 (3) (2012) 1819–1831.
- [6] S. Tourbier, M. Schaer, S. Warfield, R. Meuli, A. Gholipour, M. B. Cuadra, Quantification of fetal cortical folding using slice-to-volume reconstructed MRI and freesurfer, in: *22nd Annual Meeting of the Organization for Human Brain Mapping (OHBM)*, 2016.
- [7] A. Gholipour, J. A. Estroff, C. E. Barnewolt, R. L. Robertson, P. E. Grant, B. Gagoski, S. K. Warfield, O. Afacan, S. A. Connolly, J. J. Neil, et al., Fetal MRI: A technical update with educational aspirations, *Concepts in Magnetic Resonance Part A* 43 (6) (2014) 237–266.
- [8] B. Caldairou, N. Passat, P. A. Habas, C. Studholme, M. Koob, J.-L. Dietemann, F. Rousseau, Segmentation of the cortex in fetal MRI using a topological model, in: *Biomedical Imaging (ISBI)*, International Symposium on, IEEE, 2011, pp. 2045–2048.
- [9] Y. Boykov, G. Funka-Lea, Graph cuts and efficient n-d image segmentation, *Int. J. Comput. Vision* 70 (2) (2006) 109–131.
- [10] M. Lustig, D. Donoho, J. M. Pauly, Sparse MRI: The application of compressed sensing for rapid mr imaging, *Magnetic Resonance in Medicine* 58 (6) (2007) 1182–1195.
- [11] M. Lustig, D. L. Donoho, J. M. Santos, J. M. Pauly, Compressed sensing MRI, *IEEE Signal Processing Magazine* 25 (2) (2008) 72–82.

- [12] S. Geethanath, R. Reddy, A. S. Konar, S. Imam, R. Sundaresan, R. B. D. R., R. Venkatesan, Compressed sensing MRI: A review, *Critical Reviews & trade; in Biomedical Engineering* 41 (3) (2013) 183–204.
- [13] F. Rousseau, E. Oubel, J. Pontabry, M. Schweitzer, C. Studholme, M. Koob, J.-L. Dietemann, BTK: An open-source toolkit for fetal brain MR image processing, *Computer Methods and Programs in Biomedicine* 109 (1) (2013) 65–73.
- [14] B. Kainz, M. Steinberger, W. Wein, M. Kuklisova-Murgasova, C. Malamateniou, K. Ker-audren, T. Torsney-Weir, M. Rutherford, P. Aljabar, J. V. Hajnal, et al., Fast volume recon-struction from motion corrupted stacks of 2D slices, *Medical Imaging, IEEE Transactions on* 34 (9) (2015) 1901–1913.
- [15] K. Kim, P. Habas, F. Rousseau, O. Glenn, A. Barkovich, C. Studholme, Intersection based motion correction of multislice MRI for 3-D in utero fetal brain image formation, *Medical Imaging, IEEE Transactions on* 29 (1) (2010) 146–158.
- [16] K. Kim, P. A. Habas, V. Rajagopalan, J. A. Scott, J. M. Corbett-Detig, F. Rousseau, A. J. Barkovich, O. A. Glenn, C. Studholme, Bias field inconsistency correction of motion-scattered multislice MRI for improved 3D image reconstruction, *Medical Imaging, IEEE Transactions on* 30 (9) (2011) 1704–1712.



MIALSRTK: C++ Medical Image Analysis Laboratory Super-Resolution ToolKit

In this annex, we will briefly describe the Medical Image Analysis Laboratory Super-Resolution Toolkit (MIALSRTK). This toolkit consists of a set of C++ image processing tools based on the open-source image processing Insight ToolKit (ITK) library [1] and the command line parser TCLAP library. Source code is available on a git repository. To clone the repository, use the following command:

```
1 git clone https://tourbier@git.epfl.ch/repo/externalmialtoolkit.git
```

Note: The address of the git repository corresponds to the one used at the time of writing this thesis. Please check on the Medical Image Analysis Laboratory website for the most up-to-date repository address and it might change in the future.

A readme file is provided to guide the user in the installation process. The toolkit has been implemented and tested on Linux (Debian Ubuntu 12.04) and MacOSX (10.9.5). MIALSRTK consists of a set of tools necessary to perform the whole reconstruction pipeline (Figure A.1) where all algorithms and methods for brain localization and extraction, intensity standardization, motion estimation, and super-resolution have been implemented, except the NLM denoising program which is part of the Baby ToolKit (BTK) library [2]. The USAGE message of each tool can be obtained using either the `-h` or `--h` flag. They will be listed and briefly described according to their role in the pipeline.

A.1 Image denoising

mialsrtkGaussianDenoising Denoises the image through basic anisotropic Gaussian denoising.

Appendix A. MIALSRTK: C++ Medical Image Analysis Laboratory Super-Resolution Toolkit

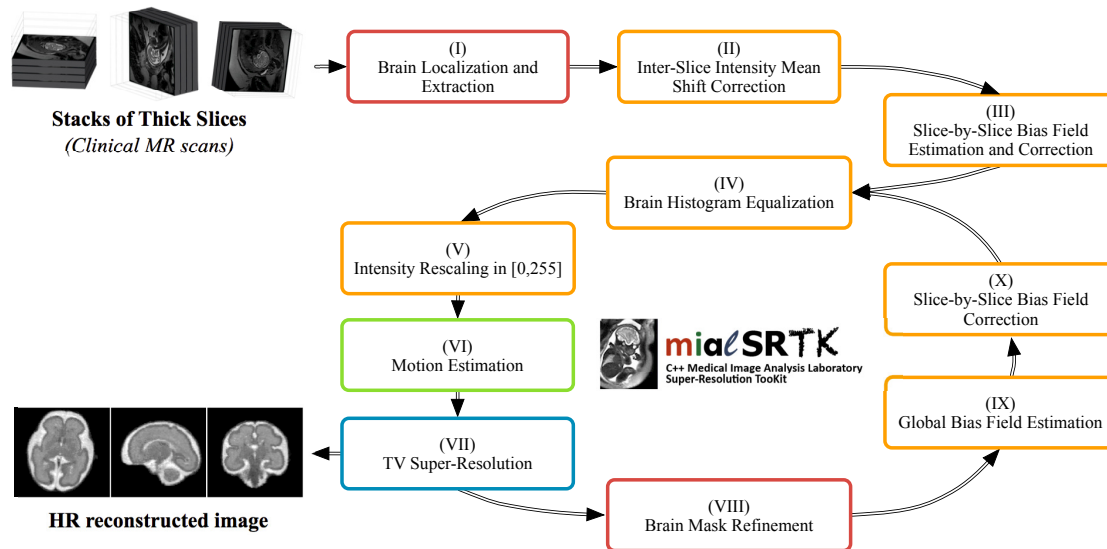


Figure A.1 – Our ultimate reconstruction pipeline for fetal MRI using MIALSRTK. All algorithms and methods developed in the context of this thesis have been implemented in the toolkit. They are highlighted according to their role in the pipeline. It consists of a set of tools addressing automatically brain extraction (red), intensity standardization (yellow), motion estimation (green) and super-resolution (blue).

mialsrtkTVDenosing Denoises the image through efficient minimization of the exact Total Variation energy. TV denoising like TV super-resolution is not trivial and the primal-dual technique [3] is adopted for optimization.

A.2 Brain localization and extraction

mialsrtkFetalBrainLocalizer Performs brain localization using the slice-to-template block matching algorithm [4], presented in Section 2.4.1. It outputs a LR image that has been reoriented and cropped in the template brain space.

mialsrtkOrientImage Depending on the imaging center protocol, it can happen that the slice-select direction does not correspond to the third dimension. However, the motion estimation and super-resolution algorithms are implemented based on the assumption that the slice-select direction is the third direction, in which context they fail. This tool allows us to fix this issue by specifying a correct anatomical slice-select direction (axial, coronal or sagittal).

mialsrtkRefineHRMask Refines the brain mask of multiple scans. Specifically, it uses the method presented in Section 2.4.4 where brain masks are refined in the spatial space of the template using a consensus fusion voting process, which are re-applied to the scans using the tool `mialsrtkMaskImage`.

mialsrtkSegmentationWeightedFusionWithUnanimousConsensus Performs label fusion of multiple segmentation, where the fusion strategy can be: majority voting, global weighted voting and local weighted voting. Weight are based on the normalized cross correlation. This tool has been implemented in the context of our first works on brain extraction [5, 6] using multiple reconstructed images from subjects as atlases.

mialsrtkSliceToTemplateCompositeVersor2DBSplineRegistration Performs rigid slice-to-template registration followed by two-dimensional B-Spline deformation (essential in case of anatomical variability) to refine the brain mask slice by slice (essential in case of motion). It implements the slice-by-slice brain extraction method presented in Section 2.4.2.

A.3 Intensity standardization

mialsrtkCorrectSliceIntensity Estimates a global mean intensity in the brain region of the volumetric image and mean intensity in the brain region of each slice is shifted towards the global mean intensity. It has as effect to correct for shifts in intensity levels that might be present between the slices. It implements the *slice-by-slice* mean intensity equalization method presented in Section 2.4.3.

mialsrtkCorrectBiasFieldWithMotionApplied Generates the bias field and corrects each slice for it, given a global and smooth bias field estimated in the HR space (using the tool `mialsrtkN4BiasFieldCorrection` presented below) and using the estimated motion parameters. It implements the improved slice-by-slice bias field correction method presented in Section 4.3.

mialsrtkHistogramNormalization Normalizes intensities in multiple images using the brain intensity histogram equalization method [8], as presented in Section 2.4.3.

mialsrtkIntensityStandardization Rescale the intensity in the [0,255] range.

mialsrtkN4BiasFieldCorrection Estimates a global three-dimensional bias field in the input image using the N4 method [7].

mialsrtkSliceBySliceCorrectBiasField Applies the bias field estimated by the tool `mialsrtkSliceBySliceN4BiasFieldCorrection` (presented below) to other images. In practice, the bias field is estimated on a denoised image and then used for correction in the corresponding original image.

mialsrtkSliceBySliceN4BiasFieldCorrection Estimates and corrects a two-dimensional bias field independently in each slice of the input image using the N4 method [7]. It implements the slice-by-slice bias field correction method presented in Section 2.4.3.

A.4 Motion estimation

mialsrtkImageReconstruction Estimates the motion parameters using the most common iterative method [9–11] which alternate between slice-to-volume registration and scattered data interpolation using a Gaussian kernel. It implements the registration method used in all works.

A.5 Super-resolution

mialsrtkRobustTVSuperResolution Restores the HR image by performing TV super-resolution. It implements the efficient TV super-resolution algorithm presented in Section 1.4. By default, the ℓ_2 -norm is used in the data fidelity term. It also implements the more robust implementation based on the Huber norm, as presented in Section 4.4, which can be selected with the `--use-robust` and the discriminative mode of the Huber norm set with the `--mode` flag.

mialsrtkRobustTVSuperResolutionWithGMM Restores the HR image by performing segmentation-driven TV super-resolution. It implements the TV algorithm that incorporates discriminative GMM terms coming from a previous segmentation, as presented in Section 4.5. It also implements the more robust implementation based on the Huber norm, as presented in Section 4.4, which can be selected with the `--use-robust` and the discriminative mode of the Huber norm set with the `--mode` flag.

A.6 Evaluation tools

mialsrtkEvaluateReconstructionQualityMeasures Computes mean squared error (MSE), root mean squared error (RMSE), normalized root mean squared error (NRMSE), and peak signal-to-noise ratio (PSNR) between an input image and a reference image for the evaluation of the reconstruction quality.

mialsrtkEvaluateSharpnessMeasures Computes the gradient-based M1 and M2 sharpness measures of an input image for the evaluation of image contrast.

mialsrtkEvaluateLabelOverlapMeasures Computes different region overlap measures for the evaluation of segmentation performance. It includes: true and false positive, true and false negative, dice coefficient, precision, recall and accuracy.

mialsrtkComputeImageMedianCNR Computes the median contrast to noise ratio between two tissues given an input image and its segmentation.

mialsrtkComputeHausdorffDistance Computes the Hausdorff distance between two segmentations.

mialsrtkComputeHistogramSpread Computes the brain histogram spread of an input image for the evaluation of image contrast.

A.7 Other tools

mialsrtkComputeVolume Computes the volume of a given label in a given segmentation.

mialsrtkCropImageUsingMask Crops an input image where the cropping region is determined by smallest bounding box containing the brain mask.

mialsrtkMaskImage Masks an image with a given binary image.

mialsrtkFourierTransform Computes the magnitude of the Fourier transform of an input image.

mialsrtkCreateWhiteMatterVolumeFromLabels Combines all labels of an input segmentation lying inside the white matter volume in order to create the binary white matter volume used in Section 3.3.

mialsrtkCreateImageWithHalo Create a two-voxel width halo around the brain, as it was presented in 3.3

Bibliography

- [1] T. S. Yoo, M. J. Ackerman, W. E. Lorensen, W. Schroeder, V. Chalana, S. Aylward, D. Metaxas, R. Whitaker, Engineering and algorithm design for an image processing API: A technical report on ITK - the Insight Toolkit, in: J. Westwood (Ed.), Proc. of Medicine Meets Virtual Reality, Vol. 85, IOS Press Amsterdam, 2002, pp. 586–592.
- [2] F. Rousseau, E. Oubel, J. Pontabry, M. Schweitzer, C. Studholme, M. Koob, J.-L. Dietemann, BTK: An open-source toolkit for fetal brain MR image processing, *Computer Methods and Programs in Biomedicine* 109 (1) (2013) 65–73.
- [3] A. Chambolle, T. Pock, A First-Order Primal-Dual Algorithm for Convex Problems with Applications to Imaging, *Journal of Mathematical Imaging and Vision* 40(1) (2011) 120–145.
- [4] V. Taimouri, A. Gholipour, C. Velasco-Annis, J. Estroff, S. K. Warfield, A template-to-slice block matching approach for automatic localization of brain in fetal MRI, in: Biomedical Imaging (ISBI), International Symposium on, IEEE, 2015, pp. 144–147.
- [5] S. Tourbier, X. Bresson, P. Haggmann, M. Cagneaux, M. Schaer, L. Guibaud, J.-P. Thiran, R. Meuli, M. B. Cuadra, Automated Brain Extraction in Fetal MRI by Multi-Atlas Fusion Strategy: Study on Healthy and Pathological Subjects., Joint Annual Meeting ISMRM-ESMRMB, 2014.
- [6] S. Tourbier, P. Haggmann, M. Cagneaux, L. Guibaud, S. Gorthi, M. Schaer, J.-P. Thiran, R. Meuli, M. B. Cuadra, Automatic brain extraction in fetal MRI using multi-atlas-based segmentation, in: Proc. SPIE Medical Imaging, Vol. 9413, 2015, pp. 94130Y–94130Y–7.
- [7] N. J. Tustison, B. B. Avants, P. A. Cook, Y. Zheng, A. Egan, P. A. Yushkevich, J. C. Gee, N4ITK: improved N3 bias correction, *Medical Imaging, IEEE Transactions on* 29 (6) (2010) 1310–20.
- [8] L. G. Nyúl, J. K. Udupa, X. Zhang, New variants of a method of MRI scale standardization, *Medical Imaging, IEEE Transactions on* 19 (2) (2000) 143–150.
- [9] F. Rousseau, O. A. Glenn, B. Iordanova, C. Rodriguez-Carranza, D. B. Vigneron, J. A. Barkovich, C. Studholme, Registration-based approach for reconstruction of high-resolution in utero fetal MR brain images, *Academic Radiology* 13 (9) (2006) 1072–1081.
- [10] A. Gholipour, J. Estroff, S. Warfield, Robust super-resolution volume reconstruction from slice acquisitions: Application to fetal brain MRI, *Medical Imaging, IEEE Transactions on* 29 (10) (2010) 1739–1758.
- [11] M. Kuklisova-Murgasova, G. Quaghebeur, M. A. Rutherford, J. V. Hajnal, J. A. Schnabel, Reconstruction of fetal brain MRI with intensity matching and complete outlier removal, *Medical Image Analysis* 16 (8) (2012) 1550–1564.

Sébastien Tourbier

Avenue de Tivoli, 27A
1007 Lausanne, Switzerland

ResearchGate and LinkedIn profiles
sebastien.tourbier1@gmail.com
+41 76 637 92 95

Objectives

R&D Engineer with a special interest in imaging, signal and image processing, machine learning and pattern recognition problems with medical application. I am currently pursuing a PhD at the Center for Biomedical Imaging (CIBM), Lausanne, Switzerland, focusing on novel image processing methods for Fetal MR Imaging.

Education

- **University (UNIL) and University Hospital (CHUV) of Lausanne** Lausanne, CH
PhD in Life Sciences at the Medical Image Analysis Laboratory (MIAL) Oct. 2012 - Oct. 2016
– Project: development of advanced image processing methods to improve fetal MR images.
- **University College London (UCL)** London, UK
Medical Image Computing Summer School Aug. 2015
- **Boston Children's Hospital and Harvard Medical School** Boston, MA
Visiting PhD Student at the Computational radiology Laboratory (CRL) Jan. 2015 - July 2015
- **Swiss Federal Institute of Technology (EPFL)** Lausanne, CH
M. Sc. in Communication Systems Feb. 2009 - Sept. 2011
– Relevant courses: Foundations of Imaging Science, Image Processing, Statistical Signal Processing, Biomedical Signal Processing, Pattern Classification and Machine Learning, Neural networks, Biomedical sensors, Statistics for Genomic Data Analysis, Cell Biology and Biochemistry for Information Sciences.
- **EF International Language Schools** Vancouver, B.C.
Intensive English and Internship Courses Sept. 2008 - Jan. 2009
- **Swiss Federal Institute of Technology (EPFL)** Lausanne, CH
B. Sc. in Communication Systems Oct. 2005 - July 2008
– Relevant courses: Computer graphics, Computer programming, Computer Networks, Distributed Systems, Information Systems, Signal Processing for digital communications, Physics, Stochastic models.

Scientific contributions

- S. Tourbier, M. Schaer, S. Warfield, R. Meuli, A. Gholipour, M. B. Cuadra, Quantification of fetal cortical folding using slice-to-volume reconstructed MRI and freesurfer, in: 22nd Annual Meeting of the Organization for Human Brain Mapping (OHBM), 2016
- S. Tourbier, X. Bresson, P. Hagmann, R. Meuli, M. B. Cuadra, An efficient total variation algorithm for super-resolution in fetal brain MRI with adaptive regularization., *Neuroimage* 118 (2015) 584–597. doi:10.1016/j.neuroimage.2015.06.018
- S. Tourbier, P. Hagmann, M. Cagneaux, L. Guibaud, S. Gorthi, M. Schaer, J.-P. Thiran, R. Meuli, M. B. Cuadra, Automatic brain extraction in fetal MRI using multi-atlas-based segmentation, in: *Medical Imaging 2015: Image Processing*, Vol. 9413 of SPIE Proceedings, Spie-Int Soc Optical Engineering, Bellingham, March 20, 2015, 2015, p. 94130Y. doi:10.1117/12.2081777
- S. Tourbier, X. Bresson, P. Hagmann, R. Meuli, J.-P. Thiran, M. B. Cuadra, Efficient total variation algorithm for fetal MRI reconstruction, in: *17th International Conference on Medical Image Computing and Computer Assisted Intervention*, Vol. 8674 of Lecture Notes in Computer Science, 2014, pp. 252–259. doi:10.1007/978-3-319-10470-6_32

- M. Cagneaux, M. B. Cuadra, S. Tourbier, M. Schaer, S. Hannoun, L. Guibaud, D. Sappey-Marinier, Segmentation of fetal pericerebral spaces based on reconstructed high-resolution MRI, in: ISMRM 2014, 22nd of the International Society for Magnetic Resonance in Medicine. Proceedings of the International Society for Magnetic Resonance in Medicine, 2014, p. 4618
- M. Gianoni, M. Schaer, S. Tourbier, Y. Vial, M. Cagneaux, P. Hagmann, R. Meuli, L. Guibeaud, M. B. Cuadra, In-vivo 3d magnetic resonance volumetric analysis of fetal cerebellum: From normal to pathology (unilateral cerebellar hypoplasia), in: ISMRM 2014, 22nd of the International Society for Magnetic Resonance in Medicine. Proceedings of the International Society for Magnetic Resonance in Medicine, Annual Meeting Proceedings, Milano, Italy, 2014, p. 3435
- S. Tourbier, X. Bresson, P. Hagmann, M. Cagneaux, M. Schaer, L. Guibaud, J.-P. Thiran, R. Meuli, M. B. Cuadra, Automated brain extraction in fetal MRI by multi-atlas fusion strategy: Study on healthy and pathological subjects, in: ISMRM 2014, 22nd of the International Society for Magnetic Resonance in Medicine. Proceedings of the International Society for Magnetic Resonance in Medicine, 2014, p. 4305

Professional Experience

- **Bracco Suisse S.A. – Research Center** Geneva, CH
R&D Engineer *Oct. 2011 – May 2012*
 - Responsible for porting Matlab image processing algorithms to C# / C++, the development environment of *VueBoxTM*, a quantification software tool.
 - Responsible for algorithm optimization. Experienced with memory / performance profiling, optimized numerical library (Intel MKL), image processing library (ITK), CPU parallelization and GPU programming (CUDA).
 - Developed a website in support to commercialization of *VueBoxTM* (CSS, HTML5, PHP, Javascript, SQL).

M.Sc. Thesis (Grade: 6/6) *Feb. 2011 – Sept. 2011*

 - Responsible for designing, prototyping and validating image processing systems (optimized subsampling, automatic segmentation, post-processing) for carotid plaque tracking in dynamic contrast-enhanced ultrasound modality.
 - Developed a new ultrasound tissue simulator based on physical principles for validation purpose.
- **Nestlé Research Center (Digestive Health Group) & EPFL (LTS5)** Lausanne, CH
Research Intern *June 2010 – Aug. 2010*
 - Integrated Matlab-based methods in a standalone application with GUI, wrote HTML documentation and User's guide.
 - Responsible for image acquisition guidelines.
 - Participated in a seminar to present the application developed to other research groups.

M.Sc. Semester Project (Grade: 6/6) *Feb. 2010 – June. 2010*

 - Designed, implemented and validated new image processing algorithms for quantitating neurons in confocal microscopy.
- **World Medical Device Organization** Ecublens, CH
Part-time IT Support *March 2009 – Jan. 2011*
 - Technical support to the production unit: Audio and video recording/processing for e-learning modules.
 - Prototyped a new website platform: Database modeling, Graphical and Technical specifications (Website pre-design, Use cases).

Skills

Computing Languages: C/C++, C#, CUDA, Matlab, Java, Python, VBS, R, \LaTeX , CSS, HTML / HTML5, PHP, SQL.

Image Processing: DICOM, ITK/VTK/Qt, OpenCV, Custom ImageJ Plugins, Matlab Image Processing Toolbox.

Languages: Native French, Pre-advanced English (Level C1).

Interests

Sports (Snowboard, Tennis, Mountain hiking), Music (Saxophone), Independent backpacking (Australia, Canada, Ecuador, Guatemala, India, Malaysia, Mexico, USA, Thailand)